GDAŃSK UNIVERSITY
OF TECHNOLOGY

FACULTY OF ELECTRONICS, TELECOMMUNICATIONS
AND INFORMATICS

The author of the PhD dissertation: Sylwia Babicz-Kiewlicz
Scientific discipline: electronic

DOCTORAL DISSERTATION

Title of PhD dissertation: Analysis of Atomic Force Microscopy surface images by means of higher-harmonic tip vibrations modes

Title of PhD dissertation (in Polish): Analiza obrazowania powierzchni mikroskopem sił atomowych na podstawie pomiarów wyższych harmonicznych drgań igły mikroskopu

Supervisor *signature*
dr hab. inż. Janusz Smulko, prof. nadzw. PG

Gdańsk, year 2015

Table of contents

List of abbreviations

A – amplitude of vibrations [V]

A_{r_i} – spectrum of the i-th row of the image

$|A_c|$ – average module of the column spectrum

$|A_r|$ – average module of the row spectrum

AFM – Atomic Force Microscope

a – length of the cantilever [nm]

a_0 – intermolecular distance introduced to avoid numerical divergence of the force F_{ts} [nm]

b – width of the cantilever [nm]

c – height of a small object [nm]

c_z – spring constant [N/m]

d – distance between atoms (the edge of the tip and the surface) [nm]

E – Young’s modulus [GPa]

E^* – effective contact stiffness [GPa]

E_e – modulus of elasticity [GPa]

E_t, E_s – respective elastic moduli [GPa]

$\langle E_k \rangle$ – average kinetic energy [J]

$\langle E_p \rangle$ – average potential energy [J]

$F(d)$ – Lennard–Jones force [nN]

$F(x, t)$ – resultant force acting on the tip in time t [nN]

F_0 – amplitude of the driving force [nN]

F_{ts} – tip-surface interaction force [nN]

F_{ts_n} – coefficients representing the n^{th} harmonic component of the oscillating tip [nN]

$F_{ts_{\cos}}$, $F_{ts_{\sin}}$ – cosine and sine Fourier coefficients [nN]

f – frequency [kHz]

f_0 – angular resonance frequency of the free cantilever [kHz]

F_{ts} – tip-surface interaction forces [nN]

H – Hamaker constant [zJ]

$H(X)$ – Shannon entropy of a random variable X

I – moment of inertia [kg m^2]

i – row number in the image

j – column number of the image

k_B – Boltzmann constant [$1.38064852(79)\cdot10^{-23}$ J/K]

M – number of rows of the image

m_{eff} – effective mass of the cantilever [kg]

N – number of columns of the image

n – higher-harmonic image order

Q – quality factor

$q_n(i, j)$ – height of the point (i, j) of the n^{th} higher harmonic image

q_{p_k} – one of the five highest ($k = 1,\ldots, 5$) points within the analysed image

q_{v_m} – one of the five lowest ($m = 1,\ldots, 5$) points within the analysed image

R – tip radius [nm]

r – number of degrees of freedom

S_{10z} – Ten Point Height [nm]

S_a – roughness [nm]

S_{ku} – kurtosis

S_{sk} – skewness

S_q – root mean square (quadratic mean) of topography of all the points [nm]

S_y – peak-to-peak value (difference between the maximum $q_{\max}$ and the minimum $q_{\min}$ values) [nm]

T – temperature [K]

$U(d)$ – Lennard–Jones potential energy [aJ]

$w(x, t)$ – transverse displacement of the cantilever in time t and across the axis OX [nm]

$\left\langle v^2 \right\rangle$ – mean square deflection of the cantilever caused by thermal vibrations [nm]

v_t, v_s – Poisson’s rations of tip and sample

X – random variable

x – x-axis distance [nm]

y – y-axis distance [nm]

z – tip deflection in z-axis [nm]

z_c – distance between sample and free tip [nm]

ε – depth of the potential well [aJ]

φ_n – phase shift of the n^{th} harmonic component [rad]

μ – material density [kg/m^3]

$\mu_{\Delta \mathrm{n}}$ mean intensity of the pixel for the n^{th} higher-harmonic image

σ – distance when the potential between the molecules equals to zero [nm]

1 Introduction

The fast development of physics and electronics forced creation of new microscopic devices which enabled examining very small objects. Such examinations are important for improvements of technology and quality of various materials. Since the 20th century, when the science brought many discoveries in the field of nanotechnology (like metallic clusters, nanotubes, thin films or nanowires), research on surface morphology and its imaging with very high resolution has become one of the most important subjects.

The breakthrough has occurred in 1980's when a series of scanning probe microscopes (SPM) were invented. The SPM defines a broad group of high sensitivity instruments used to determine chemical and biological properties of various materials. One of these microscopes, a scanning tunnelling microscope (STM), was developed by Gerd Binnig and Heinrich Rohrer at IBM Zürich in 1982 [1-3]. The inventors earned the Nobel Prize in Physics in 1986 for that achievement. The STM examines morphology of a specimen basing on the concept of quantum tunnelling. The tunnelling current is found to be proportional to the local density of surface's states, at the position of the tip. Unfortunately, this method is not capable for analysing insulators and biological materials, like viruses, bacteria or DNA when their natural environment conditions have to be preserved during examination. This fact, associated with development of surface science, materials engineering, biochemistry and biotechnology, prompted one of the constructors of STM, Gerd Binnig, to build another tool for microscopy research.

The atomic force microscope was invented in 1986 [4, 5] as an alternative to the scanning tunnelling microscope, which cannot be used in studies of non-conductive materials. The AFM, however, has the advantage of imaging almost any type of surface, including polymers, ceramics, composites, glass, and live biological samples in conditions resembling their natural environment. Thanks to this property, the AFM can be effectively used to study biological samples [6]. Its additional advantage, in comparison with the STM microscope, is its non-destructive operation. Moreover, testing with the STM can cause damage because of electric charges passing through a sample during tests.

Today the AFM is a powerful, versatile and fundamental tool for visualization and studying the morphology of material surfaces. The AFM is widely used in research of materials as well as mechanical properties of nanostructures [7-10]. Moreover, the AFM can also be used to measure force-versus-distance curves [11]. Such curves, briefly called force curves, provide valuable information on local material properties like adhesion, hardness or elasticity. Moreover, additional information for some materials can be recovered by analysing higher cantilever modes when the cantilever motion is inharmonic and generates frequency components above the excitation frequency, usually close to the resonance frequency of the lowest oscillation mode [12, 13]. That method has been applied and developed in the thesis because it can be relatively easily adopted in various AFM units by using the prepared measurement setup. There are also other methods utilizing numerous harmonic signals (e.g. the multimodal atomic force microscopy [13]), but these methods have not been considered now.

The main aim of the work was to develop measurement systems for simultaneous analysis of multiple harmonics of AFM cantilever oscillations for surface imaging and improvement of its quality at selected experimental conditions (e.g. during growth of corrosion products). That required preparation of a virtual instrument, performing sampling the signals from the AFM at a sufficiently high frequency and implementation of synchronous detection algorithms (lock-in amplifiers) to determine intensity of higher harmonics of the vibrating microscope cantilever and enable reduction of background noise at various experimental conditions.

In the thesis two following assertions are proved:

1. *higher-harmonic imaging can be used efficiently during corrosion process monitoring to reveal differences in various corrosion products,*
2. *exposure of the selected details may be improved by using the higher-harmonic images and the proposed procedure based on the parameters: signal-to-noise ratio and entropy.*

This work, at its introduction, highlights versatility of the atomic force microscopy and presents its operation principles (Chapter 2). The mathematical analysis of tip-sample interaction and cantilever motion explains the origin of higher-harmonic generation in the recorded response signal of cantilever oscillations. The higher harmonics are generated due to the non-linear tip-sample interaction which depends on physical properties of the examined specimen [14, 15]. Thus, the higher-harmonic imaging may be used to visualize additional surface details in a better way than by the dedicated atomic force microscope software examining only topography of the specimen.

The developed measurement system for recording higher harmonics of the vibrating cantilever is presented in detail (Chapter 3). The system contains a virtual instrument, recording data at a sufficiently high sampling frequency and controlling one of two different data acquisition boards (USB-6356, PXI-5122). The system enhances measurement capabilities of various AFMs as detachable units. Moreover, the dedicated software has been developed to analyse the recorded data. The software implements a lock-in amplifier and can generate higher-harmonic images up to the frequency $f = 625$ kHz (USB-6356), or even $f = 50$ MHz (PXI-5122). Moreover, additional software for the analysis and improvement of quality of the higher-harmonic images has been created. The software task is to analyse the generated higher-harmonic images by automating the process of their selection according to the presented details.

The thesis presents numerous experimental results (Chapter 4) which include topography analysis and higher-harmonic imaging at various stages and environments (air or liquid). In addition, usability of the higher-harmonic imaging for surfaces having different material properties is described. The data for several selected materials have been compared. The identified details are visualized with the higher-harmonic imaging to expose their heterogeneous morphology.

Furthermore, the problem of image quality and its information contents has been considered. Statistical measures, like signal-to-noise ratio and entropy, have been applied to figure out the content of the analysed images (Chapter 5). These efforts have resulted in the proposal of an algorithm automatically exposing selected details from various higher-harmonic images.

2 The principle of operation of an atomic force microscope and higher-harmonic imaging

2.1 Background information

The principle of an atomic force microscope (AFM) operation is shown in Fig. 2.1. A sharp tip [16] is attached to the free end of flexible cantilever placed in a close proximity of the tested sample. At another end of the cantilever, a piezo is attached to induce cantilever – and hence the tip – vibrations of amplitude A at the selected frequency. Typically, the resonant frequency f_0 of this mechanical object is selected. During scanning, the sharp silicon (or silicon nitride) tip moves over the sample surface. As a result of the existing tip-surface forces, the cantilever bends. The optical method is the most common approach to detect deflections from the tip mean position [17]. The optical measurement unit uses a laser beam focused on the back side of the cantilever [18]. The beam position is measured after reflection by a matrix of photodiodes. A feedback loop is employed within the AFM control unit to stabilize the acting force on the AFM tip.

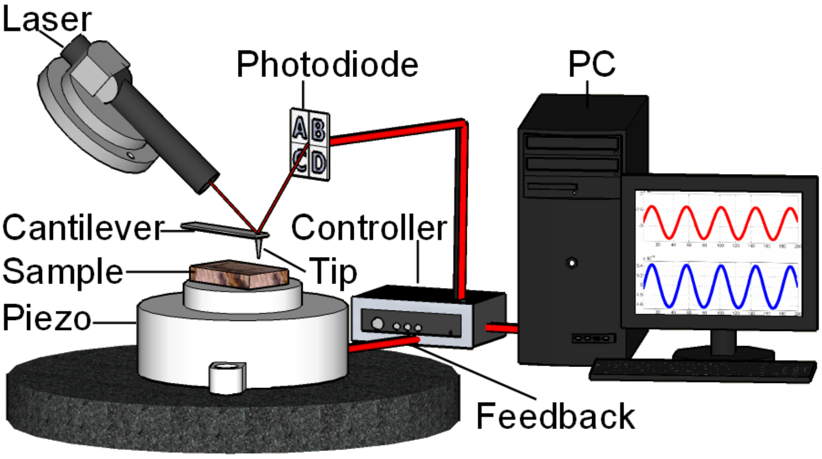

Fig. 2.1 A schematic setup of AFM

Information about the feedback loop and intensity of the reflected laser beam is transmitted to a computer. There, a dedicated software generates a map of topography and/or other properties of interest. The AFM enables also examination of twisting the lever caused by forces parallel to the plane of the tested specimen. Therefore, in addition to topographic measurements, the microscope can also provide information about the mechanical properties of the sample, such as flexibility, adhesion force or friction.

The observed oscillations of the cantilever in the AFM depend on a chosen measurement technique. These oscillations are determined by the force existing between the tip and the specimen. The force depends on the distance between these objects and the physical properties of applied materials. The tip-sample interaction is described by the Lennard-Jones potential energy function [19-26]:

$$U(d) = 4\varepsilon\left(\frac{\sigma^{12}}{d^{12}} - \frac{\sigma^{6}}{d^{6}}\right) = \frac{HR}{6\sigma}\left(\frac{1}{210}\frac{\sigma^{7}}{d^{7}} - \frac{\sigma}{d}\right), \tag{2.1}$$

where:
$U(d)$ – the Lennard-Jones potential [aJ],
d – the distance between atoms at the edge of the tip and the sample surface [nm],
H – the Hamaker constant [zJ],
R – the tip radius [nm],
ε – the depth of the potential well [aJ],
σ – the distance when the potential between molecules equals to zero [nm].

The force induced by the Lennard-Jones potential $U(d)$ between the tip and the a sample is its derivative [22, 27]:

$$F(d) = -\frac{\partial U(d)}{\partial d} = \frac{HR}{6\sigma^{2}}\left(\frac{\sigma^{2}}{d^{2}} - \frac{1}{30}\frac{\sigma^{8}}{d^{8}}\right) \tag{2.2}$$

The potential function is shown in Fig. 2.2. The Lennard-Jones potential (solid line) depends on the distance between tip and sample and is the total potential of two opposite interactions: the repulsive (dotted line) and attractive (dashed line) ones. Thus, three different modes of the AFM are marked as: the contact mode, the tapping mode and the non-contact mode [28].

The main difference between these modes is, as their names suggest, the interactive force between the sample and the tip [20]. Depending on the material type, this function has different characteristic points (zero crossing at σ, and a minimum at ε), but its overall shape remains unchanged.

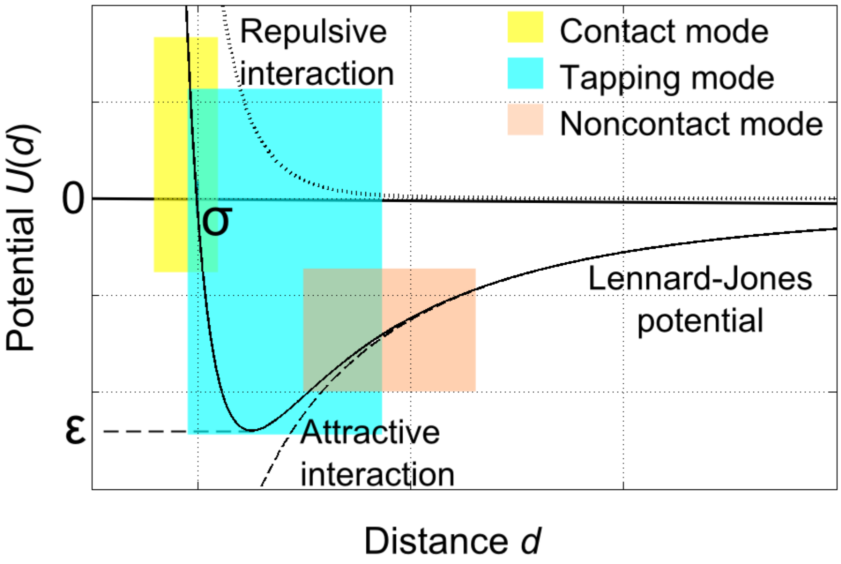

Fig. 2.2 The Lennard-Jones potential function $U(d)$ with the marked AFM modes, determined by the distance d

In the contact mode, the cantilever is held less than a few angstroms (10^{-10} m) from the sample surface, and the interatomic force between the cantilever and the sample is repulsive with the mean value of 10^{-9} N [6]. The AFM probe scans the specimen by keeping a constant force between the probe and the sample surface to obtain a three-dimensional (3D) topographical map [19]. When the probe cantilever is deflected by topographical changes, the scanner adjusts the probe position to restore the original cantilever deflection. Information about the scanner position is used to create a topographical image. The contact mode is used to examine hard materials. High-resolution images can be created during such measurements. Unfortunately, due to the physical contact between the needle and the sample, the needle may be damaged quite easily [20].

In the tapping mode, the probe cantilever oscillates in a proximity of its resonant frequency. The amplitude of such oscillations is greater than in the case of the above mentioned contact mode (~10 nm), reaching typically 100÷200 nm. The oscillating tip scans at a height where it barely touches, or "taps", the sample surface. The system monitors the probe position and vibrational amplitude to obtain a topography image and information on other properties (adhesion, electrical conductivity, thermal conductivity) [29-33]. When the needle touches the sample, the cantilever oscillates with the highest amplitude [34]. The advantage of tapping the surface is a high lateral resolution also in soft samples [35, 36]. The lateral forces, common in the contact mode, are virtually eliminated.

In the non-contact region, the cantilever is held at the distance of 1÷10 nm from the sample surface, and the interatomic force between the cantilever and the sample is attractive. The cantilever oscillates at frequencies slightly above its resonant frequency where the amplitude of oscillations is typically a few nanometres (< 10 nm) only [37-39]. The non-contact mode is mostly used to investigate soft and delicate samples where disturbing or destroying the sample is to be prevented. This is particularly important in biological applications and organic thin films.

2.2 The mathematical model of AFM scanning tip oscillations

The AFM image is generated by recording signals related to the force between the vibrating cantilever and atoms of the examined sample during movements in the x and y directions. Because of some symmetry considerations, the micro-cantilever may be approximated to a one-dimensional object. The Euler-Bernoulli equation describes motion of the cantilever tip (transverse displacement) [12, 40-44]:

$$F(x,t) = E \cdot I \cdot \frac{\partial^4 w(x,t)}{\partial x^4} + \mu \frac{\partial^2 w(x,t)}{\partial t^2}\,, \tag{2.3}$$

where:
$w(x, t)$ – the transverse displacement of the cantilever in time t and across the axis OX [nm],
$F(x, t)$ – the resultant force acting on the tip in time t [nN],
E – the Young’s modulus [GPa],
I – the moment of inertia [$kg \cdot m^2$],
μ – the density of the specimen’s material [kg/m^3],
t – time [ms].

The material’s density, the Young’s modulus and the moment of inertia are assumed to be constant, so that the tip can be treated as a massless object. The equation (2.3) is very difficult to be solved. Therefore, some authors [45-50] have considered the cantilever tip as a point-mass spring. In such a case, the tip motion can be described by the non-linear equation of the second order [34, 46, 51-56]:

$$F_{ts}(z) + F_0 \cos(2\pi f t) = m_{eff} \frac{\partial^2 z}{\partial t^2} + \frac{m_{eff} 2\pi f_0}{Q} \frac{\partial z}{\partial t} + c_z z\,, \tag{2.4}$$

where:
z – the tip position in time t (Fig. 2.3) [nm],
F_{ts} – the tip-surface interaction force [nN],
F_0 – the amplitude of the driving force (the external force induced by the applied voltage) [nN],
f – the frequency of the driving force [kHz],
Q – the quality factor,
c_z – the spring constant of the free cantilever [N/m],
m_{eff} – the effective mass of the cantilever [kg],
f_0 – the resonance frequency of the freely vibrating cantilever [kHz],
t – time [ms].

The frequency f_0 is determined by physical properties of the cantilever (the effective mass and the spring constant) [57]:

$$f_0 = \frac{\sqrt{\frac{c_z}{m_{eff}}}}{2\pi} \tag{2.5}$$

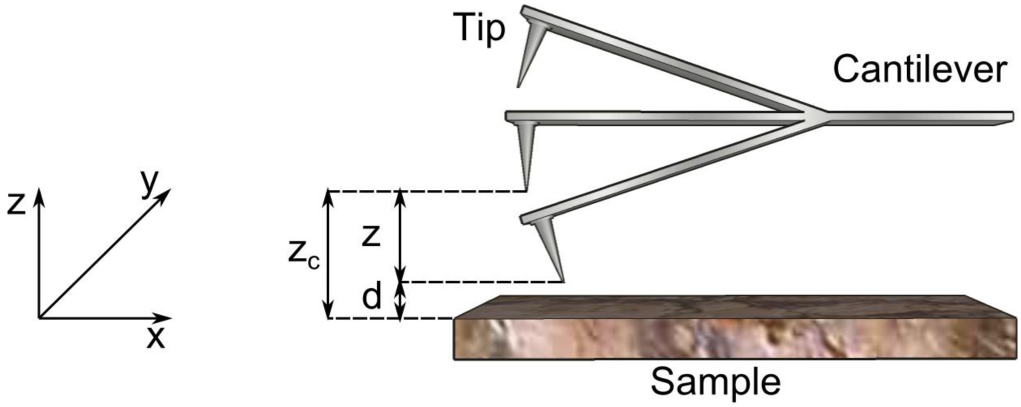

Fig. 2.3 A scheme of the relevant spatial distance in the non-contact mode of AFM between the examined sample and the tip

It is very difficult to find the solution of the tip motion equation using (2.4). This is because we have assumed the mathematical model of the point-mass and spring. Moreover, in reality more frequency modes will exist except of the mentioned eigenmode at the frequency f_0. Thus, there are some serious simplifications of the presented mathematical model. The simplest tip-sample interaction model is based on the Herzian model [58, 59], which assumes a hemispherical tip shape and ignores adhesive forces [60] (when the surface energy and applied static loads are very small). More detailed models are the Johnson-Kendall-Roberts (JKR) and Derjaguin-Muller-Toporov (DMT) ones [61], where the adhesion forces cannot be neglected [62-64]. Systems without energy dissipation in the tip-sample contact can be modelled using the DMT model leading to [12, 13, 34, 41-43, 46, 54, 65, 66]:

$$F_{ts}(z,z_c)=\begin{cases} -\dfrac{HR}{6(z_c-z)^2} & d\geq a_0 \\ -\dfrac{HR}{6a_0{}^2}+\dfrac{4}{3}E^*\sqrt{R}\left(a_0-z_c+z\right)^{3/2} & d<a_0 \end{cases}, \tag{2.6}$$

where:
a_0 – the intermolecular distance introduced to avoid numerical divergence of the force F_{ts} [nm],
E^* – the effective contact stiffness [GPa].

The value of E^* is given by the equation [46, 58]:

$$E^*=\left(\frac{1-v_t{}^2}{E_t}+\frac{1-v_s{}^2}{E_s}\right)^{-1}, \tag{2.7}$$

where:
E_t and E_s – the respective elastic moduli [GPa],
v_t and v_s – the Poisson's ratios of tip and sample.

As shown in Fig. 2.2, van der Waals forces dominate in the attractive regime when $d \geq a_0$ (Fig. 2.3) in a long-range distance. In the repulsive regime ($d < a_0$), the tip-sample forces [65] are calculated from the DMT model. The non-linearity introduced by (2.6) causes generation of higher harmonics in the AFM response signal. For the harmonic tip motion [67]:

$$z_c(t)=A\cos(2\pi ft+\varphi) \tag{2.8}$$

if the boundary conditions are stable, the resulting tip-sample interaction force F_{ts} can be expanded in a Fourier series [67]:

$$F_{ts} = \sum_{n} F_{ts_n} \sin(2\pi nft + \varphi_n) , \tag{2.9}$$

where:

F_{ts_n} – the Fourier coefficients representing the n^{th} harmonic component of the oscillating tip [nN]],

φ_n – the phase shift of the n^{th} harmonic component [rad].

The Fourier coefficients F_{ts_n} depend on the shape of interaction potential in (2.6). That shape depends on the local material properties, what results in various levels of selected harmonics for different materials. This enables distinguishing materials with different physical properties by higher-harmonic imaging.

The presented equations predict occurring non-linear effects in the tip motion [13, 68]. These non-linear components will generate higher order harmonics. Unfortunately, there is no analytical method of solving such non-linear differential equations. We can solve (2.6) only by applying numerical methods to determine intensities of the harmonic components. This requires a knowledge of physical parameters (e.g. the Hamaker constant H, the effective contact stiffness E^*) characterizing the applied tip and the examined surface. Such a detailed knowledge is often unavailable and therefore a method based on the numerical solution cannot be applied in practice too often. Furthermore, some of the harmonics are suppressed or enhanced by the resonances of the vibrating setup of the cantilever and the surface, and are situated above the main resonant frequency f_0 [Fig. 2.4]. Deviations from the purely sinusoidal behaviour of the periodic tip oscillations may be also a result of some dissipative effects. The energy dissipation comes from the tip movement itself, when the tip approaches and recedes from the sample's surface in a single oscillation cycle [69]. The energy dissipation causes hysteresis of the motion resulting in appearing additional Fourier components. Moreover, the cantilever itself has a complicated dynamic behaviour. Its complex structure means additional flexing, twisting and bending during the measurements [70, 71]. These movements generate additional resonances or influence their intensities [72].

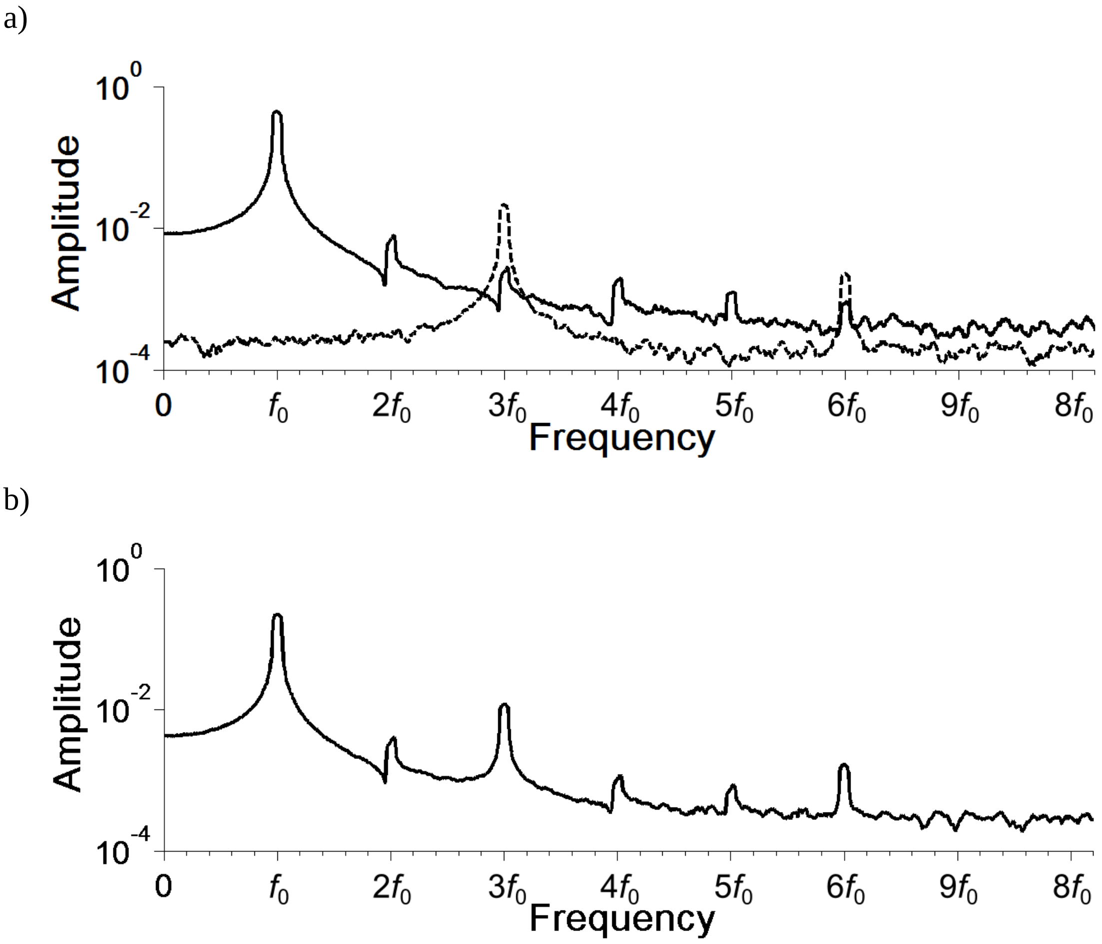

Fig. 2.4 An illustration of the influence of the measurement system frequency characteristic on the harmonic levels at the system output: a) the power spectrum of generated oscillations in the system (solid line) and the frequency characteristic of the measurement system (dashed line), b) the resultant spectrum at the measurement system output with a visible effect of amplification of the 3rd and the 6th harmonics

Because of the difficulty of determining the most informative harmonics, we are forced to perform a series of measurements for subsequent levels of harmonics repeatedly, or detecting all harmonics during a single scan process. The first method requires repeated and very long measurements, when the sample may be displaced accidentally or the microscope may be tuned out. The second method requires a more expensive data acquisition board and real-time processing (e.g. using an FPGA module for data pre-processing in the applied data acquisition board).

2.3 The multimodal atomic force microscopy

The AFM techniques are being continuously developed [73-76]. The recently proposed method is a multimodal technique using a variety of cantilever oscillatory motions related with flexing, twisting and bending of the applied cantilever [77, 78]. Two types of interactions are considered in that method: the non-linear tip-sample interaction and multiple resonances of the cantilever (Fig. 2.5). Thus, the spectrum of the output signal results from both the tip-sample interactions and the mechanical forces (Fig. 2.6).

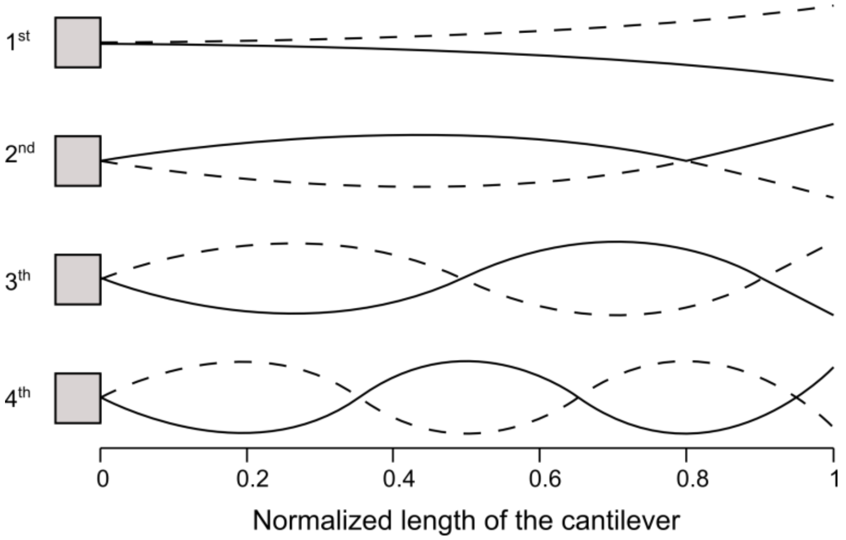

Fig. 2.5 The first four flexural eigenmodes of the free cantilever [13]

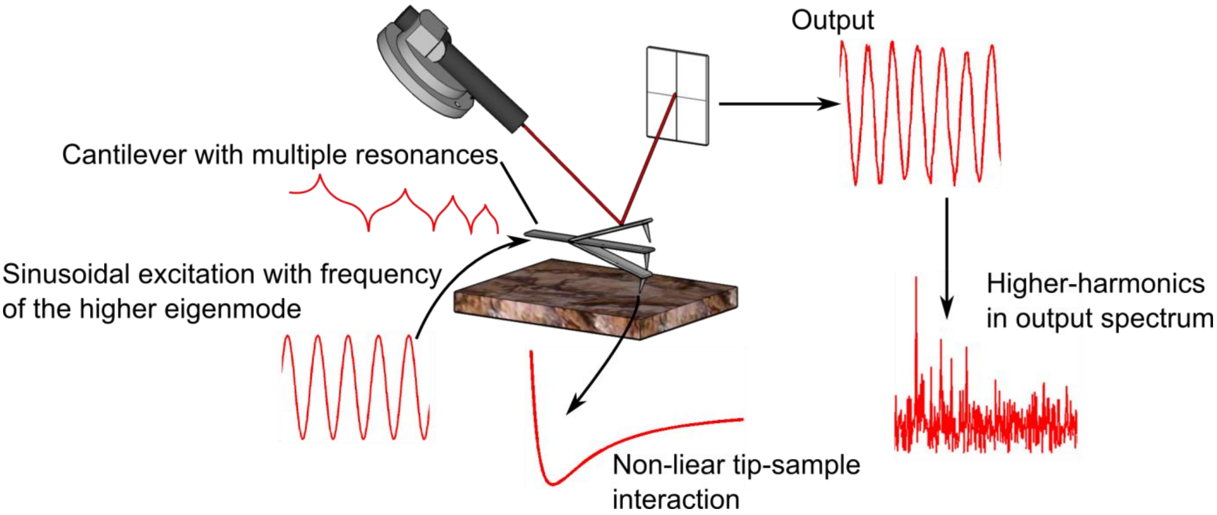

Fig. 2.6 An illustration of signals in the multimodal atomic force microscopy [13]

We can imagine various excitations which would result in generation of various harmonics at the output signal. There were some experiments when the excitation was a harmonic signal at the second cantilever eigenmode [79-81], a tri-modal excitation [82, 83], or even a continuous band excitation [84, 85]. These schemes can be very efficient because excitation with higher frequencies means faster measurements and additional possibilities of characterizing examined specimens. These methods are currently investigated by other research groups.

It has to be underlined that the above mentioned multimodal AFM is completely different from the method based on analysis of higher harmonics and considered in the thesis. The higher-harmonic methods use excitation with a harmonic signal at frequencies close to the eigen-frequency of the system and gather additional information by analysing intensities of the observed higher harmonic due to non-linear effects. Those methods can be used in numerous AFM setups during surface scanning. The multimodal AFM requires different excitation and has to be performed during a separate scanning process.

2.4 Noise sources in the atomic force microscopy

The cantilever in the AFM acts as a micro-electromechanical (MEMS) sensor. Such sensors are applied to detect acceleration, angle, pressure or presence of chemical and biological molecules. Because of a very small size of the MEMS structure, its inherent noise limits the measurement accuracy [86, 87]. The thermal noise of the cantilever is a fundamental noise source in the atomic force microscopy and determines its inherent noise intensity [86].

An average kinetic energy $\langle E_k \rangle$ of any object in thermal equilibrium is given by:

$$\langle E_k \rangle = \frac{r}{2} k_B T \,, \tag{2.10}$$

where:
r – the number of degrees of freedom,
k_B – the Boltzmann constant [J/K],
T – the temperature [K].

If the cantilever is considered to be a small object of the height c (Fig. 2.7), its potential energy is equal to:

$$\left\langle E_p \right\rangle = \frac{c^2}{2} c_z \tag{2.11}$$

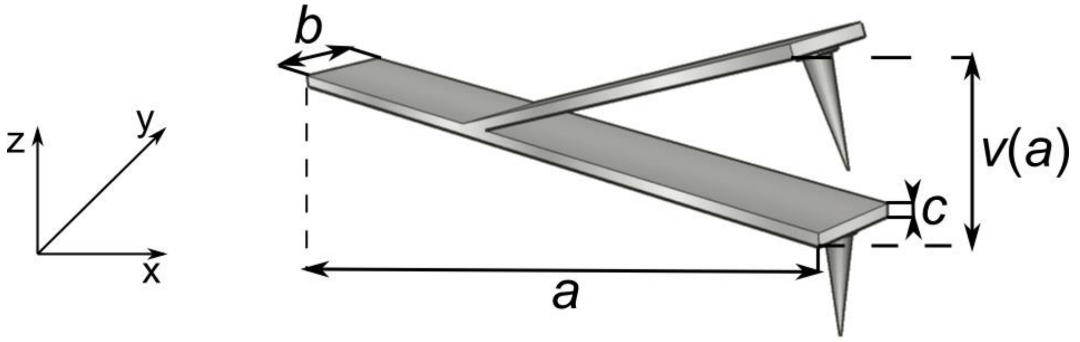

Fig. 2.7 A schematic of the cantilever

If we consider the cantilever as a bar of length *a*, width *b* and height *c*, its spring constant is given by:

$$c_z = 0.25 E_e \frac{bc^3}{a^3}, \tag{2.12}$$

where:
a – the cantilever length [nm],
b – the cantilever width [nm],
E_e – the modulus of elasticity [GPa].

Comparing the thermal energy given by (2.10) and the potential energy proportional to the spring constant given by (2.12) we can determine the mean square deflection $\left\langle v^2 \right\rangle$ of the cantilever caused by thermal vibrations [88]:

$$\frac{1}{2} k_B T = \frac{1}{2} c_z \left\langle v^2 \right\rangle \Rightarrow \sqrt{\left\langle v^2 \right\rangle} = \sqrt{\frac{k_B T}{c_z}} \tag{2.13}$$

Except of the thermal noise we can observe at a very low frequency range a flicker noise (1/*f* noise) component with its power spectral density depending on frequency as 1/*f* [89, 90]. Moreover, thermal instability (e.g. temperature drift) can strongly decrease accuracy of the performed measurements. The 1/*f* noise component can be reduced by applying materials which are characterized by a very low intensity of that component (e.g. Invar [37]). Temperature drifts can be minimized by applying a control unit for temperature stabilization, and having sufficiently long time constants. When the mentioned methods are applied the main source of inaccuracy in the AFM measurements is due to the thermal noise. That noise can be reduced by lowering the temperature of the vibrating cantilever. It means that we have to lower the temperature of the examined specimen as well. Unfortunately, a lower temperature of the examined specimen means changing its physical properties and cannot be used in all experimental studies. Thus, the best solution to assure a high signal-to-noise ratio during the AFM measurements is to have sufficiently strong oscillations of the vibrating tip.

It should be underlined that - except of the thermal noise - any other mechanical interference would decrease the measurement accuracy. Thus, additional precautions, like a mechanical suspension system attenuating external vibrations, would be appreciated.

3 Measurement systems of higher-harmonic images

Higher-harmonic images can be generated when the necessary signals are recorded during the AFM scanning process. It requires application of an additional data acquisition board to record output signals of the AFM in three independent channels at a sufficiently high sampling frequency. The recorded data have to be processed to determine intensity of the harmonics of interest by applying synchronous detection for each pixel separately [91]. That operation can be done in real time or after scanning. It depends on the applied data acquisition board, computing and data saving speed capabilities of the control computer.

It should be underlined that the data recorded during scanning of a single picture with the resolution of 256 x 256 pixels require about a few GB disk space. Such amount of data needs time for saving and data processing. Therefore, the measurement setup has to be designed to meet such requirements. There are two main sources of limitations in such measurement setups. One is the control computer which has to be relatively fast and does not require significant financial funds. The more expensive element is a precise and fast data acquisition board. Available sampling frequencies will limit the maximal frequency of higher harmonics used for image generation. There are various data acquisition boards available on the market and characterized by the maximum sampling frequency, resolution of the applied analogue-digital converter and possibility of relatively fast data saving and pre-processing using FPGA modules. Two selected data acquisition boards of relatively different parameters and costs were selected to be used in the measurement setups, denoted as version 1 and version 2. Both versions are presented below in this chapter.

3.1 The measurement system – version 1

3.1.1 The data acquisition unit

The details of the designed and constructed measurement system for higher-harmonic detection are shown in Fig. 2.1, Fig. 3.1 and Fig. 3.2 [92-94]. An NTEGRA

Prima system produced by NT-MDT was used as the AFM. The system creates images of specimen surfaces proportionally to intensity of the higher harmonic present in the recorded response signal.

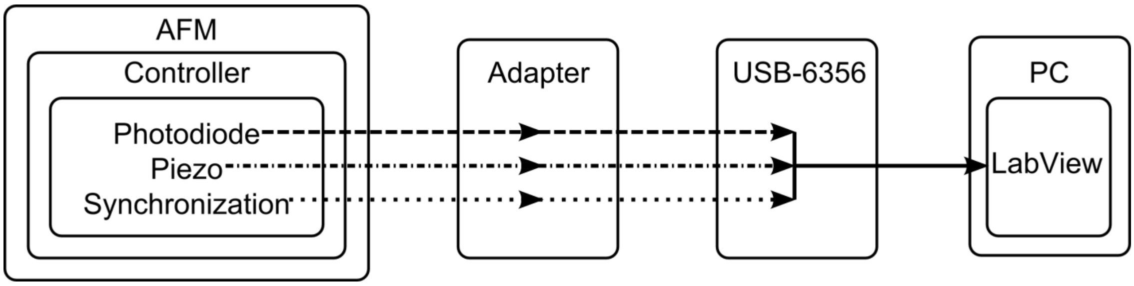

Fig. 3.1 A block diagram of the created measurement system

Fig. 3.2 A photo of the measurement system

Three signals are needed to do it: a harmonic signal generated to excite the cantilever, the output signal of the cantilever vibrations measured by a photodiode and a synchronization signal that identifies pixels during scanning. The extension output of the microscope assures access to the photodiode signal and the excitation signal of the tip. The synchronization signal is also taken from the control unit of the AFM. The three signals are recorded by a National Instruments USB-6356 data acquisition board and stored by a program prepared in LabView software. The setup can record all necessary data during surface scanning by the AFM.

Two types of AFM tips have been tested: NSG01 and HA_NC version A, produced by NT-MDT (Fig. 3.3). Both types have gilt surfaces to reflect a laser beam and can be used in the tapping-mode when the tip is placed in air or liquid. Selected parameters of the tips are presented in Tab. 3.1. These tips have been selected because they were used in various laboratory experiments and reasonable results in the tapping-mode should be expected.

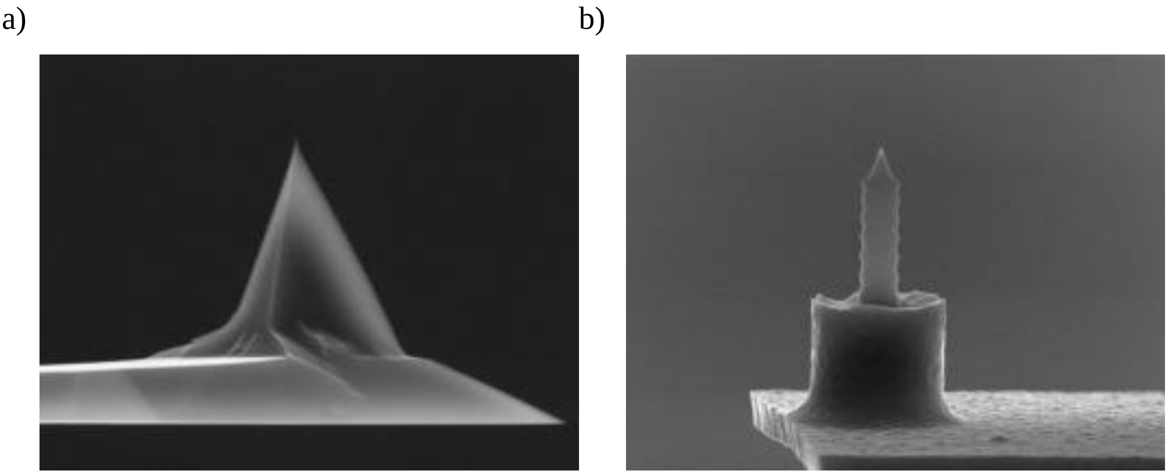

Fig. 3.3 Photos of the tested AFM tips: a) NSG01, b) HA_NC

The best results of preliminary measurements (for ZnO and sapphire layers) have been obtained for the NSG01 tip, since its resonance frequency and force constant have lower values (Tab. 3.1). The NSG01 tip is suitable for measurements in air or liquid, so it may be used in electrochemical (EC-AFM) measurements (e.g. for corrosion monitoring).

In the first measurement trial a fresh tip, NSG01 type, was applied to perform experiment. The sampling frequency was set to 1.25 MSa/s (the highest sample rate allowed by the USB-6356 board). The measurements were made by applying the non-contact mode, when the tip had no contact with the examined surface and non-linear effects were less visible when compared with conditions existing in the tapping mode. Firstly, the cantilever freely vibrating in air displayed only the second harmonic component, which was three orders lower than the tip eigenfrequency f_0 (Fig. 3.4a). The second harmonic component intensity (Fig. 3.4b) was a few times greater than that observed in the freely vibrating cantilever (Fig. 3.4a).

Tab. 3.1 General information and parameters of the applied AFM tips

Material type	single crystal silicon, N-type			polysilicon lever, monocrystal silicon tip
Chip size [mm]	3.4 x 1.6 x 0.3			3.6 x 1.6 x 0.4
Cantilever number	1 rectangular			2 rectangular – A and B
Cantilever length [µm]	125 ± 5			94
Cantilever width [µm]	30 ± 3			34
Cantilever thickness [µm]	2 ± 0.5			1.85
Resonant frequency [kHz]	min.	typical	max.	235
	87	150	230	
Force constant [N/m]	min.	typical	max.	12
	1.45	5.1	15.1	

The same signals for the same cantilever were observed when the sapphire structure was moved closer to satisfy conditions for non-contact mode measurements. In this case, the cantilever demonstrated more vivid non-linear effects which resulted in the more intense second harmonic component and appearance of the third harmonic (Fig. 3.4b). This proves that a motion of the tip in air, without any interaction with the specimen, is almost linear and the occurrence of higher harmonics results from the tip-sample interactions. The similar results in the tapping mode were observed for other specimens, like ZnO structures and biological specimens [95].

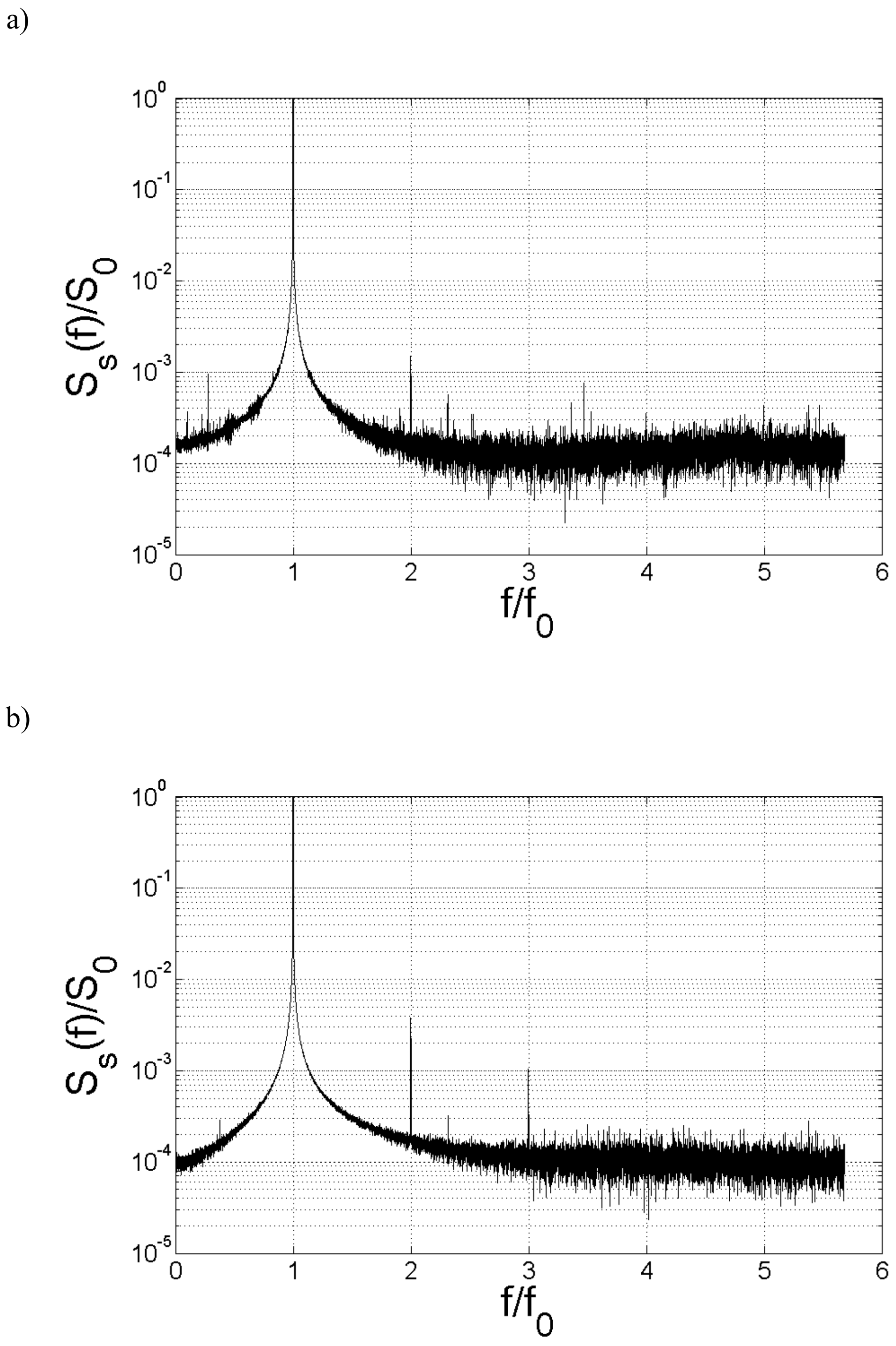

Fig. 3.4 The normalized power spectrum $S_s(f)$ of the cantilever vibrations: (a) in air, (b) in the non-contact mode at vicinity of exemplary sapphire structure; S_0 – the reference value

Other systems working simultaneously with the dedicated AFM software [94, 96-98] and using FPGA programmable acquisition boards are much more expensive and more difficult to implement than the present one because of more advanced and time-consuming programming. It is really difficult to create a real-time system estimating higher harmonics and displaying final results, because the system has to be capable of performing intense computations. The presented solution applies a post-processing lock-in amplifier to reduce the cost of the measurement system [99-101].

3.1.2 The control software and data processing

The data recorded by USB-6356 and LabView software are stored in the Technical Data Management Streaming (TDMS) file format. The binary TDMS file format is an easily exchangeable, inherently structured, high-speed-streaming-capable file format that becomes quickly searchable with no need for complicated and expensive database design, architecture, or maintenance. Unfortunately, the format is incompatible with Matlab software. Thus, the files have to be converted into the MAT type files. During a typical measurement with the scanning frequency of 1 Hz, an image requires about 34 files, each of 60.3 MB disk space, to be saved. The converted files require the total of 4 GB.

After conversion, the user has a graphical interface (Fig. 3.5) [102] to perform subsequent and necessary processing steps to obtain the higher-harmonic images. The software creates a folder hierarchy to simplify the way of selecting files for data processing and software maintenance.

A diagram of the created program is presented in Fig. 3.6. At the beginning, the user defines the processing folder (*Step A*). If any of the folders *MATdata*, *rows*, *lack_of_starts*, *starts* and *images* does not exist, it is created (*Step B*). In *Step C* the first file from the *MATdata* folder is loaded and the *synchronization* signal from the data is plotted. Typically, the scanning frequency and the *synchronization* state should be noted during the measurement, but if they are not, it is possible to read them from the plotted *synchronization* signal. Moreover, the *synchronization* signal can have a non-zero offset. All these data are necessary to properly perform *Step E* and are saved in a file in the *lack_of_starts* folder.

Splitting and merging data files into the row files are two additional operations (*Steps E* and *F*), which are useful in data debugging and controlling for the next steps. In *Step G* all moments of the *synchronization* state change are detected and saved in the *starts* folder for each row. If any processing error occurs and no starts are detected, the information is saved in a file in the *lack_of_starts* folder.

Step H is the main part of the processing program – for each pixel a lock-in amplifier procedure is performed. The procedure requires the reference signal having frequency equal to the frequency of the analysed *n*-th harmonic. These reference signals are obtained by selecting the *n*-th sample of the recorded signal from the AFM generator. The detailed procedure of the lock-in amplifier is presented in Fig. 3.7 and Fig. 3.8. The algorithm described in the literature [99, 100] is used. In our case the lock-in amplifier provides the reference generator (piezo) signal and the cantilever (photodiode) output signal. The signal from the photodiode is sampled and then multiplied by the reference signal [100]. The operation enables estimation of the higher-harmonic intensities from the recorded AFM output signal and reduction of the additive noise component.

As a result of the lock-in amplifier function, the files with selected harmonic intensities for each pixel are saved in the folder. Each file includes values for one row of the resulting image. The files are merged and plotted in *Step K*. It is possible to stop the processing at each stage, because all of them are independent. All images can be saved in the *images* folder or tailored to user requirements – after resizing and filtering.

It is possible to analyse the obtained images by an additional graphic user interface (Fig. 3.9). The program draws the selected column (left red plot) and row (below blue plot) of each of the higher-harmonic images. This enables detecting the higher-harmonic image that exhibits the highest sensitivity to identify a specific surface heterogeneity. The row and column can be chosen either by sliders or by two input boxes – the blue one for a row and the red one for a column. The created software enables selecting, filtering, and saving the set of higher-harmonic images.

The third graphic user interface (Fig. 3.10) was created to filter periodic disturbances in higher-harmonic images. The graphic user interface presents the original selected higher-harmonic image with the marked row and column for further analysis to determine parameters of possible additional filtering [103].

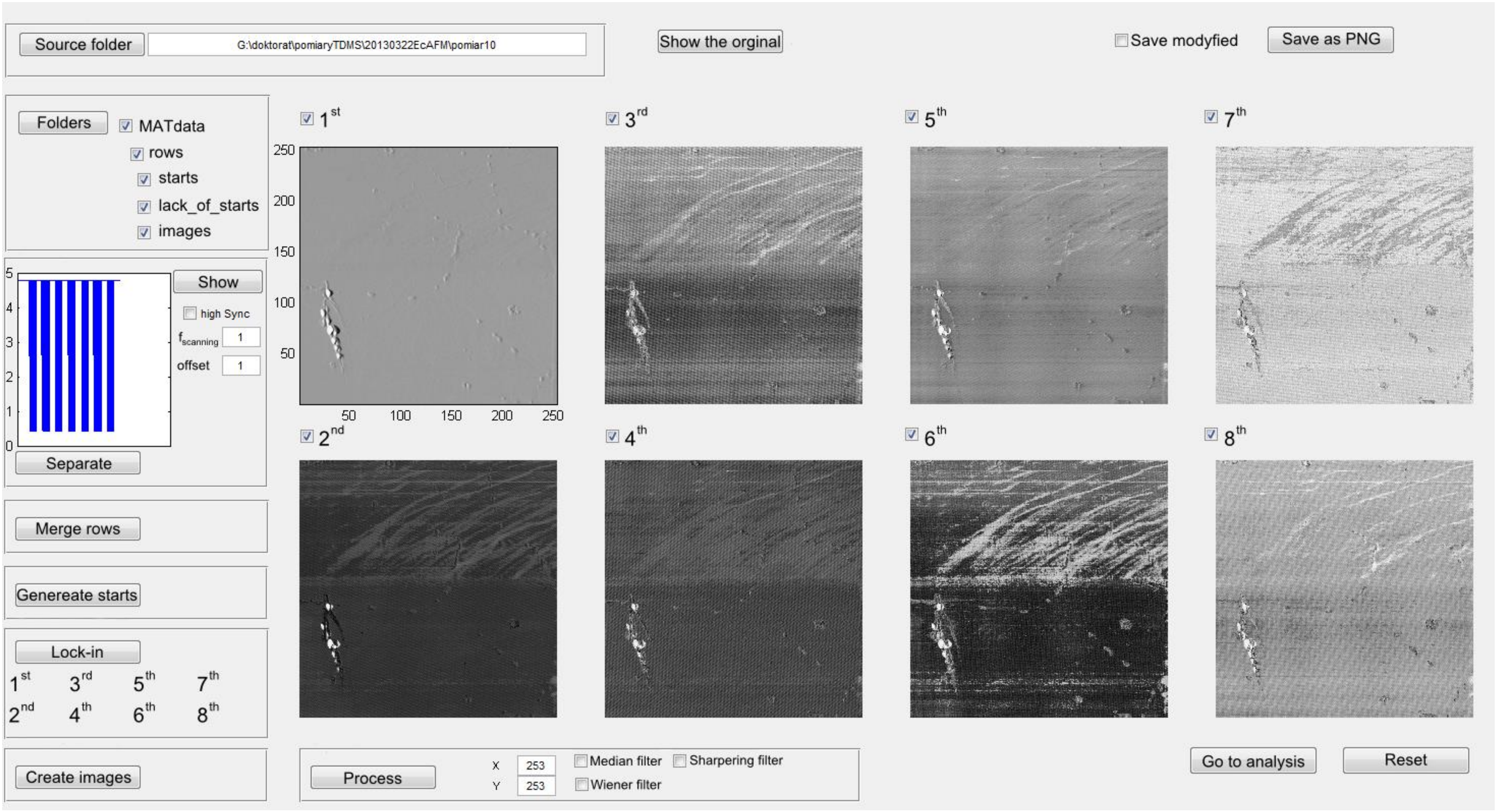

G:\doktorat\pomiaryTDMS\20130322EcAFM\pomiar10

$f_{scanning}$ 1

offset 1

X 253

Y 253

Fig. 3.5 The graphic user interface of the created processing software [102]

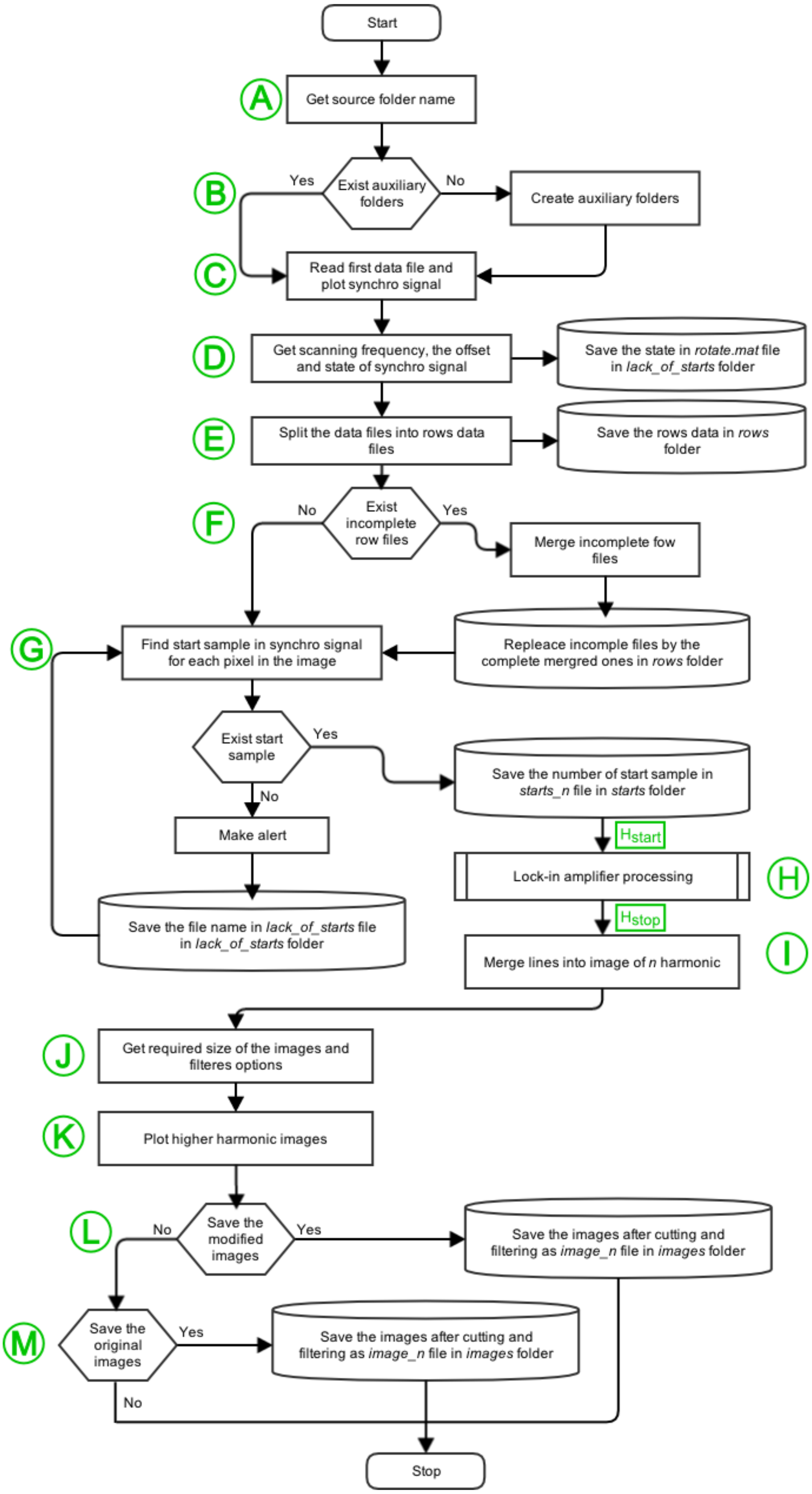

Fig. 3.6 A block diagram of the created program; the detailed algorithm of the lock-in amplifier (the block *H*) is presented in Fig. 3.7

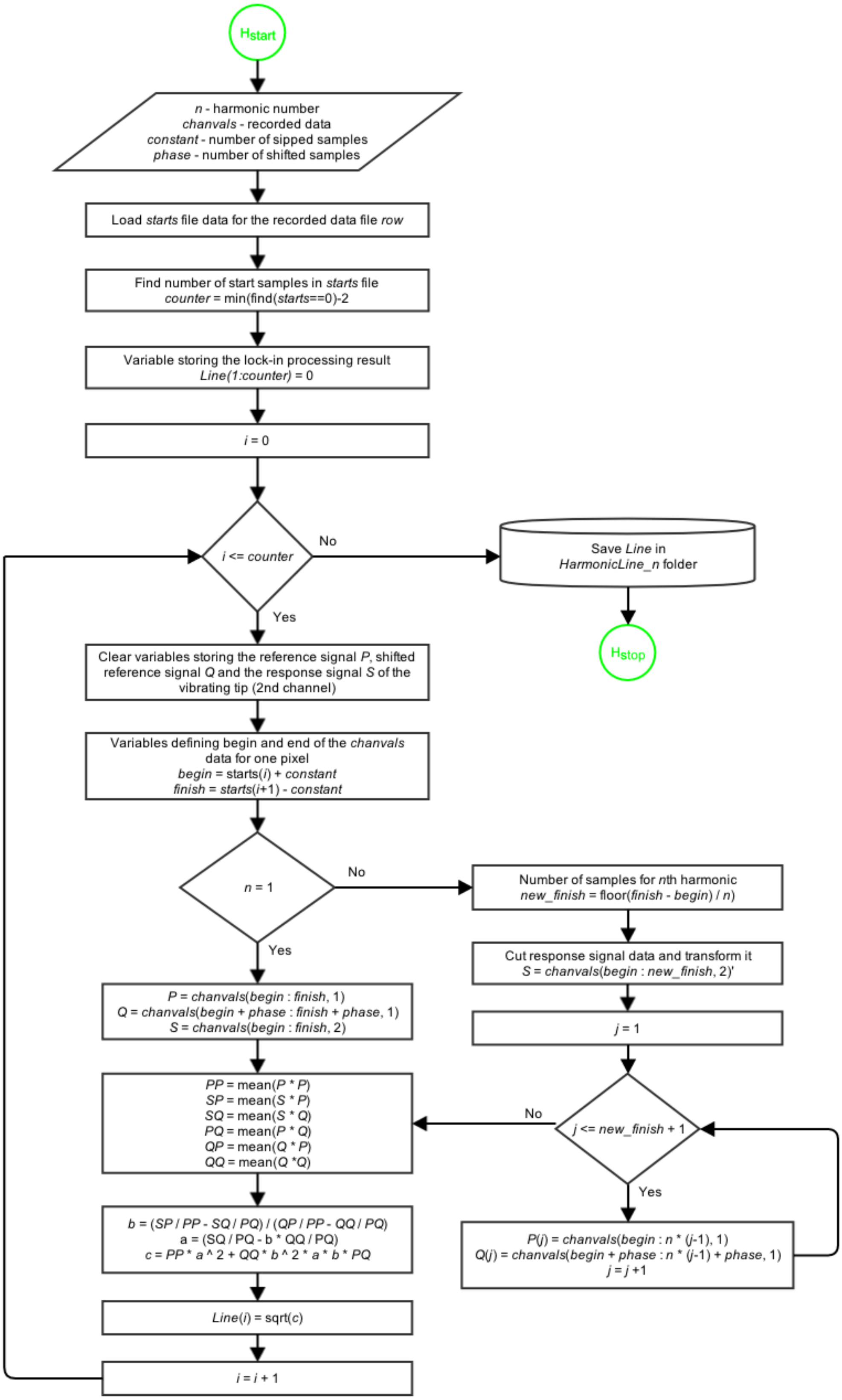

Fig. 3.7 A block diagram of the created algorithm of the lock-in amplifier

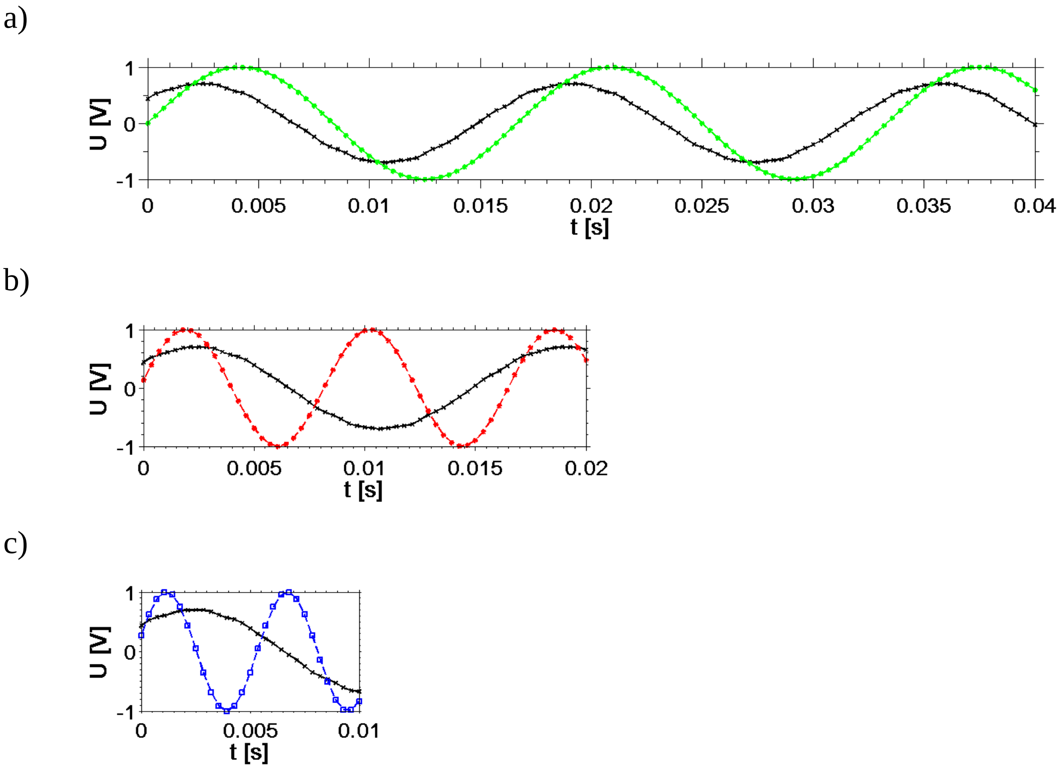

Fig. 3.8 The principle of the lock-in post processing method: a) the output signal (black cross solid) and the original reference signal (green star solid), b) the output signal (black cross solid) and the reference signal made by selecting each 2nd sample from the original reference signal (red star dashed); c) the output signal (black cross solid) and the reference signal made by selecting each 3rd sample from the original reference signal (blue square dashed)

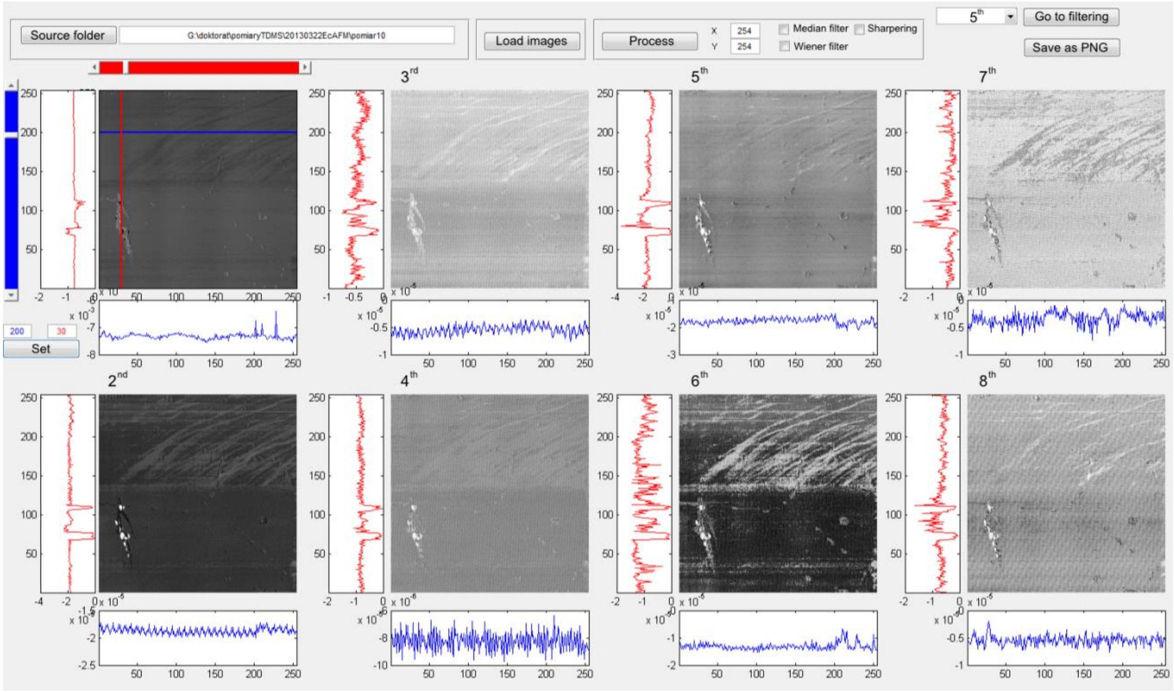
Source folder G:\doktorat\pomiaryTDMS\20130322EcAFM\pomiar10

X 254
Y 254
☐ Median filter ☐ Sharpering
☐ Wiener filter

5th

200 30

Fig. 3.9 The graphic user interface of the software for analysis of the generated images [102]

The most intense disturbances in the considered images are periodic and are independent from the examined topography. Such disturbances can be removed effectively by considering the spectrum averaged over the set of all available rows or columns. For the image matrix of size *M* x *N*:

$$\begin{bmatrix} q(1,1) & q(1,2) & \dots & q(1,N-1) & q(1,N) \\ q(2,1) & q(2,2) & \dots & q(2,N-1) & q(2,N) \\ \dots & \dots & \dots & \dots & \dots \\ q(M-1,1) & q(M-1,2) & \dots & q(M-1,N-1) & q(M-1,N) \\ q(M,1) & q(M,2) & \dots & q(M,N-1) & q(M,N) \end{bmatrix} \tag{3.14}$$

the spectrum of the *i*-th row can be described as:

$$A_{r_i}(k) = \sum_{j=1}^{N} q(i,j) \cdot e^{-\sqrt{-1}\left(\frac{2\pi}{N}\right) \cdot k \cdot j} \quad \text{for } k = 0, 1, \dots, N\text{-}1 \tag{3.15}$$

Next, the average module of the row spectrum (3.16) is given by:

$$|A_r(k)| = \frac{1}{M}\sum_{i=1}^{M}\left|A_{r_i}(k)\right| = \frac{1}{M}\sum_{i=1}^{M}\left|\sum_{j=1}^{N} q(i,j) \cdot e^{-\sqrt{-1}\left(\frac{2\pi}{N}\right) \cdot k \cdot j}\right| \text{for } k = 0, 1, \dots, N\text{-}1 \tag{3.16}$$

Similarly, for the columns:

$$|A_c(k)| = \frac{1}{N}\sum_{j=1}^{N}\left|A_{c_j}(k)\right| = \frac{1}{N}\sum_{j=1}^{N}\left|\sum_{i=1}^{M} q(i,j) \cdot e^{-\sqrt{-1}\left(\frac{2\pi}{N}\right) \cdot k \cdot i}\right| \text{for } k = 0, 1, \dots, M\text{-}1 \tag{3.17}$$

The periodic character of disturbances suggests that the average spectrum of rows and columns should exhibit peaks responsible for the distortion pattern present in the analysed picture as a mesh. The peaks attenuated in the analysed spectra can be selected manually by choosing the peaks with amplitudes clearly higher than the background level. The peaks are removed by replacing them with averaged adjacent values. The final image is obtained by applying the inverse Fourier transform from the frequency domain to the image space domain. Such operation can be performed by using functions available in the graphic user interface and filtration software (Fig. 3.10).

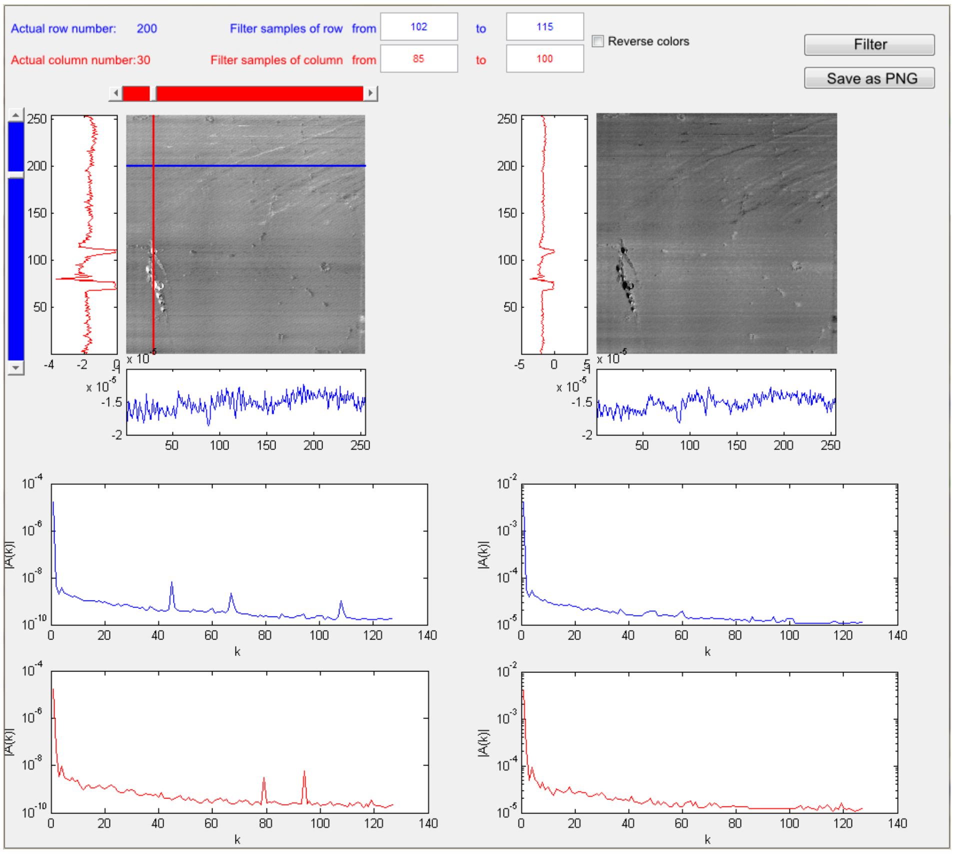

Actual row number: 200

Filter samples of row from 102 to 115

Actual column number:30

Filter samples of column from 85 to 100

☐ Reverse colors

Fig. 3.10 The graphical user interface of the filtration software

The image subjected to filtration can be selected in the graphic user interface presented in Fig. 3.9. In the next step, the filtration software presents two pictures: the original image on the left and the filtered image on the right (Fig. 3.10). It is possible to observe the picked row (the blue plot below the image) and column (the red plot on the left of the image) of the original and filtered images. The observed row and column can be changed by independent sliders. Below the images two average modules of the spectra are presented: the blue one for rows and the red one for columns. The user determines the range subjected to filtration for a row and a column. The peak is replaced during filtering with the mean value obtained from the preceding and following values of the spectra.

3.2 The measurement system – version 2

3.2.1 The data acquisition unit

The second version of measurement system has been developed by replacing the USB-6356 with the PXI-5122 data acquisition board (Fig. 3.11).

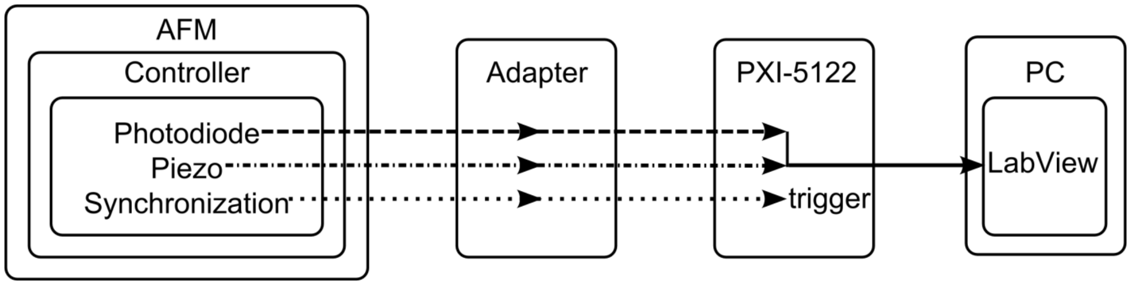

Fig. 3.11 A scheme of the modified measurement system (version 2)

The PXI-5122 board is triggered by the synchronization signal which can be not recorded. That amendment significantly reduces the size of saved data. The LabView control program saves the excitation (Piezo) and the answer (Photodiode) signals for all pixels and saves them in the TDMS file.

3.2.2 The data processing software

The method of organizing data storage for the PXI-5122 board has eliminated several steps of the algorithm used in the case of the USB-6356 board (Fig. 3.6) and makes it much more time-efficient. The higher-harmonic image is created and saved in the *images* folder directly after the lock-in amplifier processing. Similarly, in the graphic user interface of the processing software (Fig. 3.5), after selecting a source folder and higher-harmonic numbers, the images created by the lock-in amplifier processing are plotted and can be further processed. The other two graphic user interfaces (for analysis – Fig. 3.9, and filtration – Fig. 3.10) remain unchanged.

The applied PXI-5122 board has reduced the number of recorded data to such an extent that the lock-in processing of the recorded data can be performed in real time during surface scanning. Thus, it is possible to immediately verify the measurement results and, if necessary, change the measurement parameters. The number of generated higher-harmonic images is limited by the computational speed of the controlling computer and the applied excitation frequency. The images for consecutive higher harmonics were generated typically up to the 8th harmonic.

4 The experimental results

This chapter reviews numerous measurement results obtained for selected objects having various properties. Firstly, the ZnO varistors were scanned (Chapter 4.1). The experiments were performed on two batches of ZnO structures. The main difference between the batches was their composition. The structures consisted of ZnO grains having different electrical and physical properties. Therefore, their higher-harmonic images should have a potential to reveal some differences in their surface structures. The AFM was verified as a tool for non-destructive testing of the ZnO varistor structures. The results of testing ZnO varistors by the higher-harmonic imaging using the proposed measurement system (Chapter 3.1) are presented in the next part of the chapter. Then, the measurement system has been used to visualize heterogeneous surfaces (Chapter 4.2).

Another examined inhomogeneous surface was austenitic steel AISI304. That experiment was continued by monitoring the corrosion process using the higher-harmonic imaging. A series of measurements were performed when the steel corroded at accelerated conditions (Chapter 4.3). The developed measurement system (Chapter 3.2) was used for the higher-harmonic imaging during inducing the corrosion process on austenitic steel AISI304 (Chapter 4.3). The final section of this chapter considers problems of various interferences present in the higher-harmonic imaging (Chapter 4.4).

4.1 Analysis of ZnO varistor heterogenity

The ZnO varistors have a strongly non-linear current–voltage characteristic and therefore are used to protect electrical circuits and networks against excessive voltage transients by shunting the current in power supply lines [104]. The cylindrically-shaped ZnO structures are typically used for varistors working at various voltage ranges. Their properties depend on technological conditions at different production stages, like their shaping or firing in an oven (the way of the ZnO grains milling, mixing and squeezing). Microstructural heterogeneity determines performance of ZnO-based varistors. The non-linear characteristic depends on the grains and electrical contacts between them. The grains differ in geometry and are very similar with respect to their chemical composition, but have different electrical properties. A highly non-linear characteristic of ZnO structure is determined by the biggest grains. The grains assuring contacts close to ohmic are relatively smaller. Their different electrical properties should mean some differences in their other physical properties, like stiffness. The grain size can be controlled by the sintering temperature, its time profile and also by some additives. A higher sintering temperature and longer sintering times increase the grain size and result in a more non-linear current–voltage characteristic [105]. Thus, examining the ZnO structure by higher-harmonic images would be interesting because we can expect differences in the grain sizes and physical properties.

Two batches (the good quality specimens #*A* and #*B* and the poor quality specimens #*C* and #*D*) were prepared for testing. There was a significant difference between the amount of grains having linear and non-linear junctions in each group as a result of the introduced technological changes, as happens accidentally in their production. The aggregated grains formed structures which determined the final current–voltage characteristics, having visible differences between both groups of varistors. One of the batches could be treated as a group of varistors having poor quality – with a more intense leakage current and a less non-linear current–voltage characteristic. The grainy surface structures were examined by the AFM to identify differences in distribution of grain sizes between the prepared batches. The exemplary images of scanned surfaces (having dimensions of 50 μm x 55 μm) are shown in Fig. 4.1 and Fig. 4.2. The well-prepared ZnO structures (Fig. 4.1) consist of bigger grains having non-linear current–voltage junction characteristics.

The good quality specimens (Fig. 4.1) are characterized by distinct and large grains. The structures are clearly heterogeneous within the entire surface. Tiny grains are also observed, but are not so abundant as in the case of specimens from the second batch. The legend of the Fig. 4.1 uses greyscale, having 0÷255 levels. The levels correspond with the measured currents [nA] (left side of the legend) or height [μm] (right side of the legend). The same rule was assumed for all the corresponding figures in the thesis.

The poor quality specimens #*C* and #*D* (Fig. 4.2) have smaller grains than the good quality specimens #*A* and #*B*, scattered around the centre of specimen's material. The grains' height of good quality specimens #A and #B is more uniformly distributed when compared with the poor quality batch.

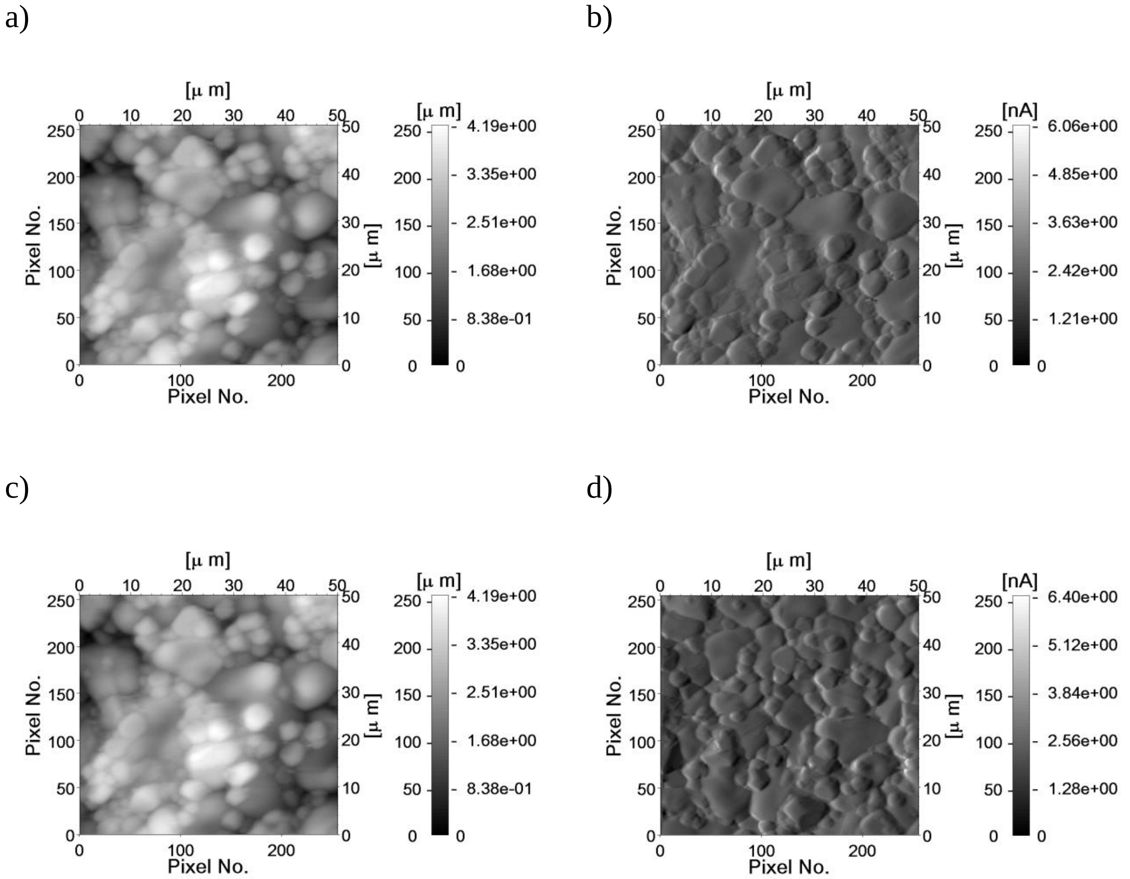

Fig. 4.1 The NOVA software images of good quality varistor specimens: a) the specimen #*A* topography, b) the specimen #*A* DFL image, c) the specimen #*B* topography, d) the specimen #*B* DFL image

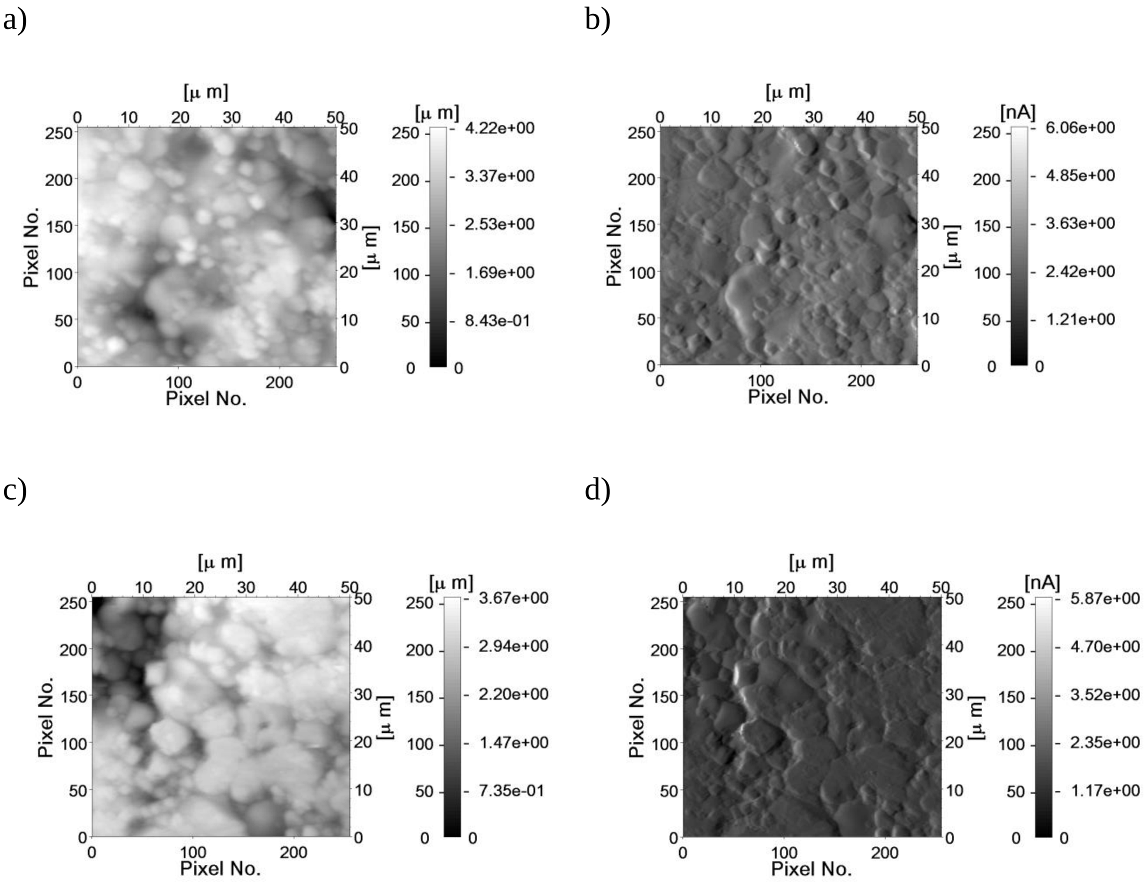

Fig. 4.2 The NOVA software images of poor quality varistor specimens: a) the specimen #C topography, b) the specimen #C DFL image, c) the specimen #D topography, d) the specimen #D DFL image

The differences between the batches are more visible when the histograms of surface height distribution are compared. The histograms (Fig. 4.3) of good quality specimens #*A* and #*B* have a symmetrical distribution more similar to the Gaussian distribution. The histograms of poor quality specimens #*C* and #*D* are shifted to higher values. It can be concluded that the poor quality specimens #*C* and #*D* have extensively high points, but their number is more limited – the maximum of height distribution at 3000 nm (e.g. Fig. 4.3d) is narrower than the maximum observed for the good quality specimens (Fig. 4.3a, Fig. 4.3b). We can suppose that the space between these grains is filled with smaller grains, as seen in the histogram in Fig. 4.3d. Such small grains, having ohmic contacts, influence strongly the current–voltage characteristic between the terminals of the structure.

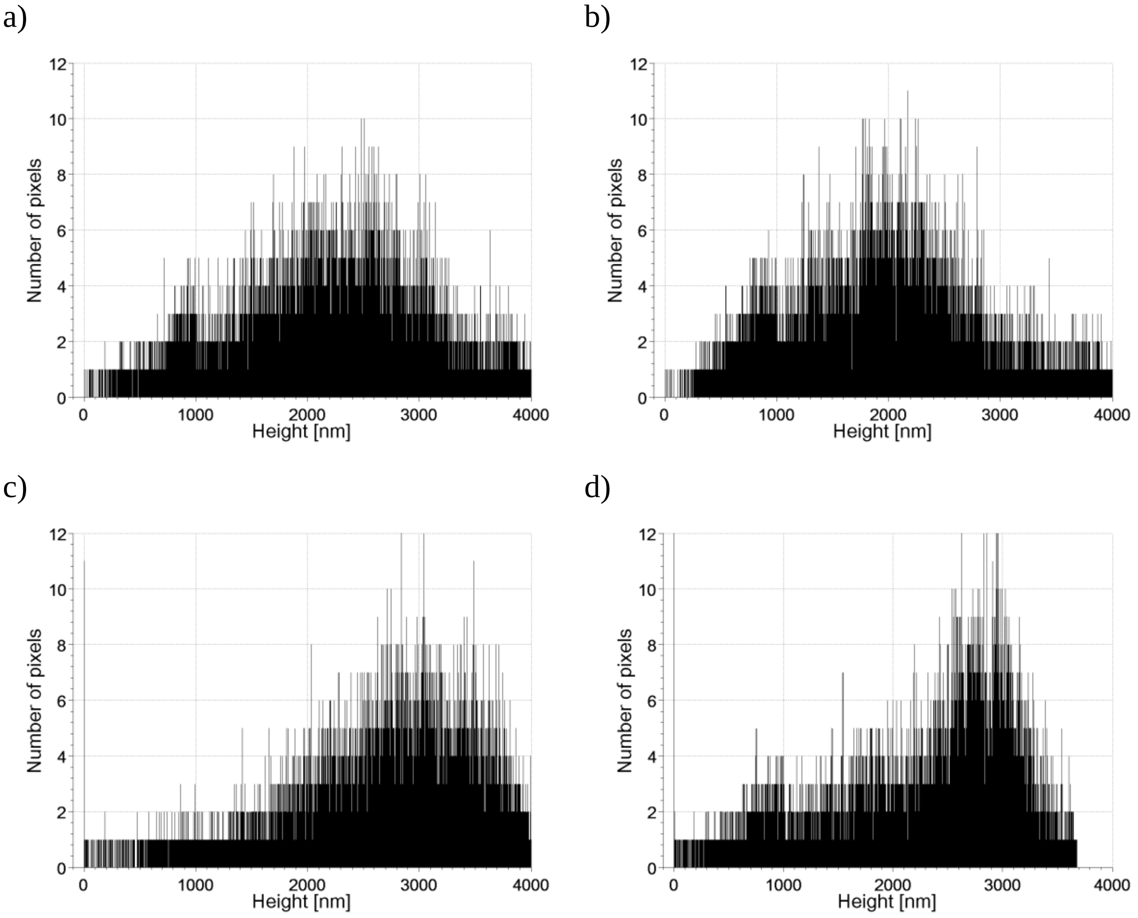

Fig. 4.3 The histograms of grains’ heights of good quality specimens a) *#A* or b) *#B*, and poor quality specimens c) *#C* or d) *#D*

The diameter and volume of grains were estimated by the NOVA software. Before the analysis, the grains’ edges were detected by a Laplace filter (Fig. 4.4, Fig. 4.5). After filtering, the difference between the batches was clearly noticeable even by comparing the images visually.

After detection of grains in the examined specimens, it is possible to analyse their basic statistical parameters, like their grains’ average size, volume, maximum and mean height, average circumference, and diameter (Tab. 4.1). All these parameters are available in the module of statistical surface analysis in the NOVA software.

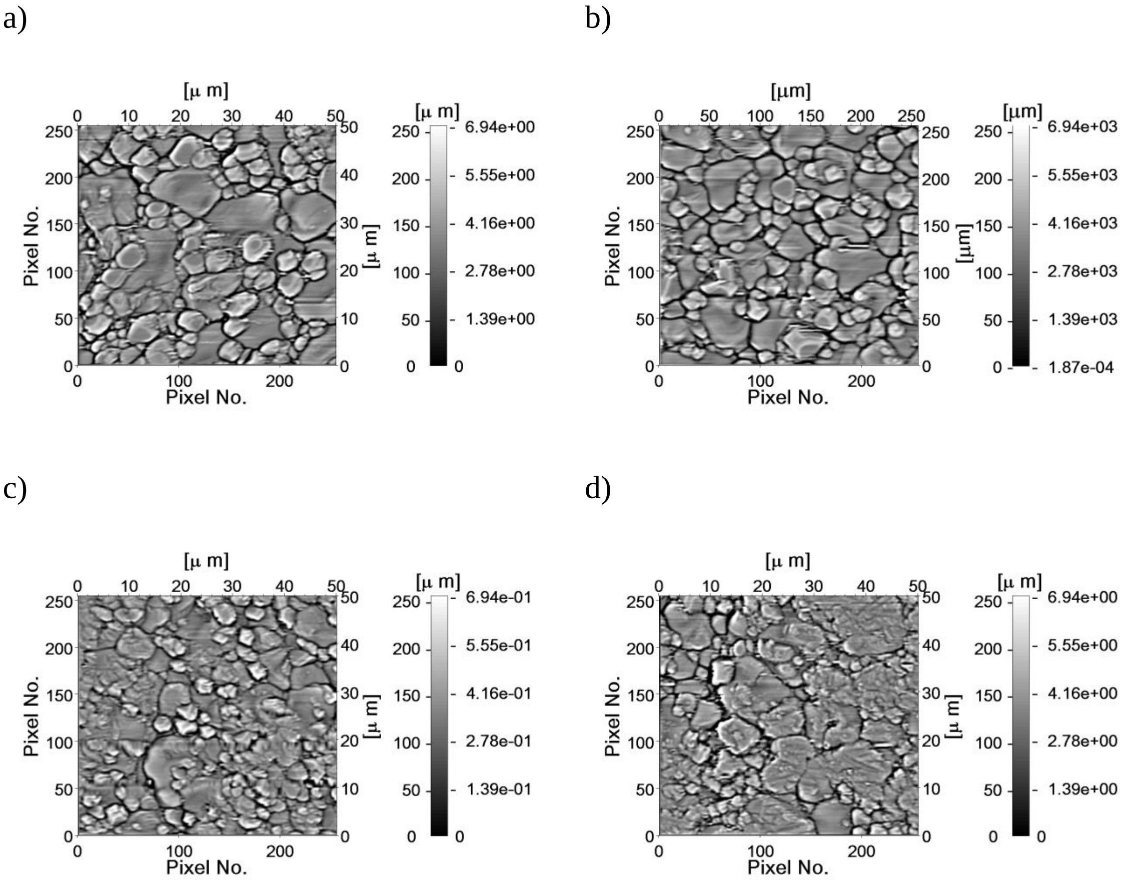
a) b) c) d)

Fig. 4.4 The topography images after 5 x 5 Laplacian filtering: a) the good quality specimen #*A*, b) the good quality specimen #*B*, c) the poor quality specimen #*C*, d) the poor quality specimen #*D*

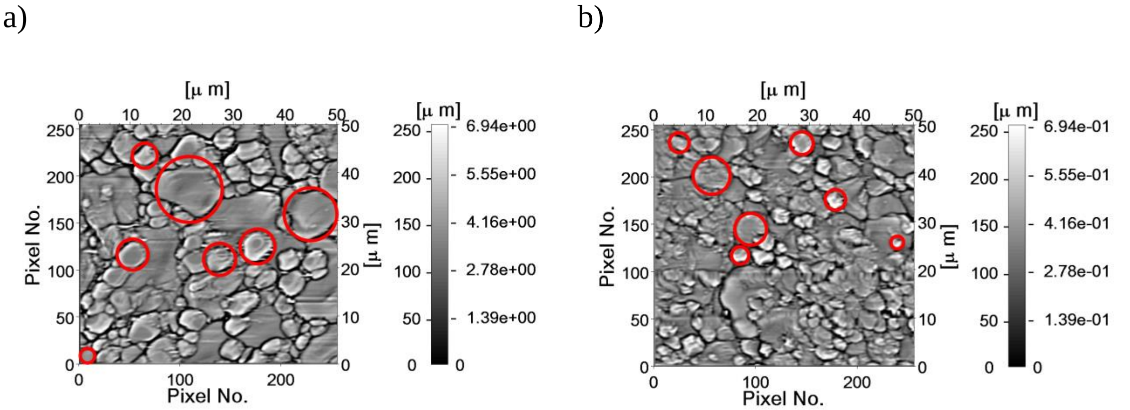
a) b)

Fig. 4.5 The topography of ZnO surface after Laplace filtering with marked examples of grains of a) the good quality specimen (specimen #*A*), b) the poor quality specimen (specimen #*C*) with marked examples of detected grains

On the basis of these results, it can be concluded that the good quality specimens (#*A* and #*B*) consist of a smaller number of very large grains. It is proved by the larger average size, volume, circumference and diameter of the grains in the examined structures. At the same time, for all four specimens, the maximum height and the average height are comparable.

Tab. 4.1 The statistical values of grains in the examined varistor specimens

	Good quality		**Poor quality**	
	specimen #A	**specimen #*B***	**specimen #*C***	**specimen #*D***
number of structures	259	211	317	277
size [µm x µm]	5.52	6.94	4.10	4.83
volume [µm x µm x µm]	12.32	15.61	9.16	10.82
max. height [µm]	2.61	2.62	2.57	2.64
mean height [µm]	2.12	2.10	2.09	2.13
circumference [µm]	11.94	14.49	10.57	13.71
diameter [µm]	1.76	2.15	1.57	1.57

The observed differences in the specimens' structures can be characterized with a few additional statistical parameters. They include: roughness, the root mean square, the peak-to-peak value, Ten Point Height, the asymmetry of distribution and kurtosis. All these parameters are available in the module of statistical surface analysis in the NOVA software (Tab. 4.2).

Roughness S_a is the mean value of height of all topography points [106]:

$$S_a = \frac{\sum_{i=1}^{M}\sum_{j=1}^{N}|q(i,j)|}{M \cdot N}, \tag{4.18}$$

where:
M – the number of pixels in OX direction,
N – the number of pixels in OY direction,
$q(i,j)$ – the height in the point (i,j) [nm].

The root mean square (also known as the quadratic mean) of topography of all points was estimated according to the formula [106]:

$$S_q = \sqrt{\frac{\sum_{i=1}^{M}\sum_{j=1}^{N}\left|q(i,j)\right|^2}{M \cdot N}} \tag{4.19}$$

The peak-to-peak value is the difference between the maximum $q_{\max}$ and the minimum $q_{\min}$ values [106]:

$$S_y = q_{\max} - q_{\min} \tag{4.20}$$

Ten Point Height is the mean value of a module of five highest q_{p_k} ($k = 1, \dots, 5$) and lowest q_{v_m} ($m = 1, \dots, 5$) points within the analysed image [106]:

$$S_{10z} = \frac{\sum_{k=1}^{5}\left|q_{p_k}\right| + \sum_{m=1}^{5}\left|q_{v_m}\right|}{10} \tag{4.21}$$

Skewness S_{sk} is the third statistical moment, qualifying the symmetry of height distribution:

$$S_{sk} = \frac{\sum_{i=1}^{M}\sum_{j=1}^{N} q(i,j)^3}{M \cdot N \cdot S_q^{\,3}} \tag{4.22}$$

A negative skewness ($S_{sk} < 0$) indicates that the surface is composed of principally one plateau and deep and fine valleys. In this case, the distribution is sloping to the top. A positive skewness ($S_{sk} > 0$) indicates a surface with lots of peaks on a plane. The distribution is sloping to the bottom [107].

Kurtosis S_{ku} is the fourth statistical moment qualifying the flatness of probability distribution. This parameter reflects how evenly the measured profile heights are spread. For spiky surfaces, $S_{ku} > 3$; for bumpy surfaces, $S_{ku} < 3$ [107]:

$$S_{ku} = \frac{\sum_{i=1}^{M}\sum_{j=1}^{N} q(i,j)^4}{M \cdot N \cdot S_q^{\,4}} \tag{4.23}$$

The considered statistical parameters are gathered in Tab. 4.2. We can conclude that the poor quality specimens #*C* and #*D* have a smaller mean height S_a and a smaller root mean square of topography S_q than the good quality specimens #*A* and #*B*. At the same time, the distribution asymmetry S_{sk} gives rise to the conclusion, that the poor quality specimens #*C* and #*D* are characterized by a greater number of cavities.

Tab. 4.2 The estimated statistical parameters of the specimens' surface height distribution

Parameter	**Good quality**		**Poor quality**	
	specimen #*A*	**specimen #*B***	**specimen #*C***	**specimen #*D***
z_{max} [nm]	4183.47	4012.13	4188.77	3673.56
z_{min} [nm]	0	0	0	0
S_a [nm]	570.683	531.474	514.741	526.189
S_q [nm]	706.113	675.765	642.802	665.991
S_y [nm]	4183.47	4012.13	4188.77	3673.56
S_{10z} [nm]	2103.21	2016.88	2093.2	1835.4
S_{sk}	-0.0495	0.2139	-0.5798	-0.9707
S_{ku}	-0.2883	0.0488	0.3711	0.6095

All the presented statistical studies confirmed that there is a clear difference between the surface topography of the considered good and poor quality specimens. The images (Fig. 4.1) created by the AFM show that the good quality varistors (specimens #*A* and #*B*) are characterized by a coarse-grained structure, in which the grains are embedded densely and closely, and variation of height between the grains is significant.

Quality of ZnO varistors may be also assessed using other tools, based on 1/*f* noise intensity or selected electrical characteristics [104]. The 1/*f* noise properties are related to electrical characteristics of multiple micro-events causing voltage fluctuations inside the specimens of ZnO varistors because of fluctuations in the potential barrier between grains, and thus giving more distinctive results than their DC voltage–current characteristics. Significant differences in electrical properties between the specimens of good and poor quality can be also observed in current–voltage characteristics (Fig. 4.6). The specimens of poor quality saturate at a significantly lower voltage (have a greater leakage current at the same bias voltage). Such differences between the specimens can be identified by measuring either non-linearity of their characteristic or intensity of the third harmonic components when the varistors are stimulated by a harmonic voltage [108].

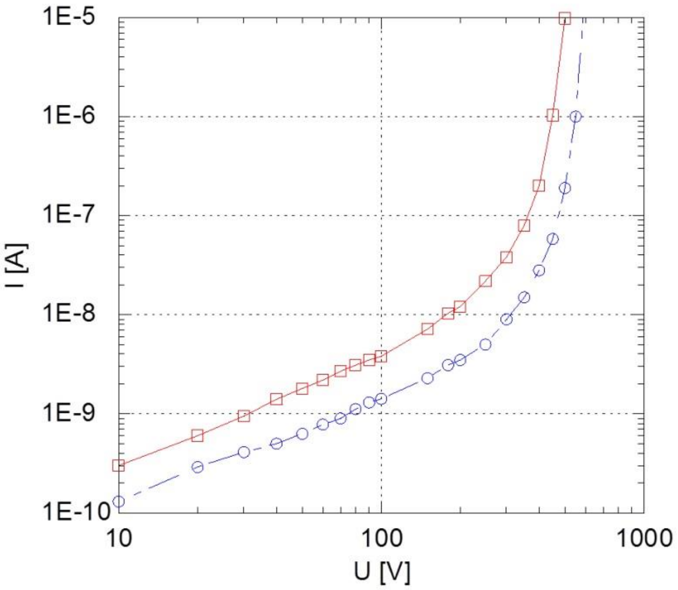

Fig. 4.6 The current–voltage characteristics of exemplary varistor specimens of poor (red squares) and good (blue circles) quality; the tested specimens were designed for working at voltage 280 V [104]

The characteristic depends on the grains' geometry and chemical composition. The non-linear characteristic is determined by the biggest piezoelectric-built grains. Smaller grains have their characteristics close to ohmic. Different physical properties, like stiffness, are a natural consequence of their electrical and chemical properties resulting from the building material. Diverse materials, with different stiffness, cause changes in the tip-sample contact forces during the AFM scanning. Variations in the tip-sample contact result in different levels of higher harmonics. Thus, it is reasonable to examine quality of varistors with the higher-harmonic imaging.

The higher-harmonic surface imaging enables to obtain clear images only for good quality specimen #*A* measurements (Fig. 4.7 and Fig. 4.8). This is caused by diversification in the building material– the piezoelectric large grains interact to a greater extent with the scanning tip. In the opposite – the ohmic areas, because of their different stiffness, have less non-linear characteristics what worsens the higher-harmonic imaging process. Consequently, the higher-harmonic images of the poor specimen #*C* have been too noisy and unclear during numerous trials.

In the case of highly diversed areas, with distinct and well developed grains, the higher-harmonic imaging clearly differentiates the grains responsible for ohmic or non-linear contacts (Fig. 4.8).

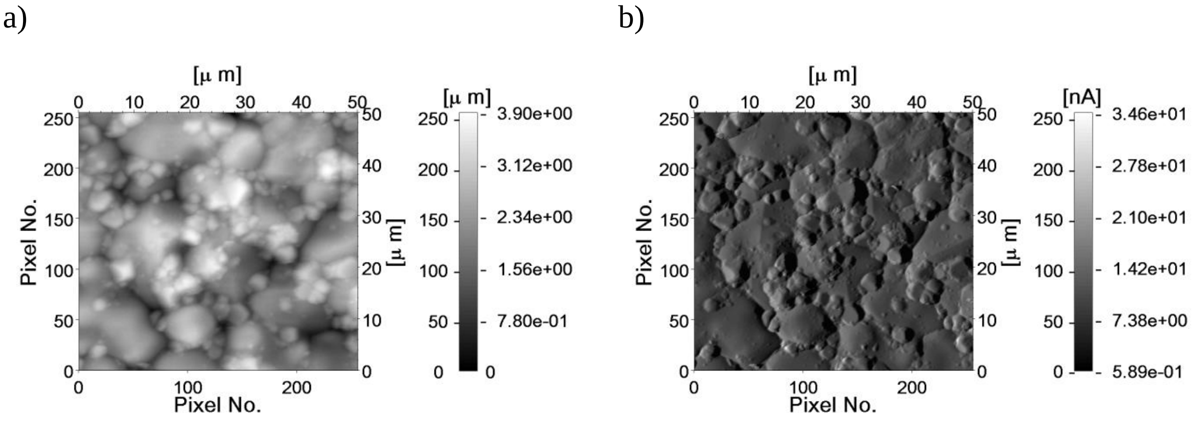

Fig. 4.7 The NOVA software images of the good quality varistor specimen #*A*: a) topography, b) DFL (control error)

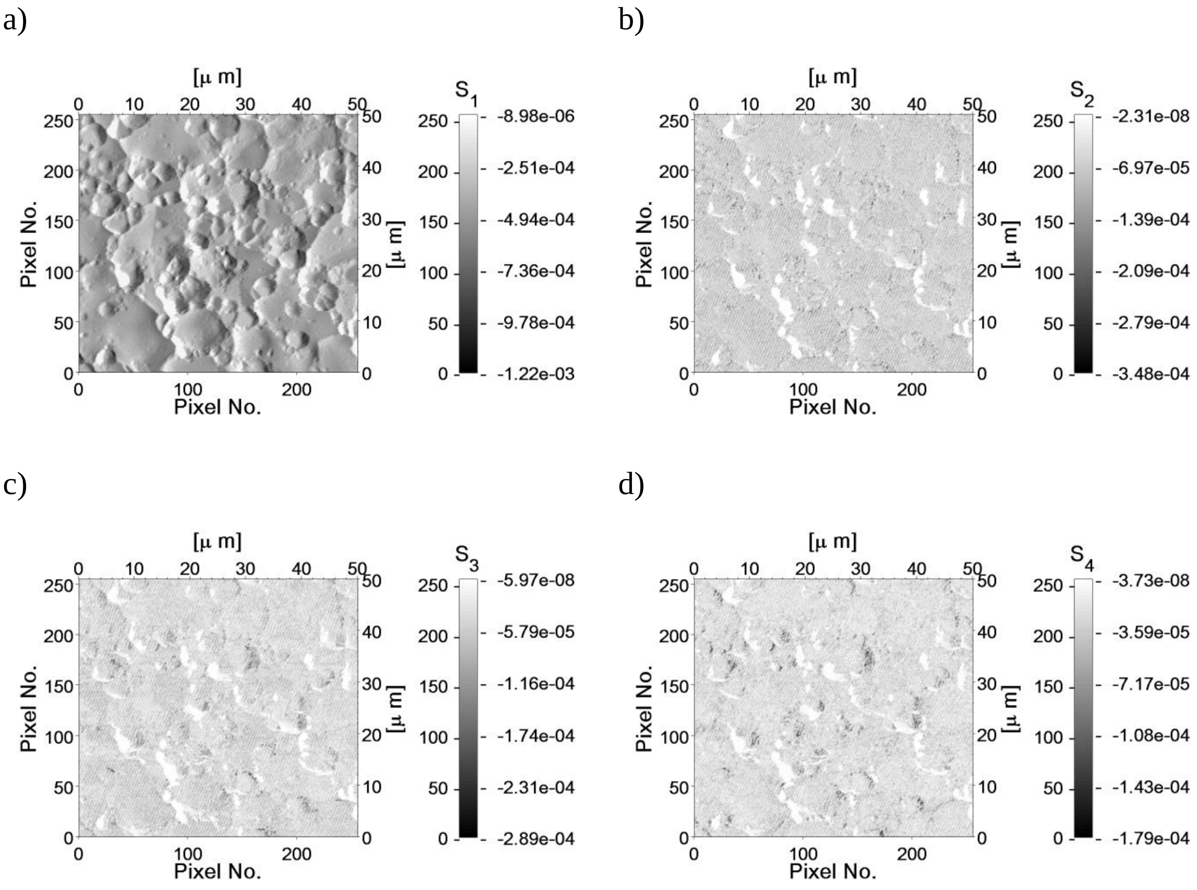

Fig. 4.8 The higher-harmonic images of the good quality varistor specimen #*A*: a) 1st, b) 2nd, c) 3rd, d) 4th harmonic image

The undesirable ohmic grains are clearly visible between the well-developed grains having piezoelectric properties as white regions spread over the image. The contrast between such grains is more visible for the higher-harmonic images (e.g. the 2nd and higher harmonics – Fig. 4.8b) than for the DFL image (Fig. 4.7b).

Thus, that result confirms that the higher-harmonic imaging by the AFM can be effectively used to determine properties and quality of ZnO varistors.

4.2 The higher-harmonic imaging of glass and resin heterogeneous surfaces

The next measurements were carried out on a specimen consisting of resin with embedded glass fiber (Fig. 4.9). It is also possible to visualize the specimen in three dimensions NOVA software (Fig. 4.10), where two different materials with various physical properties may be easily distinguished.

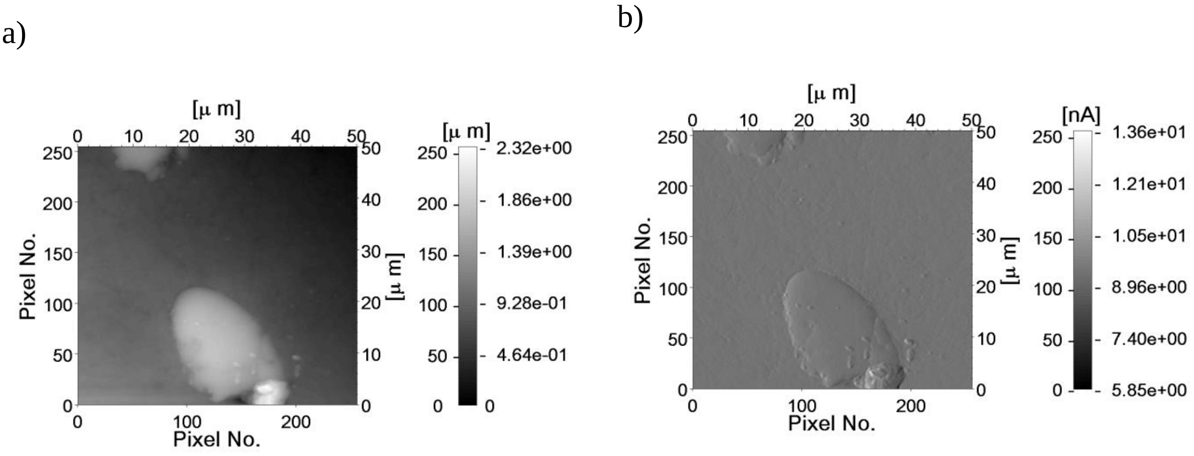
a)

b)

Fig. 4.9 The images of glass fiber in resin derived by the NOVA software: a) topography, b) DFL (control error)

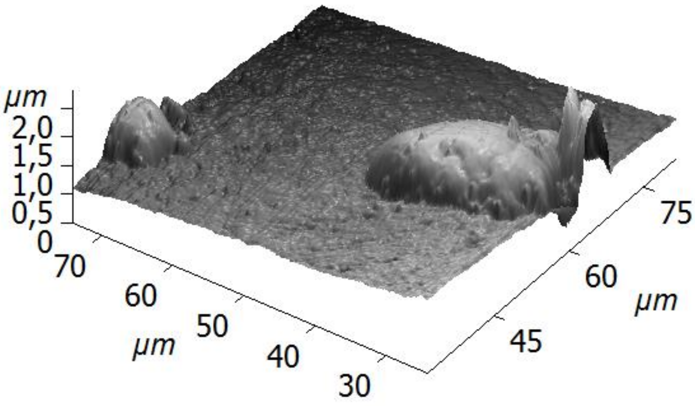

Fig. 4.10 The three dimension picture of the specimen consisting of glass fiber embedded in resin

The higher-harmonic images (Fig. 4.11) were obtained by applying the measurement setup with the USB-6356 board. Thus, the highest order of the observed harmonic was $n = 6$. Significant interferences were seen in pictures, starting from the third harmonic. Intensity of the interferences was especially visible in the fifth harmonic image (Fig. 4.11e). Despite this, in the 2nd and the 6th harmonic images heterogeneous parts of larger fiberglass in the centre bottom could be easily identified. Such a difference is not visible in topography and DFL (control error) pictures (Fig. 4.12).

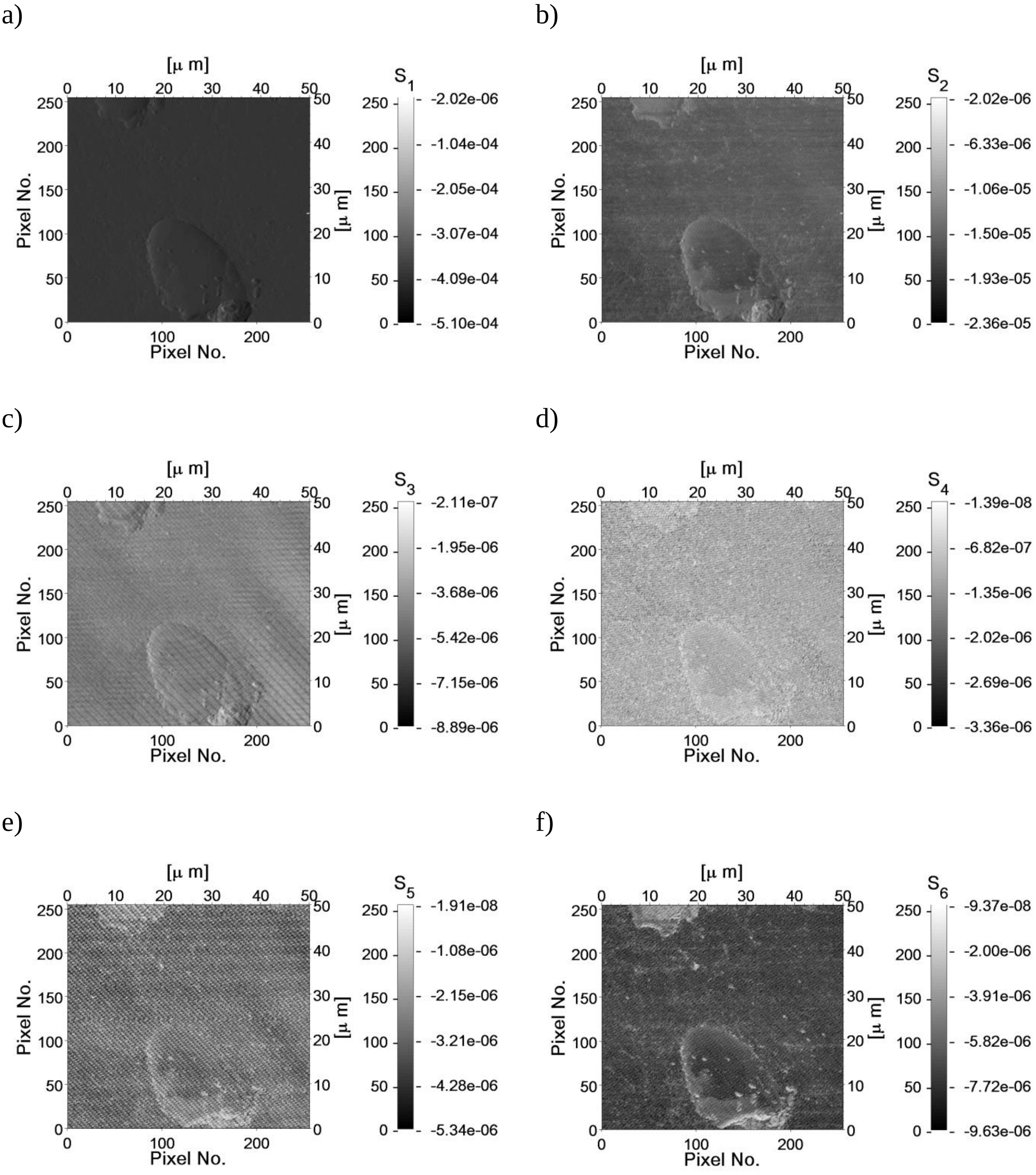

Fig. 4.11 The higher-harmonic images of glass fiber embedded into resin: a) 1st, b) 2nd, c) 3rd, d) 4th, e) 5th, f) 6th harmonic

a)

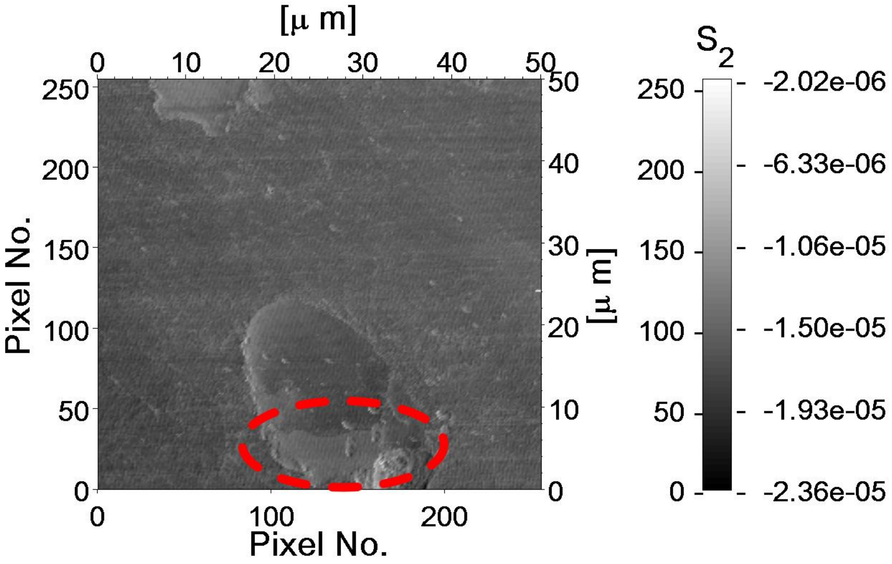

b)

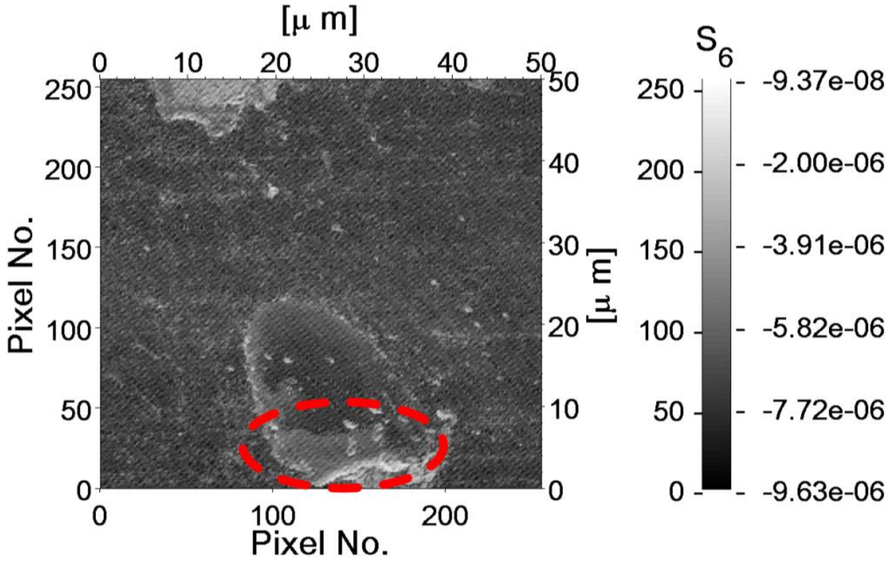

Fig. 4.12 The images of: a) the 2nd, b) the 6th harmonic with the marked area which is invisible in topography and DFL (control error) pictures (Fig. 4.11)

It can be concluded that the higher-harmonic imaging can be successfully applied to gather more information about examined specimens [109]. The 2nd (Fig. 4.12a) and the 6th (Fig. 4.12b) harmonic images emphasize some elements of topographical substructures (slight differences inside the glass area) which are invisible in the typical pictures created with the dedicated software (Fig. 4.9). Thus, it can be assumed that the presented surface imaging method can be successfully applied to characterize also corroding surfaces. The corrosion products (oxides) are characterized by different stiffness and other physical quantities than those of metallic surfaces. Moreover, a certain area - locally charged due to varied corrosion intensity and its stages - should be also present on the specimen surface. The charged area will influence the force between the specimen and the tip - and therefore induce non-linear effects having various intensity. As a result, such a method would characterize the corroding specimen to assure additional information about efficiency of anticorrosion protection and to monitor its changes during corrosion processes, controlled by potential-static methods. These issues are considered in the experimental studies presented in the next point.

4.3 Monitoring corrosion processes by the higher-harmonic imaging

Steel is a very important construction material. Unfortunately, its quality and use is limited because of its heterogeneous structure, due to treatment and local corrosion effects. Costs of steel protection and conservation are very high [110]. Thus, it is important to test new alloys and protective coatings efficiently, quickly and accurately by observing even very subtle changes on their surfaces. Especially, the inter-granular corrosion (IGC) is very harmful for steel constructions and therefore requires careful attention to be identified at a preliminary stage. The atomic force microscopy can be applied to analyse a metal surface in nanoscale, to recognize any heterogeneity resulting in corrosion development, and to understand its mechanism.

The higher-harmonic imaging is especially helpful for sharpening boundaries between objects in heterogeneous samples [12]. That fact can be used to identify variations in steel structures (e.g. corrosion products, steel heterogeneity). The corrosion products have different chemical structures because they are composed of chemicals other than the original metal base (mainly iron oxides [111]). Thus, their elastic properties are different from the primary basis. These structures have edges at which higher harmonics should be more intense because of stronger interference between the tip and the specimen structure there [52].

Austenitic stainless steels (containing 18% chromium and 8% nickel) exhibit a high general and localized corrosion resistance. This is often the key factor in their choosing to work in aggressive chemical environments, or in nuclear and conventional power plants (e.g. steam turbines), despite relatively poor mechanical properties of these steels [112]. A good corrosion resistance results from addition of chromium, with its protective effect observed when the content exceeds the critical value of 13%. On the other hand, the range of useful operating temperatures of the aforementioned steels is limited by the phenomenon of thermal sensitization leading to subsequent inter-granular corrosion attacks [113, 114].

It is important to consider what type of corrosion products can be created on a steel surface. Physical properties of the arising corrosion products would determine possible applications of the higher-harmonic images. According to the widely accepted depletion theory [115], it is assumed that exposure to temperatures in the range of 425÷815°C during welding or working lifetime leads to precipitation of carbides (such as $Cr_{23}C_6$) or intermetallic phases at the grain boundaries [116]. This phenomenon promotes forming chromium-depleted regions in their vicinity. $Cr_{23}C_6$ carbide is recognized to be responsible for the depletion (chromium reduction) and thereby sensitizing to the IGC [117], which is observed when the chromium content falls below 12-13% [112, 117, 118]. It should be noted that the thermal sensitization of austenitic steels is a process taking place in the solid phase phenomena (diffusion, precipitation and sliding) [118]. Degradation of the material is the effect of the subsequent interaction with the liquid medium governed by an electrochemical mechanism. The chromium-depleted grain boundary region is less resistant to corrosion than the interior of the grain. The preferential weld corrosion takes place at the grain boundaries while the interior of the grains remains passive. Thus, the higher-harmonic images could be used to monitor corrosion development by recognizing the differences at the grain boundaries.

The image of a specimen created by higher harmonics can be used to gather information about the elastic properties of the specimen (stiffness) [52]. Moreover, various substances are much easier distinguishable in non-homogeneous samples, because the higher-harmonic imaging enables clear differentiation of distinct materials

[40, 119]. Higher harmonics can be even more sensitive when compared with the conventional imaging. For example, inclusions in steel have different chemical structures because they are composed of chemicals other than the original metal base and should have slightly different stiffness [111, 113].

The experiment was performed using the NTegra Prima AFM by NT-MDT with an electrochemical adapter (Fig. 4.13). The aim was to test whether it is possible to get higher-harmonic images in the liquid environment using an existing measurement system. The examined specimen was austenitic steel AISI304. The specimen was subjected to temperature sensitization by heating during 1 h in 675°C according to the ASTM standard.

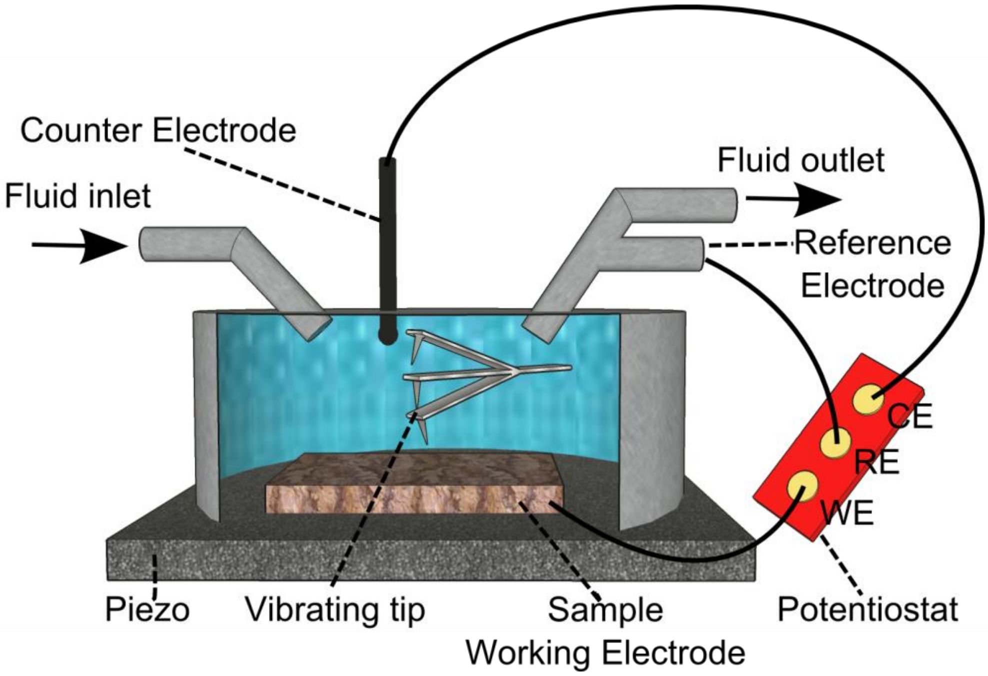

Fig. 4.13 The measurement setup used for monitoring - by the AFM - corrosion of a specimen submerged in aqueous electrolyte

Before the AFM experiment the specimen surface was prepared according to the following scheme. The specimen was subjected to wet grinding on sandpapers of increasing grade (400, 800, 1500 and 2000). In each step, the specimen was ground in perpendicular directions until a visually homogeneous surface was obtained. Then the specimen was rinsed with water with a surfactant and dried in a stream of hot air. The specimen was polished on a rotary polisher with diamond suspension of decreasing size (15 μm, 9 μm and 3 μm). In each step the specimen was polished in perpendicular directions for 15 min. Then the specimen was washed in an ultrasonic washer with deionized water and dried. Next, the specimen was polished with colloidal silica of 50 nm size and washed three times in the ultrasonic washer for 15 min. with exchanging deionized water after each period.

The specimen was completely immersed in 0.1 M solution of Na_2SO_4 (Fig. 4.13) to enable monitoring eventual corrosion development and – first of all – to increase number of the recorded higher harmonics due to a lower resonant frequency of the vibrating tip submerged in liquid. During the experiment, the specimen was scanned (21 μm x 21 μm area) in the tapping mode in the mentioned solution without external polarization. The cantilever, type NSG01 (Fig. 3.3), was excited by a harmonic 10 V voltage signal. The cantilever's resonance frequency was equal to $f_0 = 74.9$ kHz (when submerged in the applied electrolyte).

The images with the resolution of 256 x 256 pixels and with the scanning period equal to 1 s for each row were recorded. The applied acquisition board assured 4800 samples per each pixel. For the established cantilever resonance frequency f_0, about 300 periods of the sinusoidal excitation signal were acquired to characterize each pixel separately. That was enough to assure necessary averaging during the lock-in amplifier processing, and to generate the images with a limited additive noise component, at least up to the 8th harmonic. During scanning, the dedicated NOVA software created two images: topography (Fig. 4.14a) and DFL (control error; Fig. 4.14b). The images were recorded in laboratory at the room temperature.

In Fig. 4.15, the images generated by four selected higher harmonics after necessary pre-processing are presented. The image of the first harmonic (Fig. 4.15a) is used to verify the proposed processing method because one should obtain almost the same picture as the feedback image from the NOVA software. The presented topography exposes the product of temperature sensitization (the bulge at the left bottom corner of the pictures).

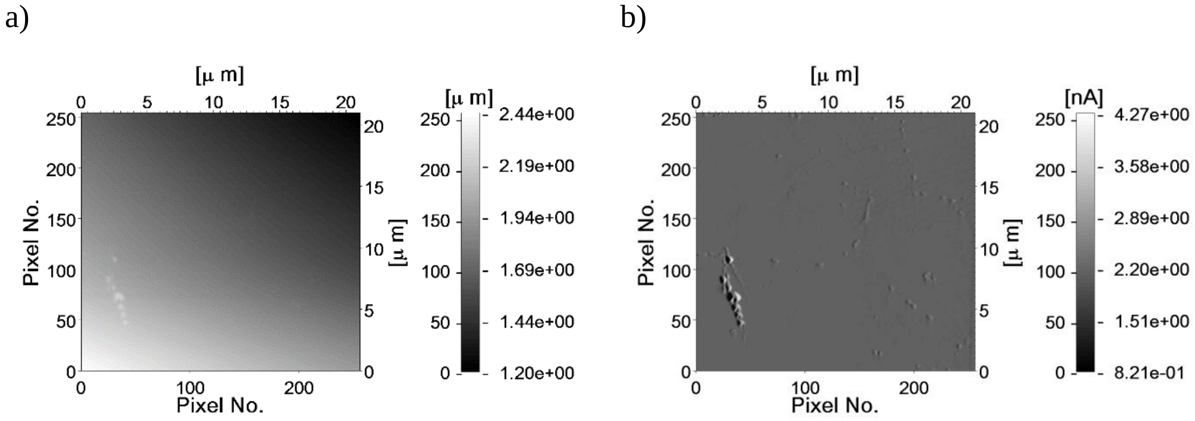

Fig. 4.14 The images of AISI304 steel specimen, generated by the NOVA software: a) topography, b) DFL

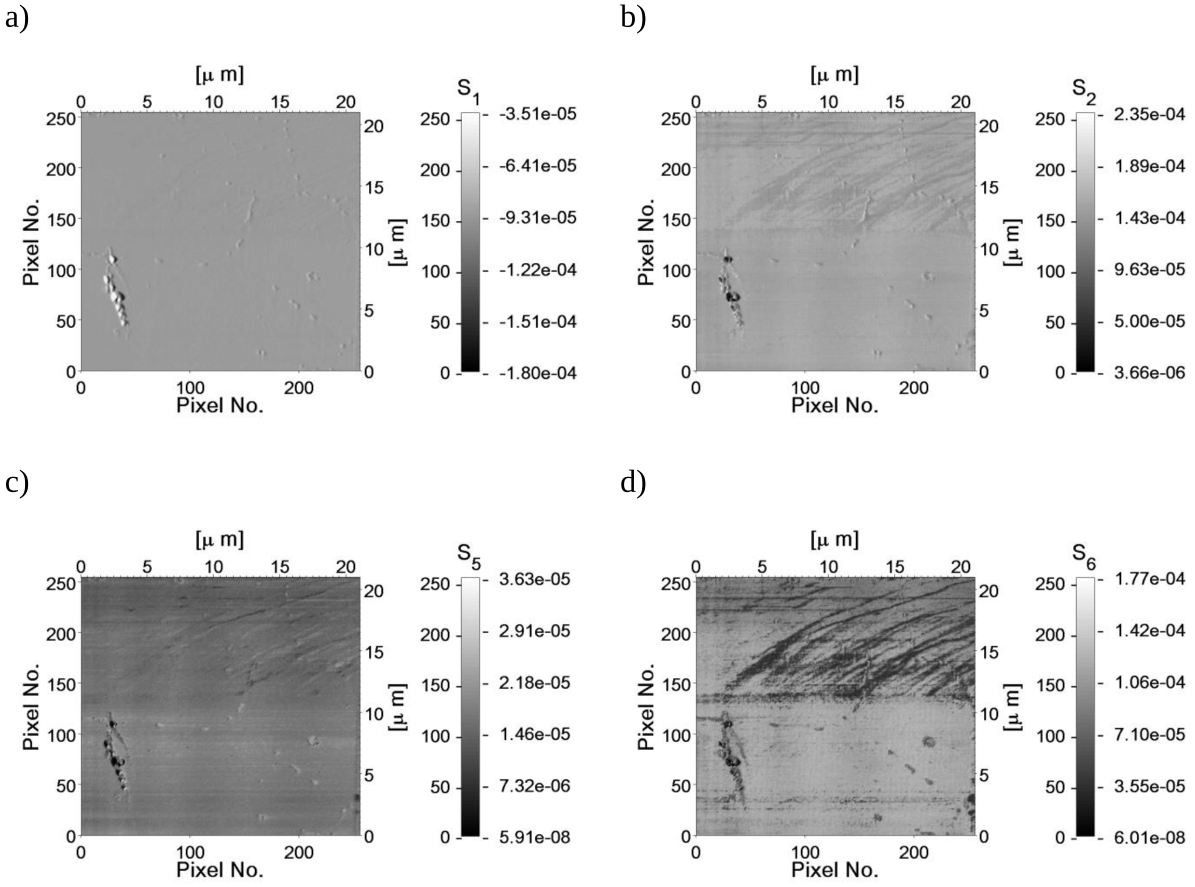

Fig. 4.15 The higher-harmonic images of the AISI304 steel specimen: a) 1st, b) 2nd, c) 5th, d) 6th harmonic image

Differences between Fig. 4.14b and Fig. 4.15a are hardly noticeable and limited only to some variations in the shade of the background grey. It proves that the measurements were made correctly. In the presented images (Fig. 4.15), intensities of the estimated consecutive higher harmonics were marked as S_n, where n is equal to their number. Fig. 4.15b, c and d show, respectively, the second (S_2), the fifth (S_5) and the sixth (S_6) harmonic images. Some of them expose details, which are not clearly visible in other images.

The images of the 2nd (Fig. 4.15b), the 5th (Fig. 4.15c) or the 6th (Fig. 4.15d) harmonics reveal effects of some unavoidable local differences in steel treatment during the polishing procedure (the streaks in the right top corner). These local differences are most visible in the image of the sixth harmonic. Thus, it can be concluded that this harmonic exposes in a better way the selected details of the examined surface. Moreover, the results confirm that the higher-harmonic imaging in liquid can be efficiently used, as in the case of measurements when the tip vibrates in air only.

The measurements in the aqueous environment (Fig. 4.14, Fig. 4.15) were continued when corrosion processes developed in time. Corrosion was accelerated by additional polarization, which induced aggressiveness of the applied electrolyte. Because of the cantilever resonance frequency $f_0 = 74$ kHz and the applied USB-6356 having the maximum sampling frequency 1.2 MSa/s, about 74 000 periods and over 4 680 samples of the sinusoidal excitation signal were recorded to characterize each pixel. The measurement scheme included a continuous increase of polarizing voltage to accelerate corrosion processes, as presented in Fig. 4.16.

The 256 x 256 pixels topography image (Fig. 4.17a) of 15 μm x 15 μm specimen does not present topographical details satisfactorily. After additional processing, called "flatten correction" (see Appendix C), more details are revealed (Fig. 4.17b). Despite a clearly visible periodic pattern, the first harmonic image (Fig. 4.17d) is similar to the DFL (control error) image (Fig. 4.17c). The higher-harmonic images of the first harmonic recorded at selected moments (Fig. 4.16) are presented in Fig. 4.18.

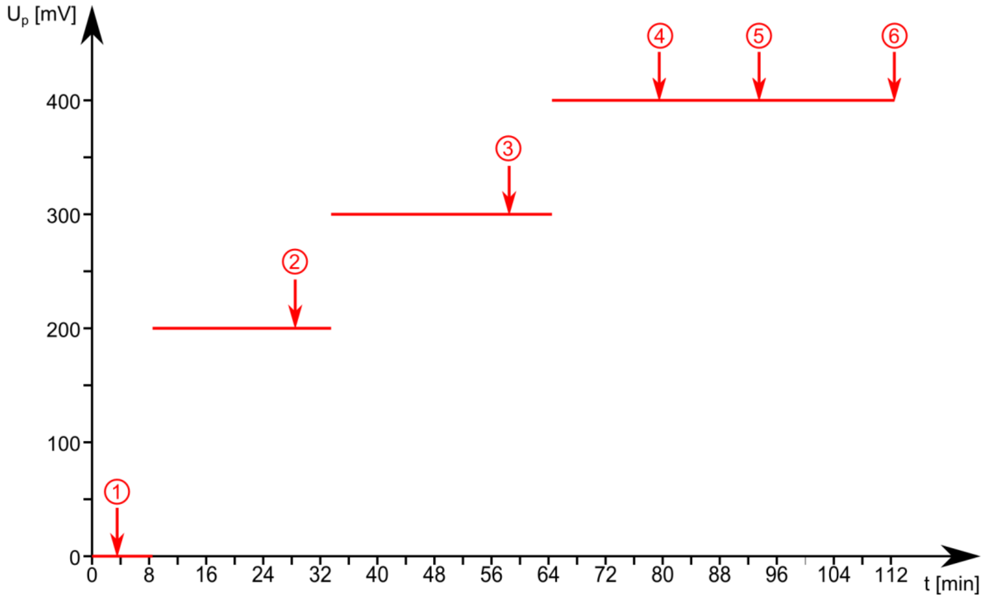

Fig. 4.16 The measurement scheme of the applied anode polarizing voltage U_p versus time; the measurement points: 1, 2, 3, 4, 5, 6 mark the moments of recording the AFM images; the polarizing voltage was switched off during specimen scanning

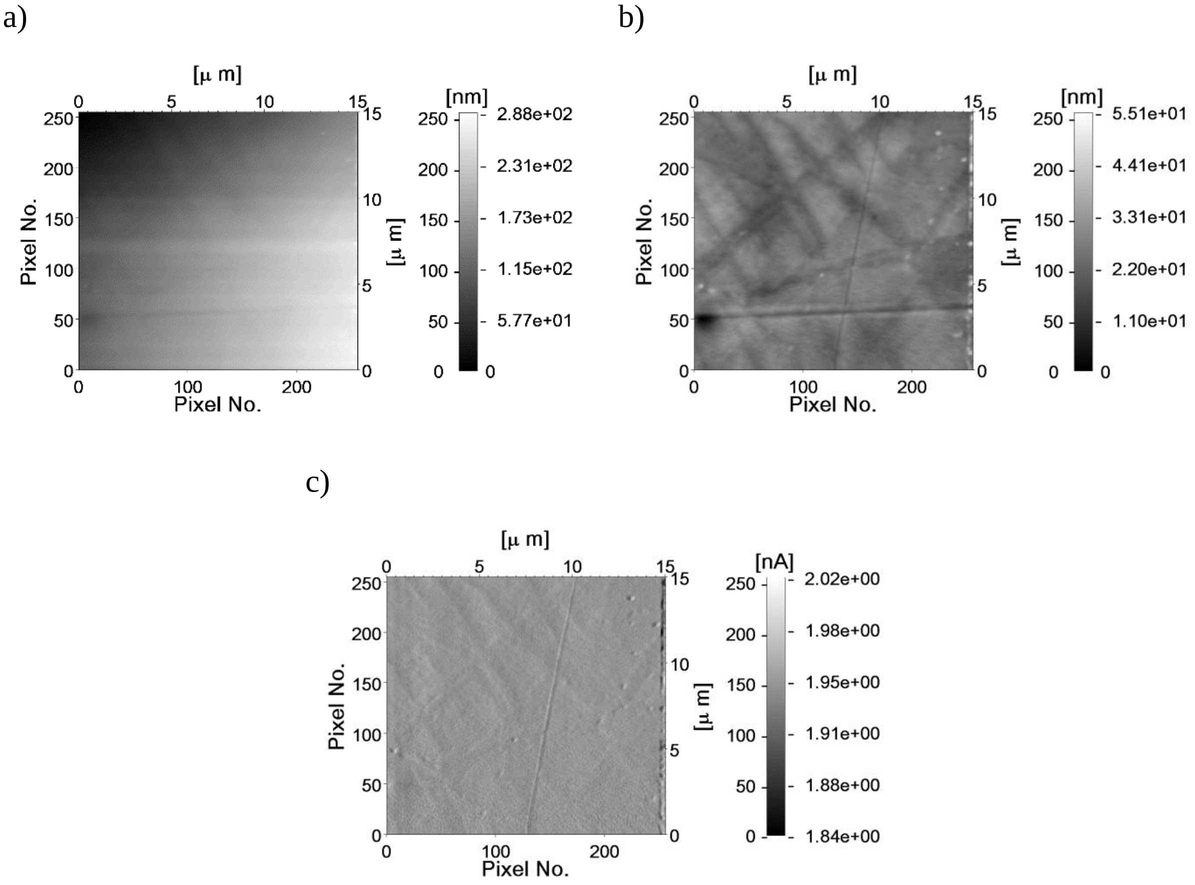

Fig. 4.17 The images generated by the NOVA software for the AISI304 steel specimen: a) topography, b) flatten corrected topography using the 2nd order subtraction, c) DFL (control error)

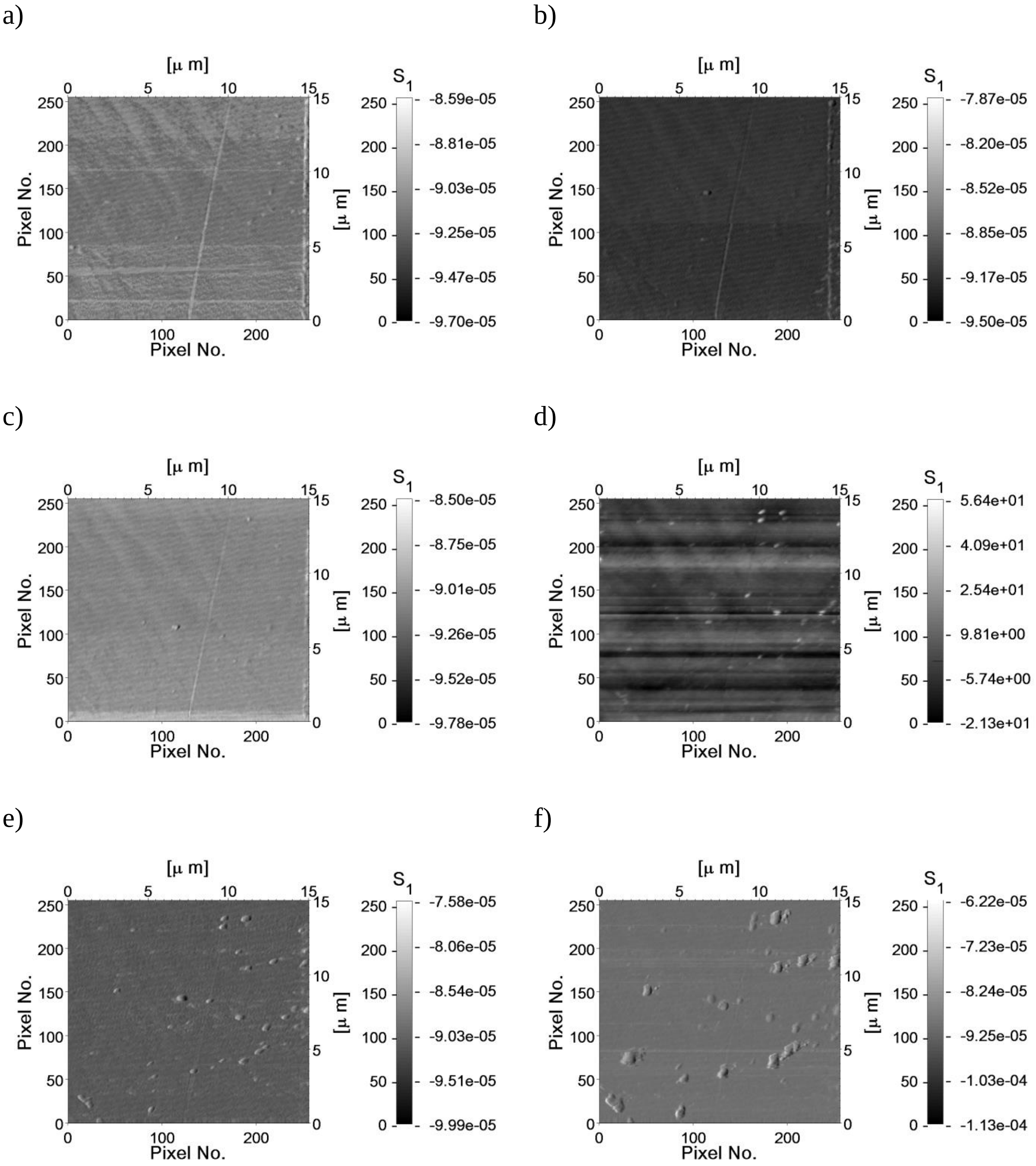

Fig. 4.18 The 1st harmonic image recorded at selected moments (Fig. 4.16): a) point 1 (3 min.), b) point 2 (29 min.), c) point 3 (59 min.), d) point 4 (79 min.), e) point 5 (93 min.), f) point 6 (113 min.)

The 1st harmonic image (Fig. 4.18a) presents the data recorded before polarization of the examined specimen. Next, the corrosion process was accelerated by applying 200 mV anode polarization. The following picture (Fig. 4.18b) was obtained at the 29th minute of the experiment, after 19 minutes of stable polarization. An effect of corrosion process development is clearly visible in the central part of the image. From the 34th minute (step 3) the specimen was polarized by the 300 mV anode voltage. After 25 minutes the next image was recorded (Fig. 4.18c). In addition to the previously observed growths of objects in the central part, there is an increase in the spot growths around the pixel {230, 195}. After next 6 minutes the applied anode polarization voltage was increased to 400 mV. The following picture (Fig. 4.18d) was recorded after next 15 minutes and showed significant development of corrosion products. The 5th image (Fig. 4.18e) was achieved after next 24 minutes. The number of corroding centres increased even more. The last image (Fig. 4.18f), obtained after next 19 minutes, presents even greater number of large corroding centres.

The applied polarization caused not only degradation of the examined surface, but also caused damage to the scanning tip and disturbed the measured oscillations by introducing an additional voltage between the surface and the scanning tip. So, the polarity was switched off during the scanning phase of the experiment, to stabilize measurement conditions. This was necessary because:

1. there would be an unacceptable difference in time of exposure to various corrosion agents during data acquisition for the first and the last pixels of the image,
2. the applied polarization voltage could cause disturbances in the tip-sample interaction, so that we would not be able to clearly observe corrosion effects that could arise in the higher-harmonic image due to an extra current load,
3. the scanning tip could be destroyed by the corrosion processes.

In the next measurements 256 x 256 pixels images of the 25 μm x 25 μm austenitic steel area were gathered during scanning with the cantilever resonance frequency f_0 = 206 kHz. The maximum value of 50 MSa/s sampling frequency, using the PXI data acquisition board, assured over 206 000 periods and more than 195.3 kSa of the excitation harmonic signal to characterize each pixel. The measurement scheme is presented in Fig. 4.19.

The topography image (Fig. 4.20a) of the scanned specimen (25 μm x 25 μm) does not satisfactorily present topographical details. This is due to an effect of a slowly rising optical signal recorded during the scanning process. Only after applying a so called “flatten correction” processing, available in the NOVA software (the details are presented in Appendix C), much better results are obtained (Fig. 4.20b).

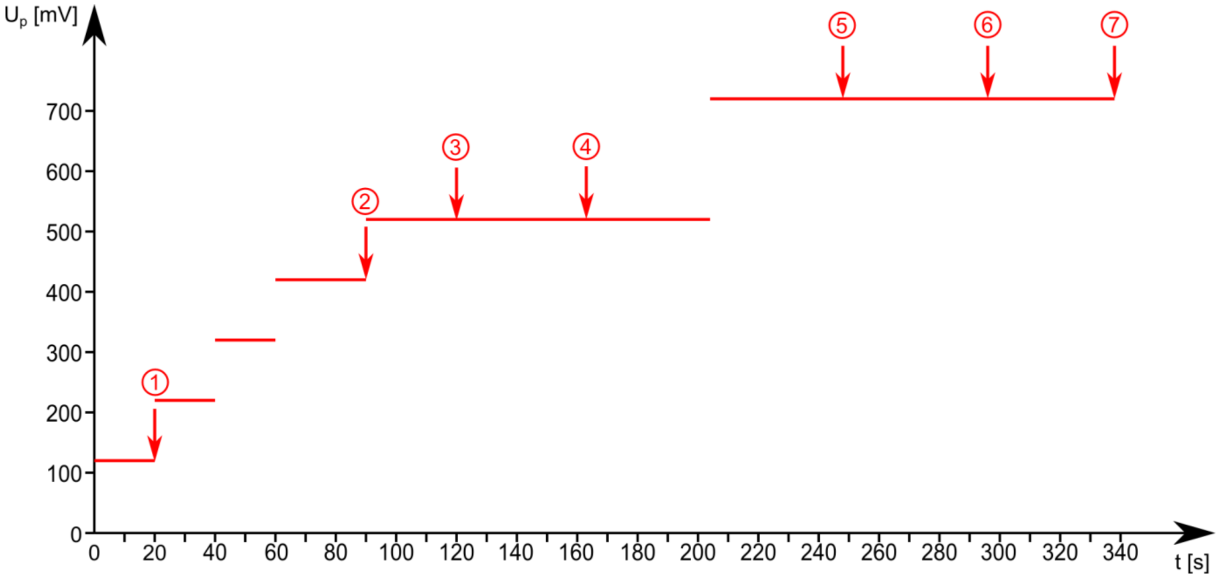

Fig. 4.19 The measurement scheme of the applied anode polarizing voltage U_p versus time; the measurement points 1, 2, 3, 4, 5, 6, 7 mark the moments of recording the AFM images; the polarizing voltage was switched off during specimen scanning

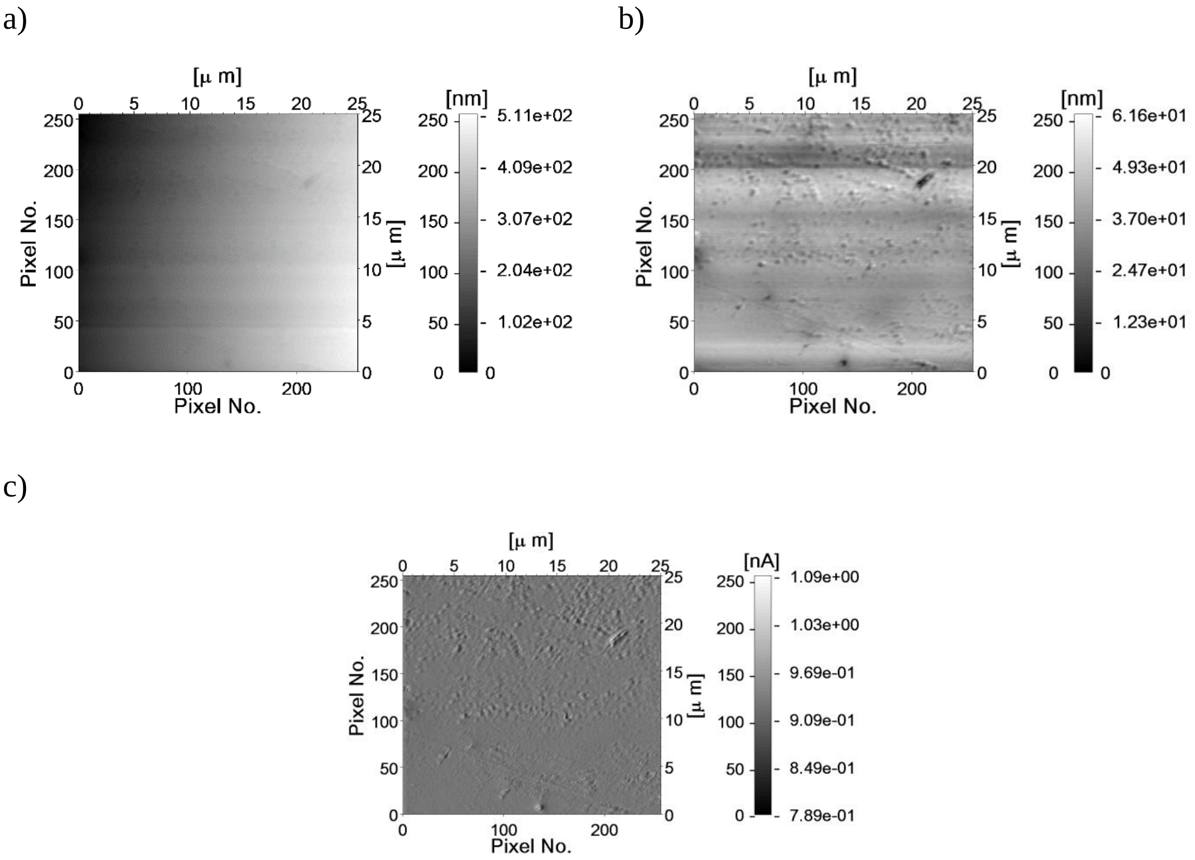

Fig. 4.20 The surface of the AISI304 steel specimen generated by the NOVA software: a) topography, b) flatten corrected topography using the 3rd order subtraction, c) DFL (control error)

The experimental studies, performed according to the measurement scheme (Fig. 4.19), resulted in obtaining a numerous set of pictures. This chapter considers only selected images representing the most valuable results and showing possible applications of higher harmonics in corrosion processes monitoring.

The first sequence (Fig. 4.19, step 1) of the considered images were recorded after supplying the anode polarity of approx. 120 mV for 20 seconds. All the recorded images for that measurement phase are presented in Appendix B (Fig. B.1). The lower parts of the pictures show signs of scratches left by the grinding process. There are also visible inclusions which may be corrosion products or other compounds resulting from the process of thermal sensitization (especially in the upper parts of these pictures). This interpretation was established by considering experimental data obtained in similar laboratory experiments using the AFM or considering corrosion processes only [120, 121]. The cavities, that could be associated with pitting corrosion processes, were observed. It is worth to mention that the image of the 2nd harmonic (Fig. 4.21a) has visible cavities at its lower part, whereas the image generated by the 7th harmonic (Fig. 4.21b) does not include such details, caused by the grinding process.

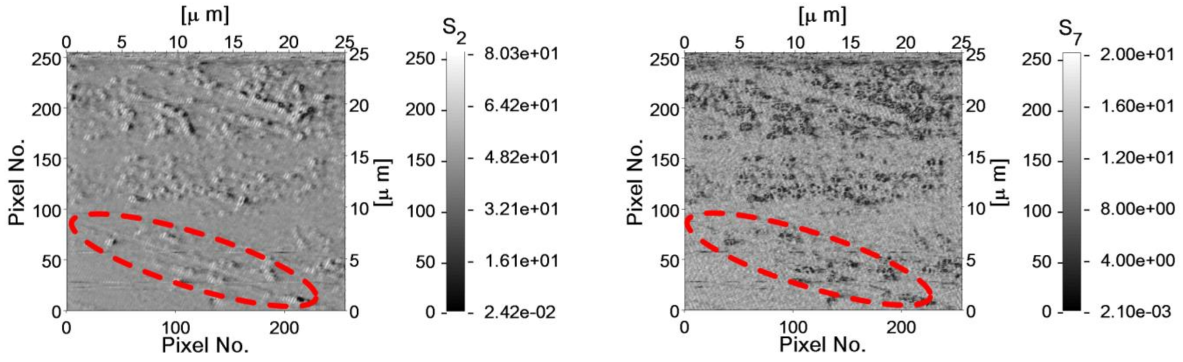
a)

b)

Fig. 4.21 The higher-harmonic images of the AISI304 specimen surface in the first experiment phase (Fig. 4.19): a) the 2nd harmonic image, b) the 7th harmonic image

The next measurements (Fig. 4.19, step 2) were performed after applying the sequence of anode polarization voltages: 220 mV for 20 seconds, 320 mV for the next 20 seconds, and 420 mV for the last 30 seconds. The applied polarization conditions resulted in growing the oxide layer coating of the specimen surface. The height of the specimen has slightly increased. It is worth to notice that after the applied polarization voltages some objects have changed their size, for example the object at coordinates {21 μm, 19 μm}. It proves that the electrochemical processes resulted in developing corrosion products. The same effect of different sensitivity to different objects for various higher-harmonic images was observed as in the previous measurement phase (Fig. 4.19, step 1). The image generated for the second harmonic has still visible cavities (Fig. 4.22a), as reported in the previous stage (Fig. 4.21a), whereas the higher-harmonic images do not show such objects (e.g. the 4th harmonic image – Fig. 4.22b).

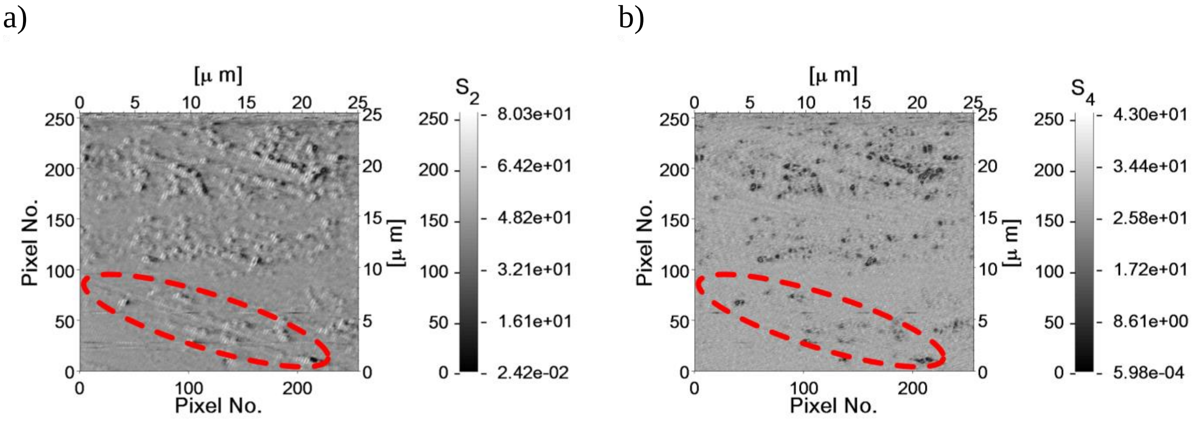

Fig. 4.22 The higher-harmonic images of the AISI304 specimen surface in the second experiment phase (Fig. 4.19): a) the 2nd harmonic image, b) the 4th harmonic image

The next observations (Fig. 4.19, step 3), were performed after applying anode polarization of 520 mV for 30 seconds. The results exhibit two new and opposite phenomena. The size of the previously mentioned pit at coordinates {21 μm, 19 μm} was slightly reduced (Fig. 4.23). At the same time the relative height of the inclusions has decreased. These effects can be explained by progressive development of the oxide layer on the surface of steel electrode. On the other hand, advancement of pitting in the lower part of image {14 μm , 1 μm} is observed (Fig. 4.23). Moreover, the previously described difference (Fig. 4.22) between the 2nd harmonic image and the 4th or 7th harmonic images was still observed (Fig. 4.24).

The next measurements (Fig. 4.19, step 4) were performed after applying the anode polarization of 520 mV for 43 seconds. Further alignment of the surface was observed. This is consistent with the hypothesis of an increase of the oxide layer induced by the anodic polarization. The higher-harmonic images revealed further increase of the pits at coordinates {21 μm, 19 μm} and {14 μm, 1 μm} (Fig. 4.25). The difference between the 2nd harmonic image and the 4th or 7th harmonic images was again observed (Fig. 4.26).

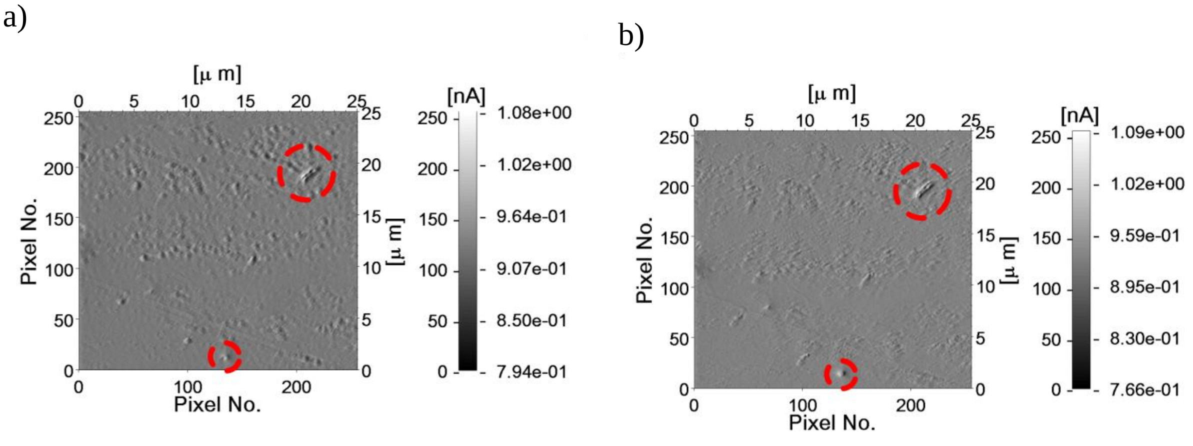

Fig. 4.23 The DFL (control error) images of the AISI304 specimen surface: a) in the second experiment phase (Fig. 4.19), b) in the third experiment phase (Fig. 4.19)

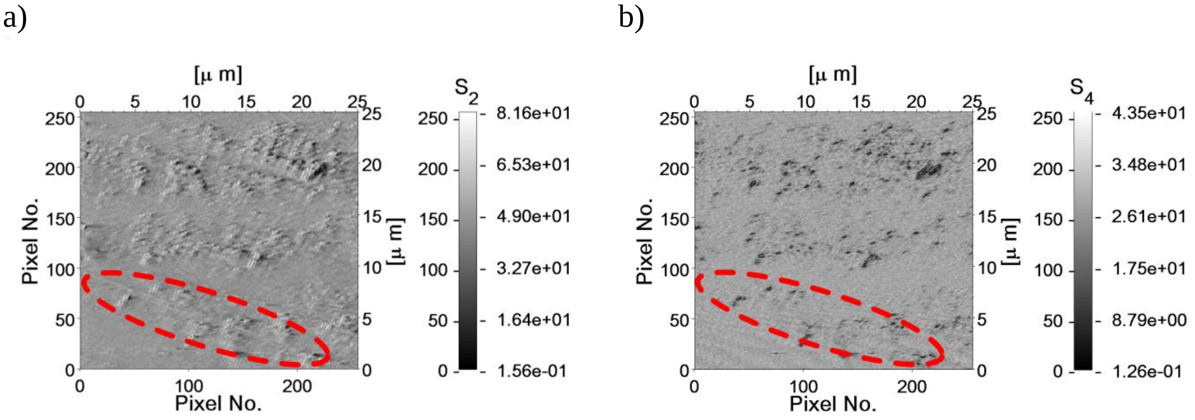

Fig. 4.24 The higher-harmonic images of the AISI304 specimen surface in the third experiment phase (Fig. 4.19): a) the 2nd harmonic image, b) the 4th harmonic image

The next measurements (Fig. 4.19, step 5), were performed after applying the sequence of anode polarization voltages: 520 mV for 43 seconds and 720 mV for the last 43 seconds. The results exhibit a specific behaviour of the 4th harmonic image, exposing scratches made during the polishing procedure (Fig. 4.27a). The image of the 7th harmonic (Fig. 4.27b) reveals also these scratches but their exposition is weaker than in the previous case of the 4th component.

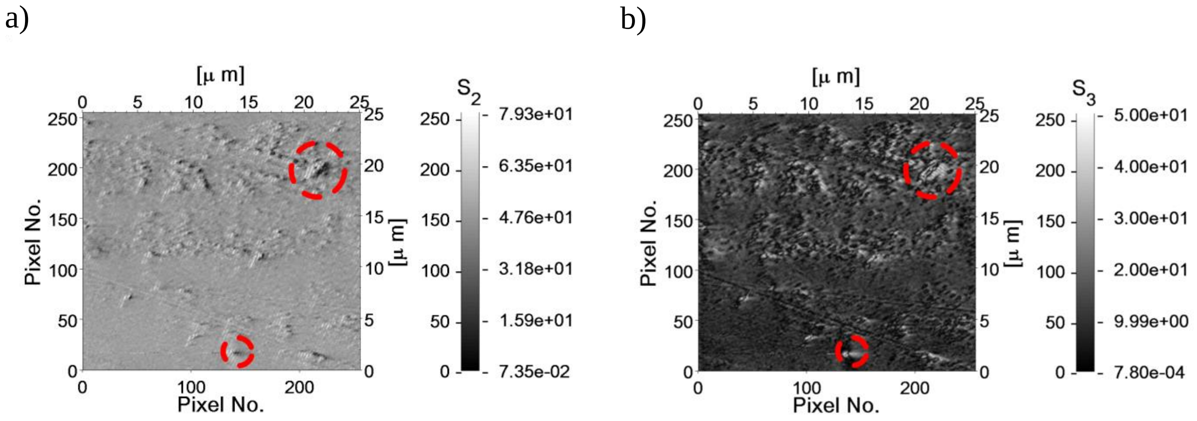

Fig. 4.25 The higher-harmonic images of the AISI304 specimen surface in the fourth experiment phase (Fig. 4.19): a) the 2nd harmonic image, b) the 3rd harmonic image

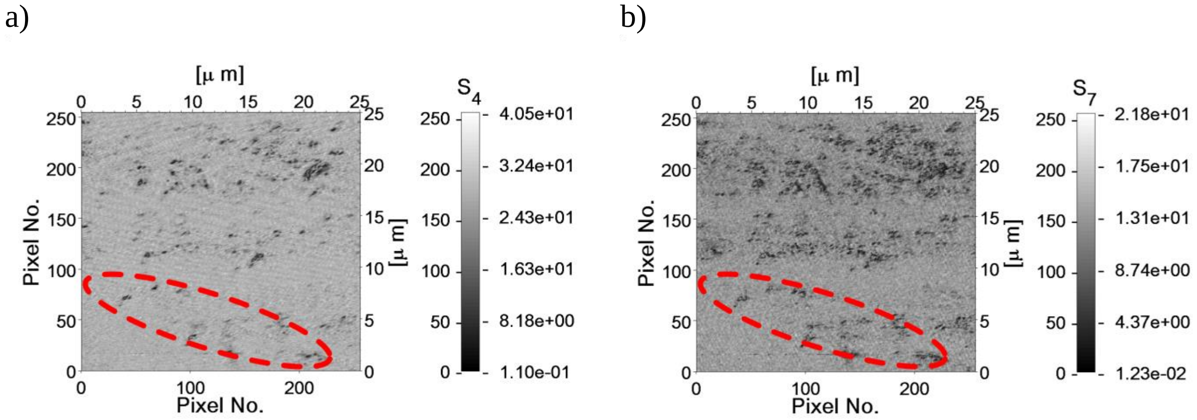

Fig. 4.26 The higher-harmonic images of the AISI304 specimen surface in the fourth experiment phase (Fig. 4.19): a) the 4th harmonic image, b) the 7th harmonic image

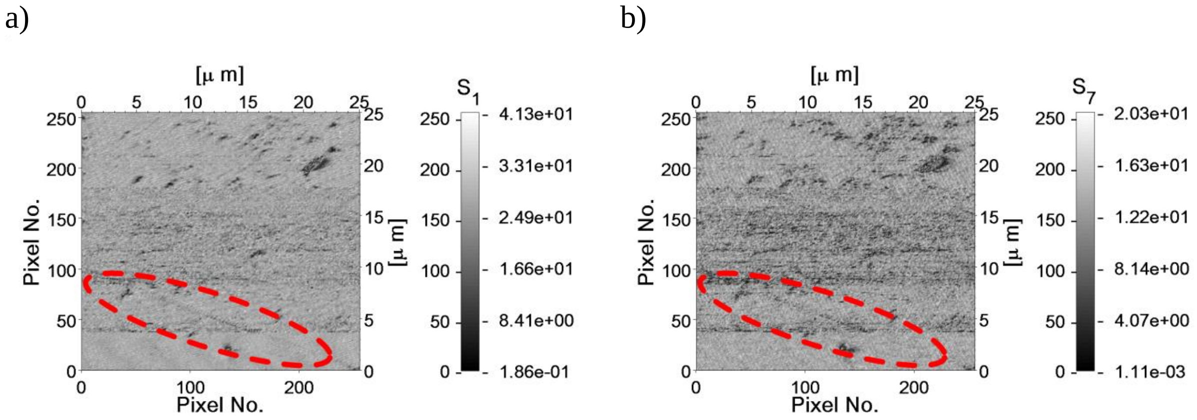

Fig. 4.27 The higher-harmonic images of the AISI304 specimen surface in the fifth experiment phase (Fig. 4.19): a) the 1st harmonic image, b) the 7th harmonic image

The next phase of corrosion development (Fig. 4.19, step 6) was observed after applying the anode polarization of 720 mV for 44 seconds. Further pit development at coordinates {21 μm, 19 μm} was observed. The pit increased so much, that its shape had changed. We can conclude that the generated images are quite selective for the mentioned pits (e.g. the images of the 2nd and the 3rd harmonics – Fig. 4.28). Moreover, the cavities resulting from the surface treatment are visible in the 4th harmonic image.

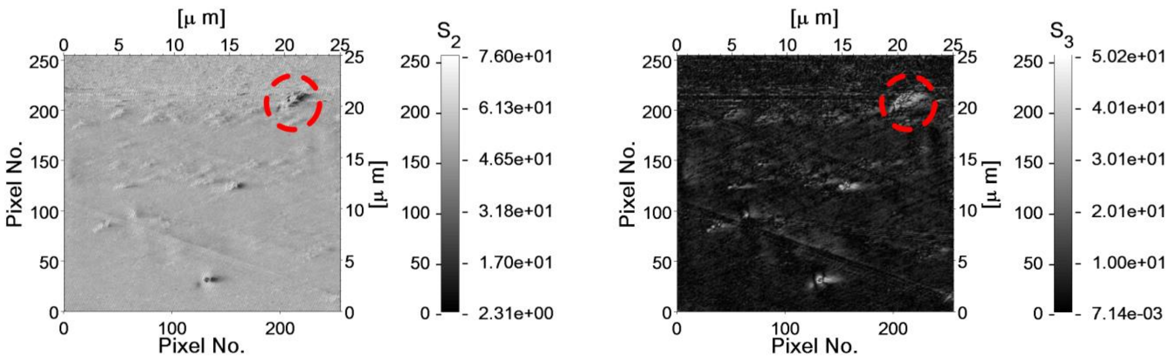
a)

b)

Fig. 4.28 The higher-harmonic images of the AISI304 specimen surface in the fifth experiment phase (Fig. 4.19): a) the 2nd harmonic image, b) the 3rd harmonic image

The final phase of data recording (Fig. 4.19, step 7) was performed after applying the anode polarization of 720 mV for 45 seconds. The growth of oxidation layer around the whole examined area was observed again. The cavities resulting from the surface treatment are still visible in the 4th harmonic image, as was noticed in the previous measurement phase. The greatest difference between the images generated by higher harmonics was observed for the developed pit at coordinates {21 μm, 19 μm} (Fig. 4.29). We observe that the object is much blurred at higher harmonics (e.g. the 7th harmonic – Fig. 4.29b). It can be concluded that the corrosion products cover the pit and further development of corrosion processes should occur there.

In each measurement series the higher-harmonic images have a better contrast than the images generated by the NOVA software. The experimental results proved that higher-harmonic images can characterize the topography objects very selectively. The 4th and the 7th harmonics are more sensitive to extreme (high or low) topographic substructures. That can explain invisibility of the polishing scratches in the 4th harmonic images.

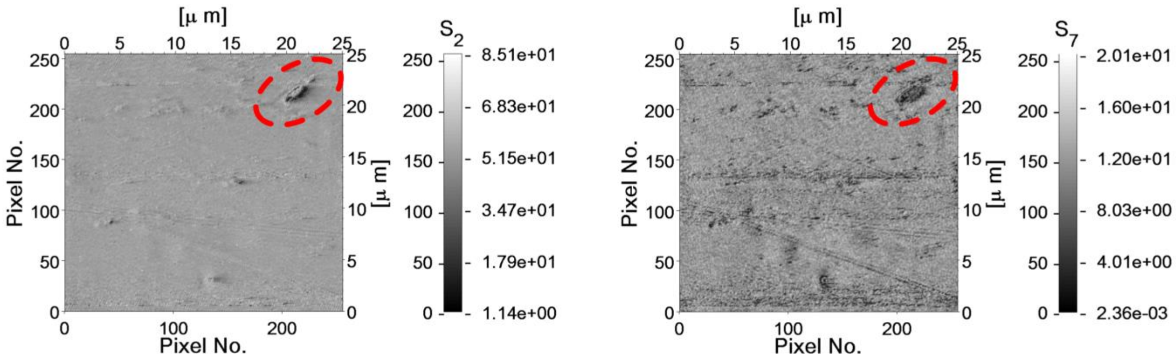
a) b)

Fig. 4.29 The AISI304 specimen with marked different fragments of the higher-harmonic images in the seventh measurement point: a) the 2nd harmonic image, b) the 7th harmonic image

The results of the experiment proved usefulness of the higher-harmonic imaging for increasing capabilities of the AFM, especially during corrosion process monitoring, by revealing more subtle differences between corrosion products (the first assertion of the dissertation). The higher-harmonic imaging during corrosion process development may be advantageous in assessing quality of metal materials or the corrosion protection methods. Fast and effective evaluation of production technology of metal parts should greatly reduce the operating cost of metal constructions.

4.4 Interferences observed in the higher harmonic imaging

In each scanning process, the 1st harmonic image can be used to determine correctness of the measurement. If the 1st harmonic image is not properly recorded, the consecutive higher-harmonic images will not be satisfactory, too. It means that the experimental work can be reduced by stopping continuation of such an experiment. This procedure was assumed during numerous experiments because the applied measurement setup was able to estimate only up to three higher-harmonic images in real time scanning of the specimen.

The main problem of higher-harmonic imaging is to secure optimal conditions and parameters of the AFM measurements [122]. Individual parameters of each surface and scanning tip are difficult to be known before the experiment. Thus, many measurements may fail even if the 1st harmonic image is quite satisfactory. Such effects can be observed for a specimen of AISI304 steel (Fig. 4.30, Fig. 4.31).

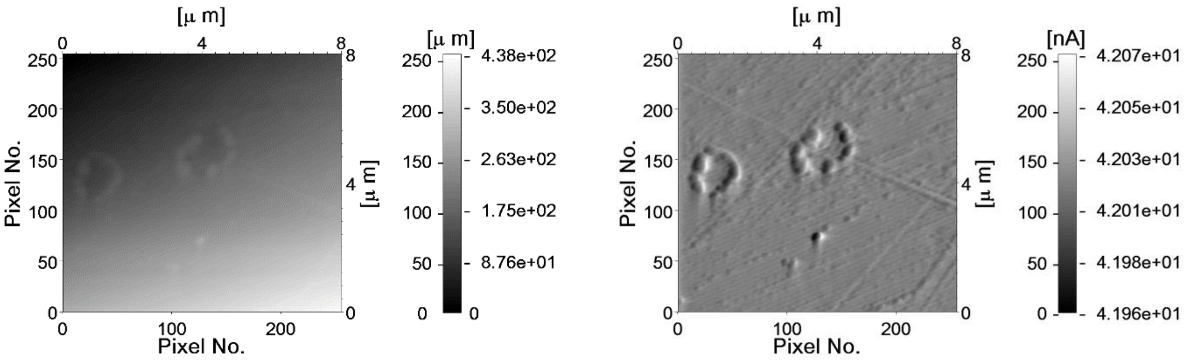
a) b)

Fig. 4.30 The images of a specimen of AISI304 steel recorded by the NOVA software when the tip vibrated in air: a) topography, b) DFL (control error)

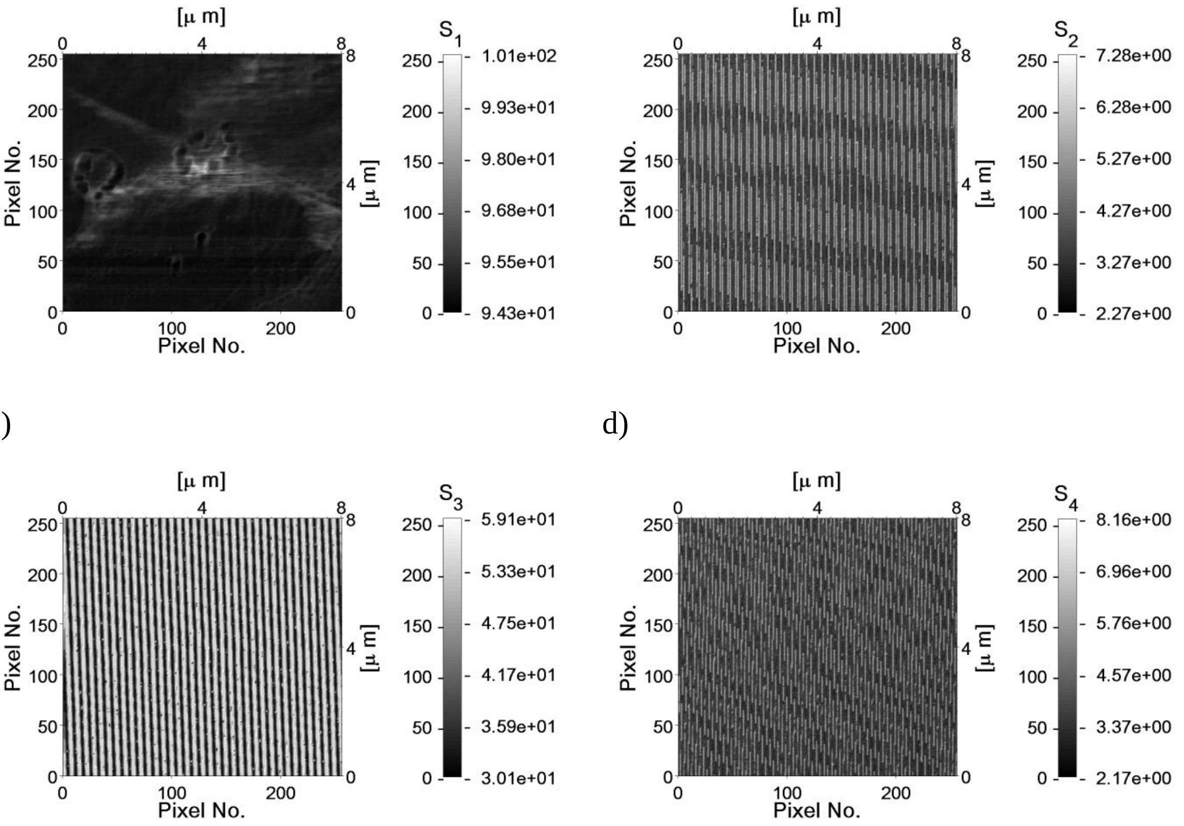
a) b) c) d)

Fig. 4.31 The higher-harmonic images of a specimen of AISI304 steel, when the tip vibrated in air: a) 1st, b) 2nd, c) 3rd, d) 4th harmonic image

It was also observed that even if the 1st harmonic image is of good quality the rest does not introduce any additional information. That case was observed for a specimen of vapour deposition diamond (Fig. 4.32, Fig. 4.33). The results can be explained by high hardness, roughness and surface uniformity. Such non-linear effects were similar within the entire area of the examined specimen.

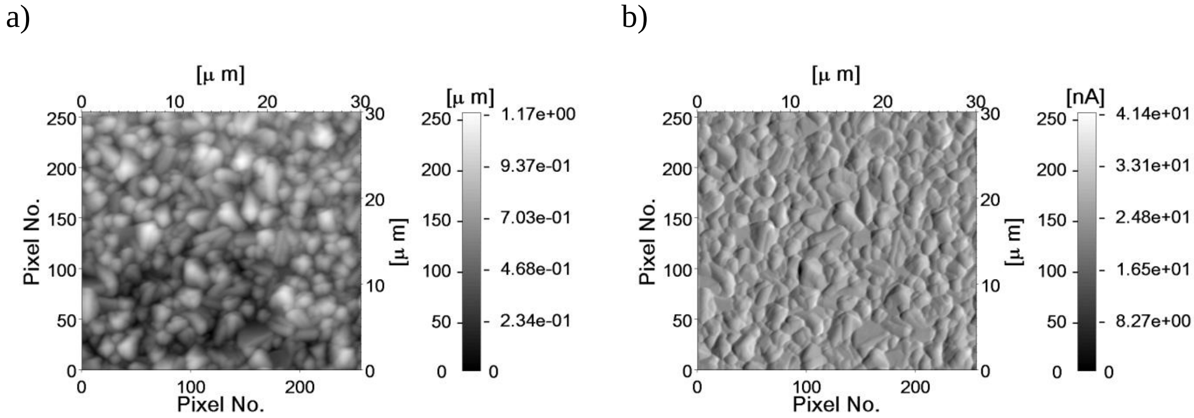

Fig. 4.32 The NOVA software images of a vapour deposition diamond specimen: a) topography, b) DFL (control error)

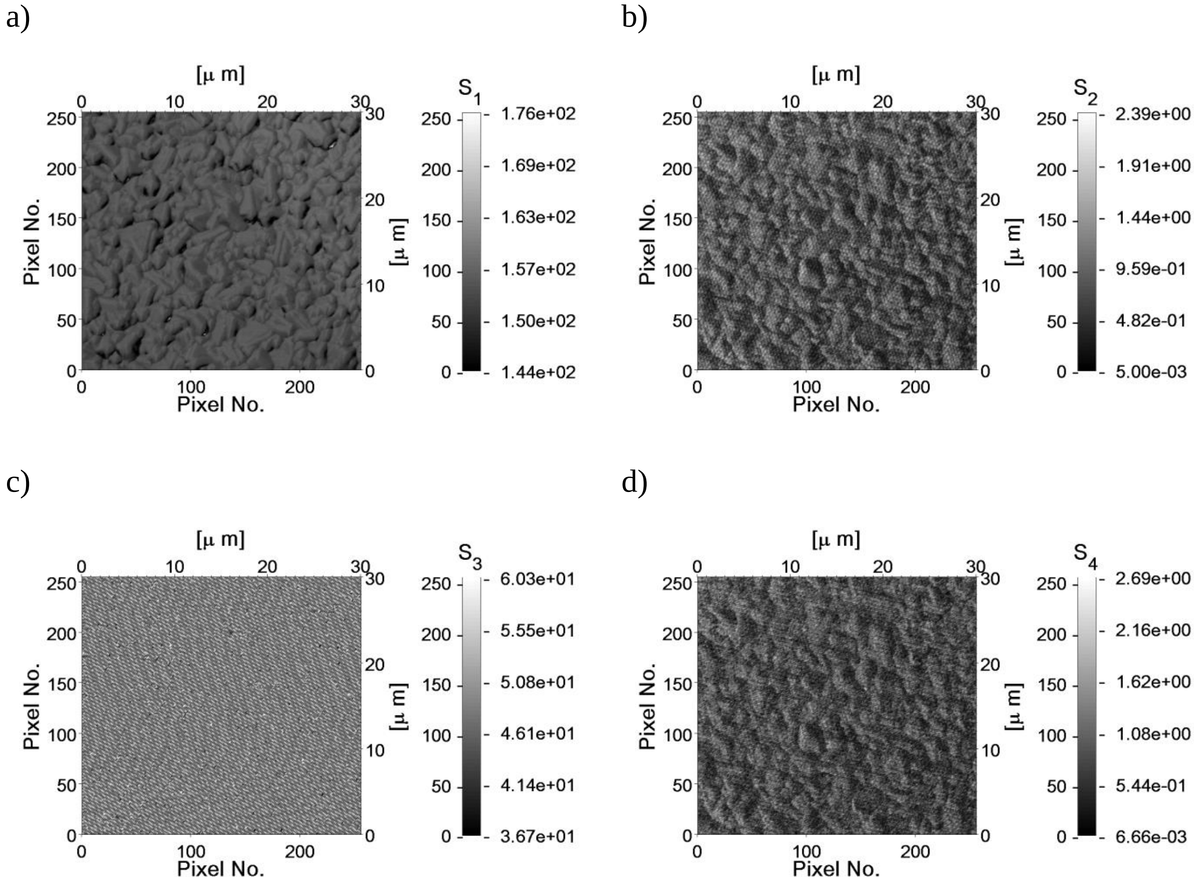

Fig. 4.33 The higher-harmonic images of a vapour deposition diamond specimen: a) 1st, b) 2nd, c) 3rd, d) 4th harmonic image

Among important problems of the higher-harmonic imaging is the most popular type of the observed interferences – harmonics induced by an external electromagnetic field. These harmonics are exposed for specimens where the non-linear effects are weak. So, in such cases applying the higher-harmonic analysis is rather doubtful.

5 An algorithm automatically increasing quality and contents of images

It is difficult to unambiguously determine quality of an analysed image. Human beings differently perceive various details of an image because of the applied colour palette or gradation of shades. Therefore, information contained in the analysed higher-harmonic images has to be processed to be identified explicitly. To expose the problem, an arbitrarily selected 200th row (Fig. 5.1a) and 30th column (Fig. 5.1b) from the 1st (solid line) and the 5th (dashed line) harmonic images presented in Fig. 4.15 were compared. The selected row and column include an object identified as the product of sensitization (column No. $j = 30$) and some of its variations during polishing (row No. $i = 200$). The selected row is plotted above, whereas the column on the left of each image (Fig. 5.2). Looking only at both curves (Fig. 5.1b) we can see a difference, but it is difficult to determine which one of them is more informative.

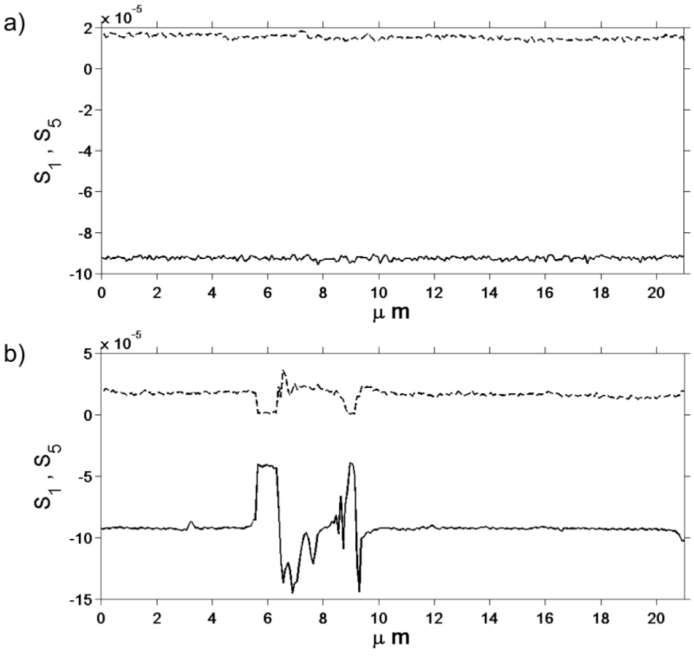

Fig. 5.1 An illustration of changes between the higher-harmonic image intensities of selected objects: a) the 200th row pixel values of the 1st (solid line) and the 5th (dashed line) harmonic images, b) the 30th column pixel values of the 1st (solid line) and the 5th (dashed line) harmonic images

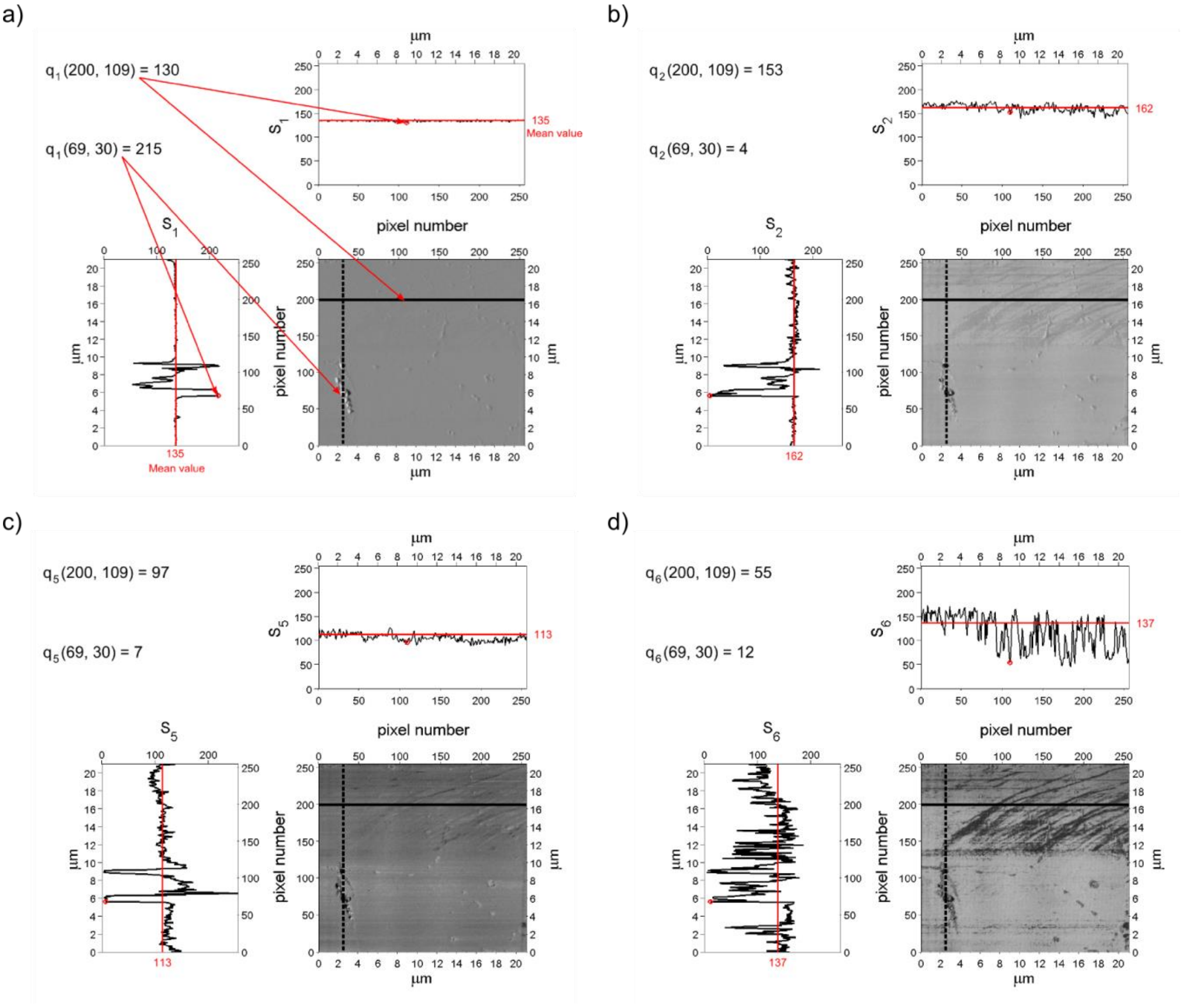

Fig. 5.2 The higher-harmonic images of the AISI304 specimen with the marked i = 200th row (solid line), j = 30th column (dashed line) and the mean value of the image for: a) the 1st harmonic, b) the 2nd harmonic, c) the 5th harmonic, d) the 6th harmonic

Analysis of the relative difference $\Delta_n(i, j)$ between the mean pixel intensity $\mu_{\Delta n}$ for the nth harmonic image and the selected pixel intensity $q_n(i, j)$ in the ith row and the jth column, proves that some of the topographic substructures are more visible in the higher-harmonic images (Tab. 1). Let us consider two arbitrarily selected points, representing an abrupt change in the specimen topography (i = 200, j = 109) due to the temperature sensitization, and less intense streaks (i = 69, j = 30) due to the polishing procedure. With increasing the harmonic number, the relative difference $\Delta_n(200, 109)$ of the considered point raises significantly. Simultaneously, the relative difference $\Delta_n(69, 30)$ preserves its high value in all higher-harmonic images. These results prove that non-linear effects represented by the higher-harmonic images reveal both considered structure details. The streaks at the point (i = 200, j = 109) start to be more exposed at higher harmonics. The object at the point (i = 69, j = 30) was displayed with similar visibility, starting from the second harmonic.

Tab. 5.1 The comparison of the relative differences $\Delta_n(i, j)$ from the mean pixel intensity $\mu_{\Delta n}$ of the considered n^{th} image for two selected points: $q_n(200, 109)$ and $q_n(69, 30)$; the 1st, the 2nd, the 5th and the 6th harmonic images were analysed (n = 1, 2, 5, 6) as presented in Fig. 5.2

Parameter	**Higher-harmonic image**			
	$n = 1$	$n = 2$	$n = 5$	$n = 6$
$\mu_{\Delta n}$	135	162	113	137
$q_n(200, 109)$	130	153	97	55
$q_n(69, 30)$	215	4	7	12
$\Delta_n(200, 109)$ [%]	3.7	5.5	14.2	59.9
$\Delta_n(69, 30)$ [%]	59.2	97.5	93.8	91.2

The presented experimental results confirm that the intensity of higher harmonics of the vibration tip reveals additional information about the objects located on the examined specimen. It should be underlined that it is very difficult to determine which of the harmonics is more informative. Additionally, various objects can be exposed in a different way in consecutive images. Therefore, a method of automatic selecting the relevant parts of the analysed specimen images to improve the resulting quality should be proposed. That procedure would be very helpful when numerous experiments are conducted and automation would speed up recognition of the most interesting objects.

Such an algorithm has to consider the effects caused by the offset variation between the images and effects caused by their transformation into the scale of greyness, typically within the range 0÷255, where 0 is black and 255 is white [123]. It means that all values between 0 and 255 are plotted as shades of grey. In this way, the offset determines brightness of the image background. Moreover, through binarisation of greyness scale images, the useful information may be lost [124]. That remark is crucial for an ability of detecting some details in the objects, represented by values close to the extreme available numbers (maximum or minimum). This effect can be reduced by introducing a non-linear scale between the recorded data and the applied greyness scale. Unfortunately, that procedure requires the operator's activity to select the kind of non-linear scale that would only expose the most important details and improve the contrast – without revealing additional information about stiffness, as expected in the higher-harmonic images.

There is no clear method for determining quality of a surface image. Every assessment is based on personal needs of the users or on comparing with the reference image. The first method requires interpretation of the image and a feedback from the human evaluator. An image enhancement is the task of applying certain transformations to the image, so as to obtain a visually more pleasant and more detailed result [125]. The second method cannot be used due to lack of a reference image. Thus, a procedure as in the first mentioned method but based on some objective parameters, estimated from the analysed pictures by a mathematical procedure, should be proposed. The parameters, which would describe informativeness of the analysed image and a possibility of its automatic estimation, are the entropy *H* and the signal-to-noise ratio *SNR*. The entropy can be viewed as the amount of information provided by the image. Thus, it is merely a statistical average of uncertainty or information in the analysed data [126]. On the other hand, the uncertainty can be caused not only by the details in the specimen's image but also by the additive noise present during data recording. So, to evaluate the image quality, the *SNR* should be also considered. These parameters, or their combination, could be applied to select the most relevant pictures for exposing the examined specimen details.

The Shannon entropy is a measure of the uncertainty associated with a random variable [127]. Specifically, the Shannon entropy quantifies the expected value of the information contained in a message. The Shannon entropy $H(X)$ of a random variable X having the values from the set $(x_0, x_1, \ldots, x_k, \ldots, x_u)$ is defined as:

$$H(X) = -\sum_{x_k = x_0}^{x_u} p_{s_k} \log p_{s_k} \ , \tag{5.24}$$

where p_{x_k} denotes the probability of $X = x_k$:

$$p_{x_k} = \Pr(X = x_k) \tag{5.25}$$

The digital images, of $M \times N$ pixels, can be interpreted as an array of random values of the variable X. By denoting the number of pixels having intensity k $(0 \leq k \leq 255)$

within the analysed image as g_k, we can estimate their occurrence probability (when $X = x_k = k$):

$$p_{\mathrm{k}} = \Pr(X = k) = g_k/T, \tag{5.26}$$

where $T = M{\cdot}N$ is the total number of pixels in the image. Therefore, the Shannon entropy H of the image S_n can be calculated as:

$$H(S_n) = -\sum_{k=0}^{255} p_k \log p_k = -\sum_{k=0}^{255} \frac{g_k}{T} \log \frac{g_k}{T} \tag{5.27}$$

In our case $M = N = 256$.

The SNR parameter has several definitions. If a signal a, having the standard deviation σ, is known to lie between two boundaries, $a_{\min} \le a \le a_{\max}$, then the SNR is defined as [128]:

$$SNR = 20\log\left(\left(a_{\max} - a_{\min}\right)/\sigma\right) \tag{5.28}$$

In our case $a_{\min} = 0$ and $a_{\max} = 255$. The standard deviation σ has to be assessed separately for each analysed image.

Both parameters, H and SNR, were estimated for each of the considered higher-harmonic images and their derivatives (Fig. 5.3, the images presenting intensities of the derivatives were marked analogously by S_{nd} – adding the index “*d*”). Moreover, we have observed that a higher entropy H results in a lower SNR in the considered images. That result is in some way obvious because more details means more information, which increases the entropy and decreases the signal-to-noise ratio. Thus, the simplest method of selecting images with high values of both parameters, H and SNR, cannot be applied to obtain satisfactory results, at least for the analysed experimental results. The most valuable would be the case when a higher-harmonic frequency coincides with the eigenmode of the AFM cantilever and amplifies the corresponding frequency component [34]. Such an image would reveal details of the specimen surface at a high signal-to-noise ratio (a low intensity of additive noise). Then, one could select the images of highest quality by comparing the estimated H and

SNR with the set of available pictures, including their derivatives which emphasize edges of the observed objects.

As can be seen (e.g. Fig. 5.3a), the first harmonic image does not unveil all details which are visible in other considered images (Fig. 5.3c, Fig. 5.3e, Fig. 5.3g). On the other hand, the higher-harmonic images are more noisy (e.g. Fig. 5.3h, having *SNR* = 23.68), and therefore some details are blurred and hardly perceptible. Moreover, while the first harmonic image makes quite visible edges of large topographical substructures (e.g. column No. $j = 30$, Fig. 5.2), the 5th harmonic image enhances structures exhibiting lower differences from the image offset. Thus, the final image created by superposition of a few images should be certainly more informative by preserving various details. To perform that task we have to select which of the images are the most informative and does not exhibit too intense additive noise component.

The higher-harmonic images were generated by using a lock-in amplifier and averaging over the recorded number of samples. The random error of estimated pixel intensity decreases with an increase of the number of averaged samples. When we generated higher harmonics, the number y_n of averaged samples decreased. For averaging the n^{th} harmonic it is given by:

$$y_n = y_1/n \tag{5.29}$$

Thus, we can expect a drop of *SNR* between consecutive higher harmonics due to limited averaging and due to the frequency characteristic of the vibrating tip (Tab. 5.2). The change of *SNR* between the 1st and other selected harmonics (in our example: 2nd, 5th, 6th) leads to the conclusion that the drop of *SNR* for the 6th harmonic image (Fig. 5.2g) cannot be explained only by limited averaging. We can suppose that the frequency $6f_0$ is far from any resonant frequency of the applied tip, what results in a poor quality of the image for this frequency. So, the image S_6 is not suitable for further consideration. When taking into account the entropy we can note a significant increase of H for the 5th harmonic image. Therefore, it would be reasonable to use a combination of the 1st and the 5th harmonic images to get the final image, exposing the mentioned surface details.

Tab. 5.2 The comparison of the differences ΔSNR and ΔH in the SNR and H between their values estimated for the 1st harmonic image (Fig. 5.2) and the n^{th} ($n = 2, 5, 6$) harmonic image; the same differences ΔSNR_d, ΔH_d were estimated for the derivatives of the images

Difference	**Higher-harmonic image**		
	$\boldsymbol{n = 1}$	$\boldsymbol{n = 2}$	$\boldsymbol{n = 5}$
$\boldsymbol{\Delta SNR}$	3.388	6.662	14.710
$\boldsymbol{\Delta H}$	1.795	2.688	3.658
$\boldsymbol{\Delta SNR_d}$	1.210	4.551	12.180
$\boldsymbol{\Delta H_d}$	0.407	1.087	2.377

The algorithm merges selected images into the resultant one exposing more clearly details of the analysed surface. The algorithm can be explained by analysing two exemplary higher-harmonic images: the 1st (Fig. 5.3a) and the 5th (Fig. 5.3e). We estimate the mean $\mu_{\Delta n}$ for all pixels of each of the analysed higher-harmonic images separately (in our experimental study for the 1st and the 5th harmonics; $n = 1$ or $n = 5$). In the next step we reduce various contrasts (offsets) in the considered images by adding to the selected picture the difference between the estimated mean values (e.g. we add $\mu_{\Delta 5} - \mu_{\Delta 1}$ to the image of the 1st harmonic). In the second step, for each pixel $q_n(i, j)$ (Fig. 5.4) its neighbouring pixels (the surrounding region) are taken into account. The size of the region was arbitrarily selected as a 5 x 5 square of pixels around the analysed inner pixel $q_n(i, j)$, as in other graphic algorithms (e.g. video coding [129]). The pixels which are close to the edges ($i = 1, 2$ and $j = 1, 2$) are left equal to the pixels present in the image of the first harmonic.

We assume that the image for the 1st harmonic ($n = 1$, Fig. 5.3a) displays the main objects present on the examined surface, while the higher-harmonic images ($n > 1$) reveal more subtle information correlated with other factors (e.g. changes in stiffness caused by either different materials or various surface treatment, e.g. the temperature sensitization).

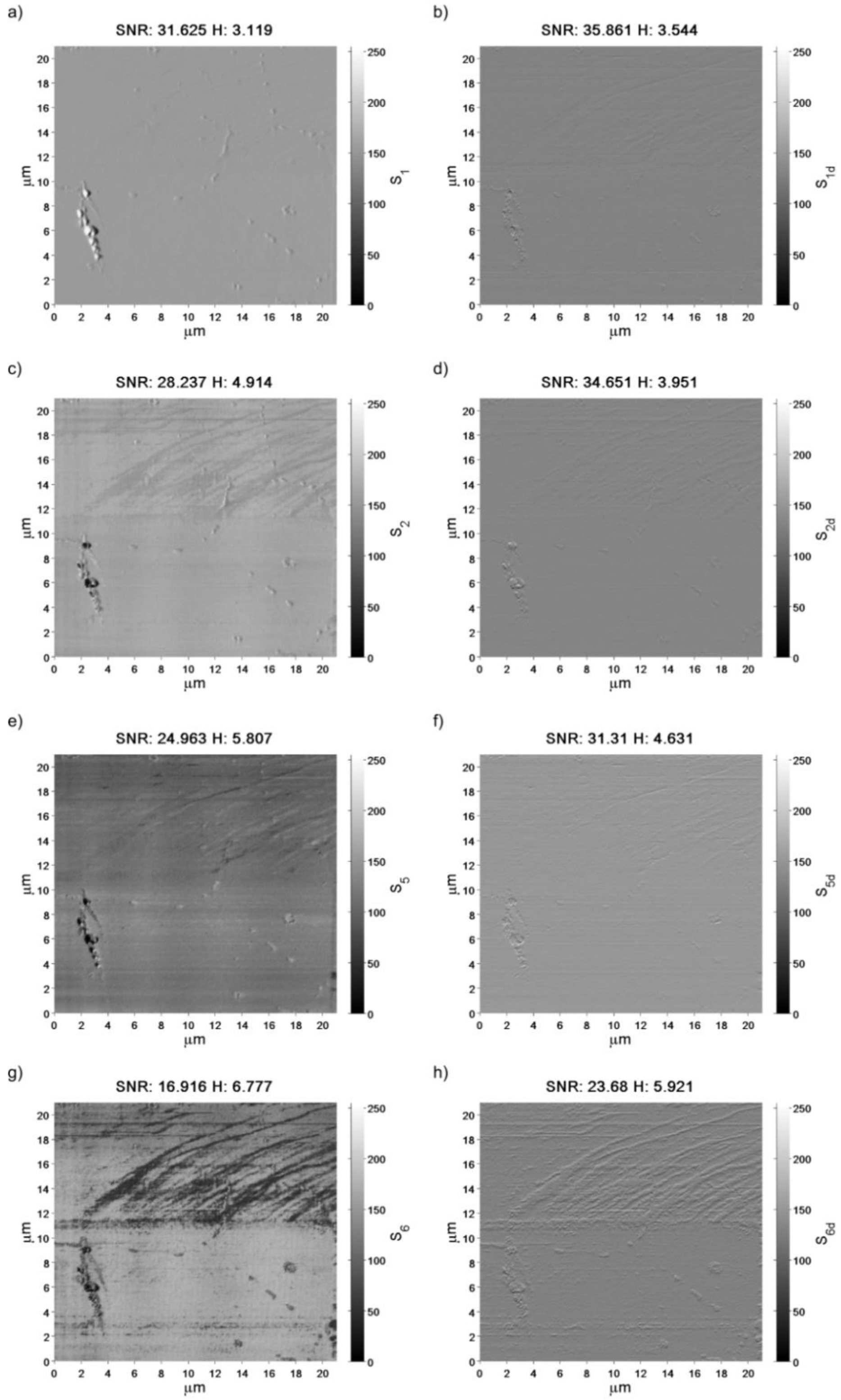

Fig. 5.3 The higher-harmonic images and their derivatives observed for the AISI304 stainless steel specimen with estimated *SNR* and entropy *H* values: a) the 1st harmonic S_1, b) the derivative of the 1st harmonic, c) the 2nd harmonic S_2, d) the derivative of the 2nd harmonic S_{2d}, e) the 5th harmonic S_5, f) the derivative of the 5th harmonic S_{5d}, g) the 6th harmonic S_6, h) the derivative of the 6th harmonic S_{6d}

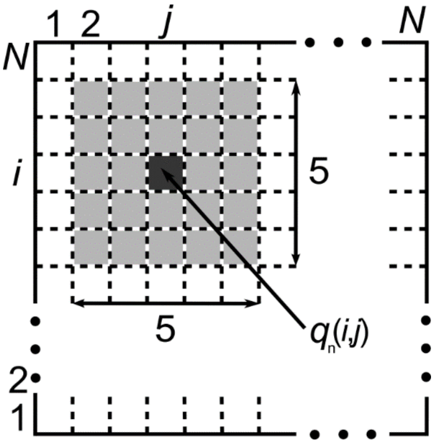

Fig. 5.4 A scheme of determining the region for each subsequent pixel $q_n(i, j)$ in the analysed image of the n^{th} harmonic

Thus, the objects which are well visible in the image for the first harmonic should be preserved in the merged image without any change. Only the details which are identified in the higher-harmonic images should be added to the final picture. Therefore, the resulting image has to include various parts of the considered pictures. That task can be done automatically by finding whether the mean value $\mu_{\Delta q1}(i, j)$ of the region around the considered pixel $q_n(i, j)$ is out of the assumed range around the estimated mean $\mu_{\Delta 1}$ of the 1st harmonic image. The procedure is resolved by the condition:

$$\left|\mu_{\Delta q1}(i,j)-\mu_{\Delta 1}\right| \le c_0\mu_{\Delta 1}\,, \tag{5.30}$$

where an arbitrarily chosen coefficient c_0 determines the width of acceptance range. If the condition (5.30) for $\mu_{\Delta q1}(i, j)$ is fulfilled, then the pixel $q(i, j)$ in the final image is taken from the higher-harmonic image (in our example - from the 5th harmonic image).

Fig. 5.5a presents the final image constructed by using the presented algorithm for the arbitrarily selected $c = 0.2$. Fig. 5.5b is the derivative of the constructed image (Fig. 5.5a). Fig. 5.5c shows the pixels selected from one of two considered candidates. The white points represent the 1st , whereas the black ones - the 5th harmonic images. The described procedure produced the image of a better entropy H and a slightly lower SNR than the constituent images. The algorithm requires only arbitrary selection of one parameter c. Its value can be easily evaluated after some trials for given experimental conditions.

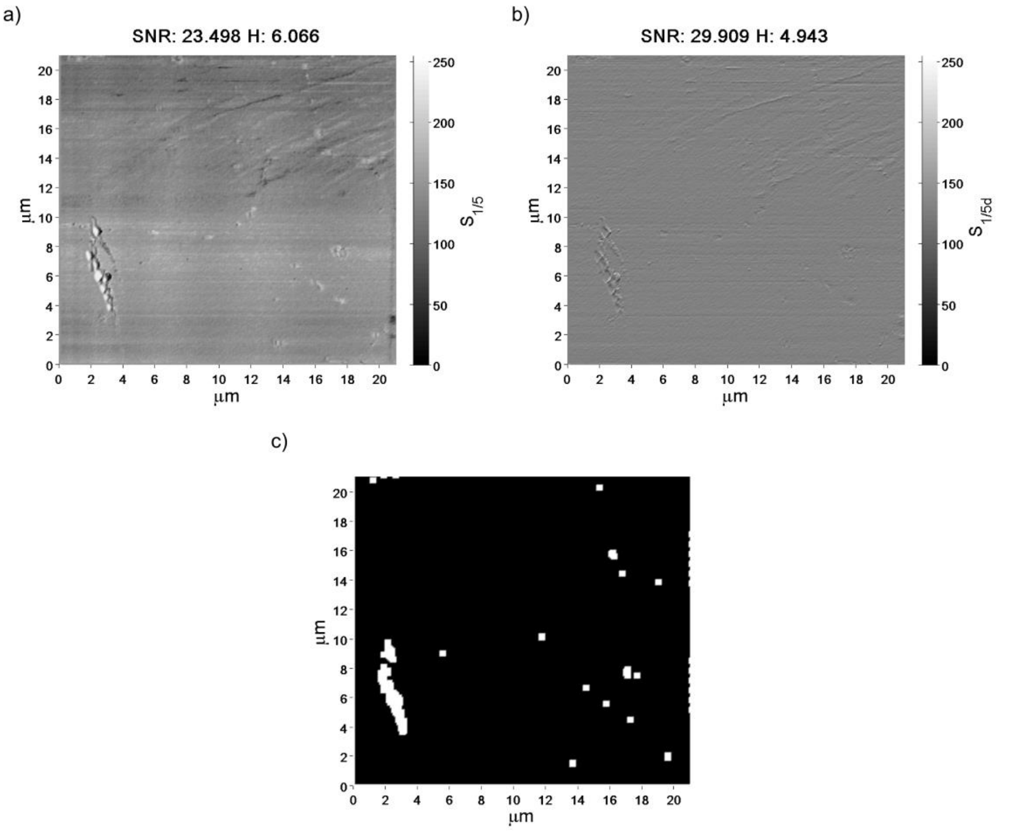

Fig. 5.5 The results of processing the 1st and the 5th harmonic images: a) the final image, b) its derivative, c) the illustration of pixels selected from the 1st (white) and the 5th (black) harmonic images to compose the final picture

Fast detection and diagnosis of topographic structures is essential in microscopic research of various surfaces. The AFM higher-harmonic imaging is an important source of additional information about the examined surface because it can determine the presence of various objects (e.g. corrosion products, variations in surface treatment) by exposing some differences in stiffness of the tested specimen. The AFM system can record lots of higher-harmonic images exposing such objects on the scanned surface. There is a need to propose efficient and automatic methods of reducing the volume of recorded data by composing the resulting image from the most informative parts coming from the obtained pictures. The quality of surface visualization and exposure of selected details may be improved by using the higher-harmonic images and the proposed procedure.

6 Conclusions

The main goal of the dissertation was to develop measurement tools enhancing capabilities of the AFM by recording and analysing the higher-harmonic images. The measurement setups and software were applied to analyse numerous experimental results. They confirmed their usefulness in different measurement conditions and for selected materials. The presented research results required continuous analysis of the AFM technique, the design of proposed measurement setups, and validity of numerous experimental studies.

The enumerated issues were presented in the following chapters. Firstly, some introductory information about the AFM technique was presented (Chapter 2). The mathematical model of the oscillating cantilever and its limitations were enclosed as well. Next, the main principles of the developed measurement setups were described (Chapter 3). It should be underlined that some results of the performed experimental studies – however important to validate the proposed setup – have been omitted in the thesis because of their irrelevancy (e.g. the results for mica or graphite). The measurement setup was designed to apply a relatively low-cost data acquisition board. This would help to popularize that solution among the scientists. Additionally, the setup includes a post-processing lock-in amplifier for more efficient higher-harmonic detection and additive noise component reduction. The prepared systems are an original achievements of the performed research.

The most interesting experimental results were presented for selected specimens having different physical properties, ZnO grains and AISI304 austenitic steel (Chapter 4). The experimental results suggest that higher harmonics can expose some differences in examined heterogeneous structures with significantly different physical properties of their components (e.g. Young’s modulus of glass fibre embedded in resin). Very similar effects were observed during monitoring steel corrosion processes. The differences between higher-harmonic images during corrosion product development were identified. This fact can be explained again by significantly different Young’s modulus of steel and oxides resulting from corrosion. Corrosion phenomena caused growth of oxides and development of local pits, resulting in heterogeneity of the examined surface (its locally different physical properties). These results confirmed, that corrosion processes can be monitored by higher-harmonics. That technique is innovative and original for corrosion monitoring. It can be claimed that the experimental studies proved the assertion: *higher-harmonic imaging can be used efficiently during corrosion process monitoring to reveal differences in various corrosion products (Chapter 4.3, assertion no. 1).* The last part of Chapter 4 presents some remarks about limitations and interferences present in the generated higher-harmonic images due to the averaging time, environmental conditions and material properties.

Selectivity of the higher-harmonic images to exposition of various surface elements means that all recorded higher-harmonic images should be analysed for various surface aspects. Such indispensability may be difficult and time-consuming. Moreover, two or more higher-harmonic images cannot be compared directly, due to different background colours and greyscales (Chapter 5). Therefore, a new original algorithm for combining the analysed pictures by selected statistical parameters was proposed (Chapter 5). The obtained results confirmed the second assertion: *exposure of the selected details may be improved by using the higher-harmonic images and the proposed procedure based on the parameters: signal-to-noise ratio and entropy (Chapter 5, assertion no. 2).*

It can be concluded that the prepared measurement systems and the developed software can be successfully used for various AFM units when the cantilever oscillates in either air or liquid. Thus, the system can monitor corrosion processes or some other heterogeneous structures, as confirmed by the original experimental results. Based on the detailed thesis findings, the following conclusions can be drawn:

1. the higher-harmonic imaging using a post-processing lock-in amplifier can be performed by the developed setups and can be easily implemented in popular AFM units,
2. the proposed software reduces the impact of noise in higher-harmonic images by applying algorithms reducing additive noise or attenuating harmonic interferences,
3. the higher-harmonic imaging can be effectively used when the cantilever is submerged in liquid (e.g. during corrosion process monitoring),

4. the proposed algorithm can automatically expose information present in different higher-harmonic images by combining relevant parts of various pictures into the unified one.

The dissertation, except of confirming the given assertions and developing the proposed measurement setups, inspired publishing a series of papers on the higher-harmonic imaging:

- two papers in journals indexed in the JCR library database,
- one manuscript submitted to the journal indexed in the JCR library database,
- four papers published in journals indexed by the Ministry of Science and Higher Education in Poland,
- three papers published in conference proceedings,
- lectures presented during six scientific conferences (including three international conferences).

Moreover, another manuscript based on the measurement results from Chapter 4.3 (corrosion processes monitoring) should be prepared soon.

Appendix A. **Graphical user interfaces**

During post-processing of the recorded data a special folder hierarchy (Fig. A.1) was applied to cope with a great number of saved signals. The folder hierarchy was used during selection of files to speed up that process. That method is time-saving and easier to implement than storing all files in one folder. Moreover, it gives an opportunity to postpone the processing stage after collecting the data and to resume it later. The graphic user interfaces developed for analysis of signals recorded during the AFM scanning contribute to making the higher-harmonic imaging faster and easier.

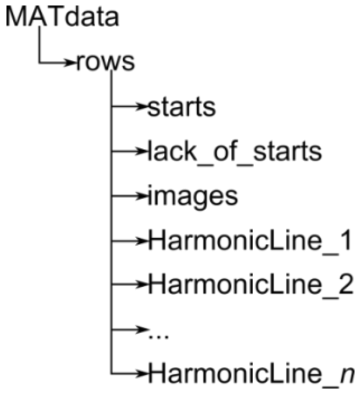

Fig. A.1 A scheme of the applied folder hierarchy

In Fig. A.2 all the steps of the prepared algorithm and software options are marked and described. Analogously, in Fig. A.3 all options of the prepared analysis software (Fig. 3.9) are marked. A row (the blue line) and a column (the red line) of the image may be chosen either by the blue (for rows) and red (for columns) sliders (*Option D*) or directly by two input boxes – the blue one for a row and the red one for a column (*Option E*). It is possible to change the set of higher-harmonic images by *Options A* and *B.* Selection of *Option C* has the same functionality as *Steps J & K* in the graphical user interface of the main processing program (Fig. A.2). The final images may be saved in MAT and PNG formats (*Option G*). The graphical user interface enables opening the next filtering panel (*Option F*) (Fig. A.4).

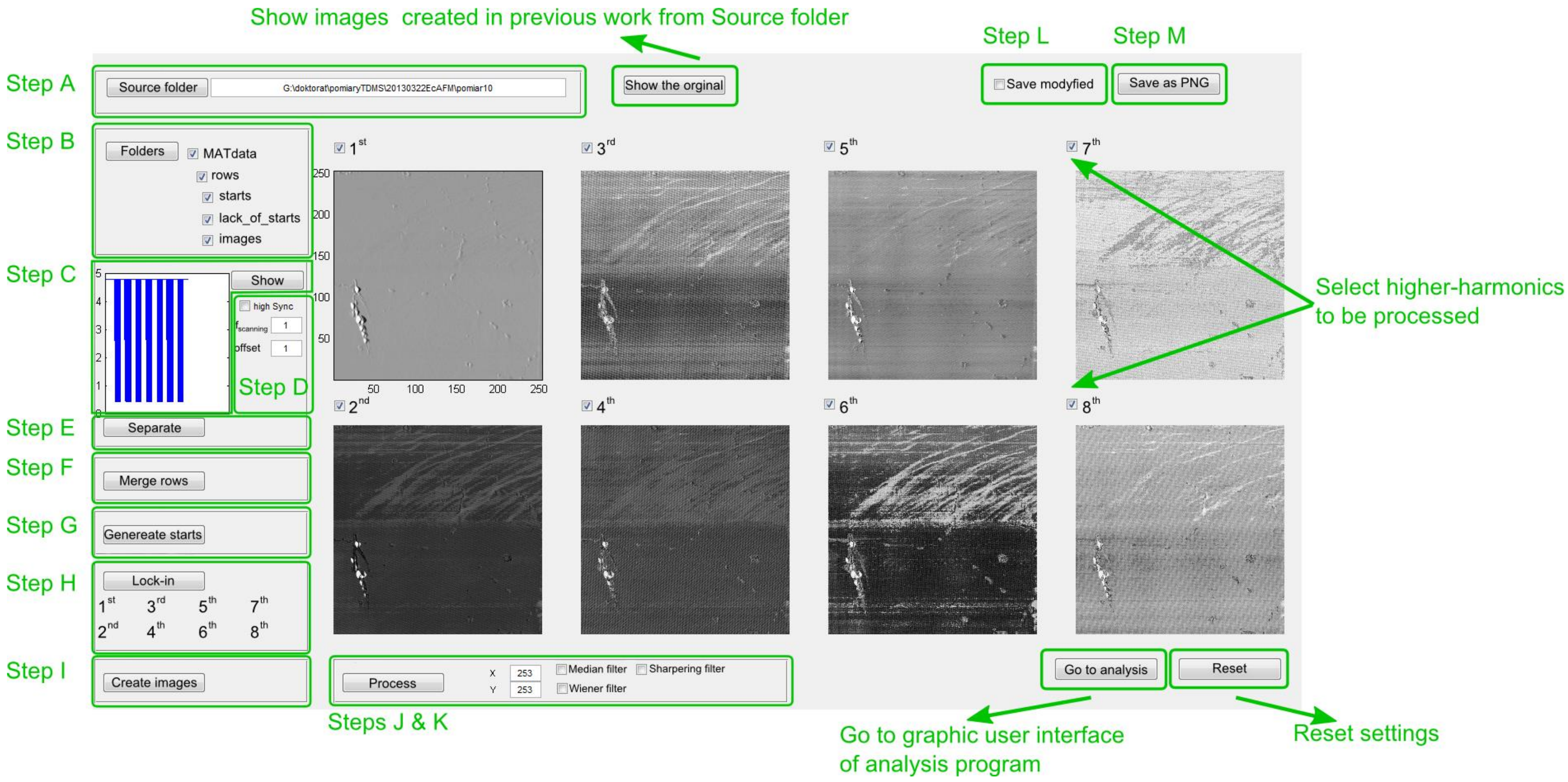

Source folder: G:\doktorat\pomiaryTDMS\20130322EcAFM\pomiar10

$f_{scanning}$: 1

offset: 1

X: 253

Y: 253

Fig. A.2 The graphical user interface of the prepared processing software (Fig. 3.5) with the marked algorithm steps

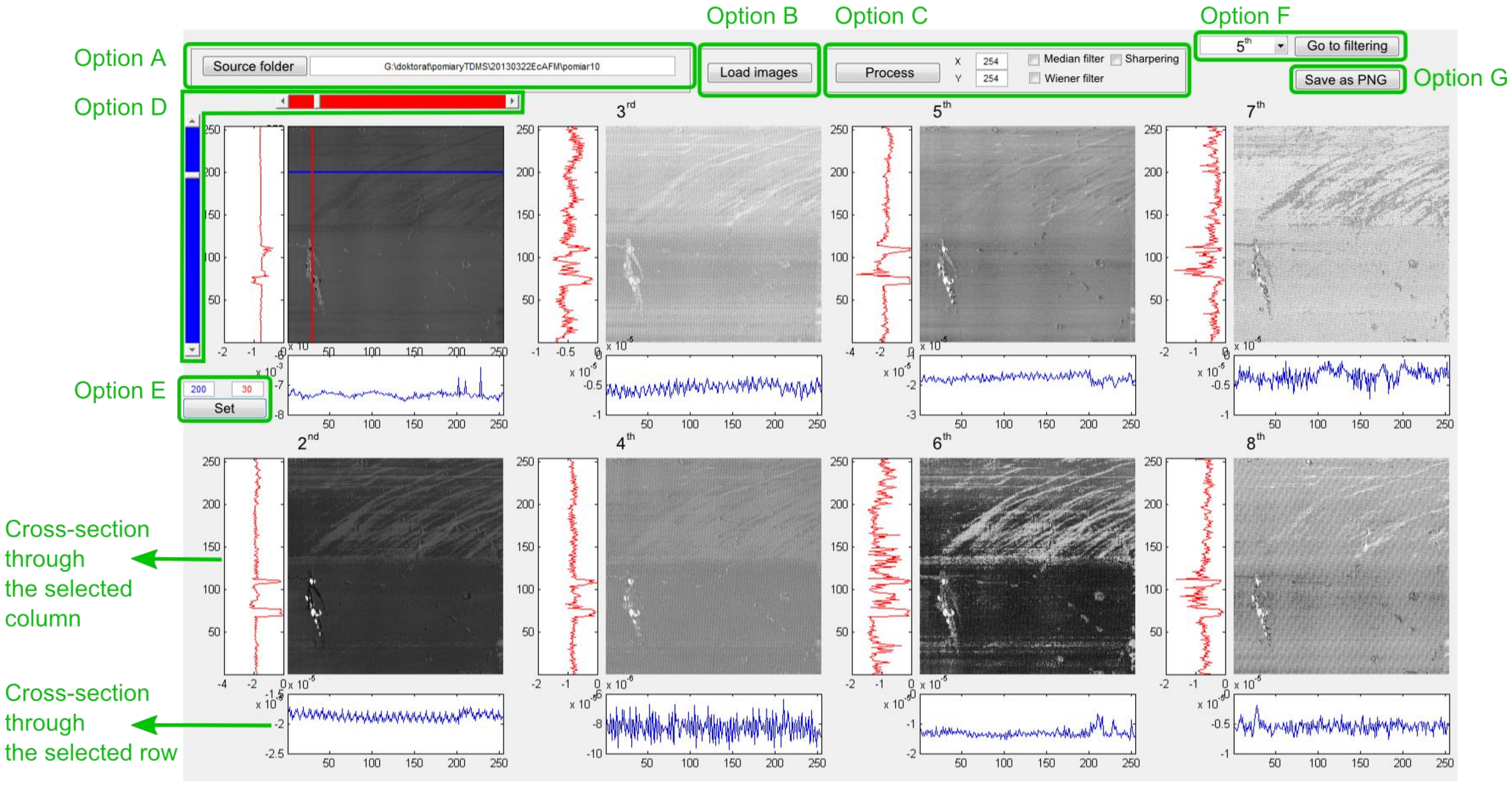

Fig. A.3 The graphical user interface of the prepared analysis software (Fig. 3.9) with the marked setting options

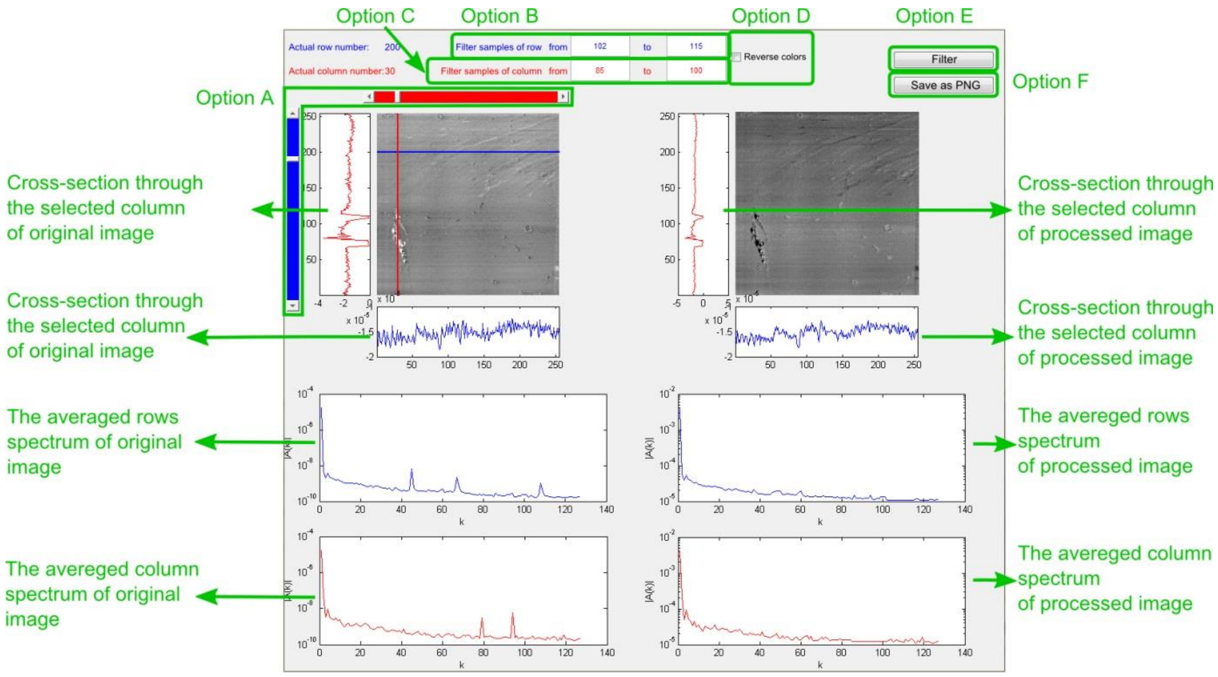

Actual row number: 200

Actual column number: 30

Filter samples of row from 102 to 115

Filter samples of column from 85 to 100

☐ Reverse colors

Fig. A.4 The graphical user interface of the filtration software (Fig. 3.10) with the marked setting options

Appendix B. The detailed experimental results of monitoring corrosion processes by higher-harmonic images

As a result of the electrochemical AFM measurements numerous higher-harmonic images were generated. A steel specimen was examined in different electrochemical conditions (various potential accelerating corrosion processes). The measurements were performed within a day after a few days of necessary preparations and trials of selecting the optimal cantilever type, the scanning frequency and electrolyte.

The specimen was scanned nineteen times in various conditions (measurement steps). Each scan generated eight higher-harmonic images (from the 1st to the 8th). Because of unpredictable development of corrosion processes some steps were redundant and were not subjected to further analysis. Other images were also excluded from further analysis because of their poor quality or insufficient informativeness when compared with other images. This appendix presents only the main results, limited to 42 images (Fig. B.1). Some of these images are repeated in Chapter 4 where the most interesting experimental results are discussed.

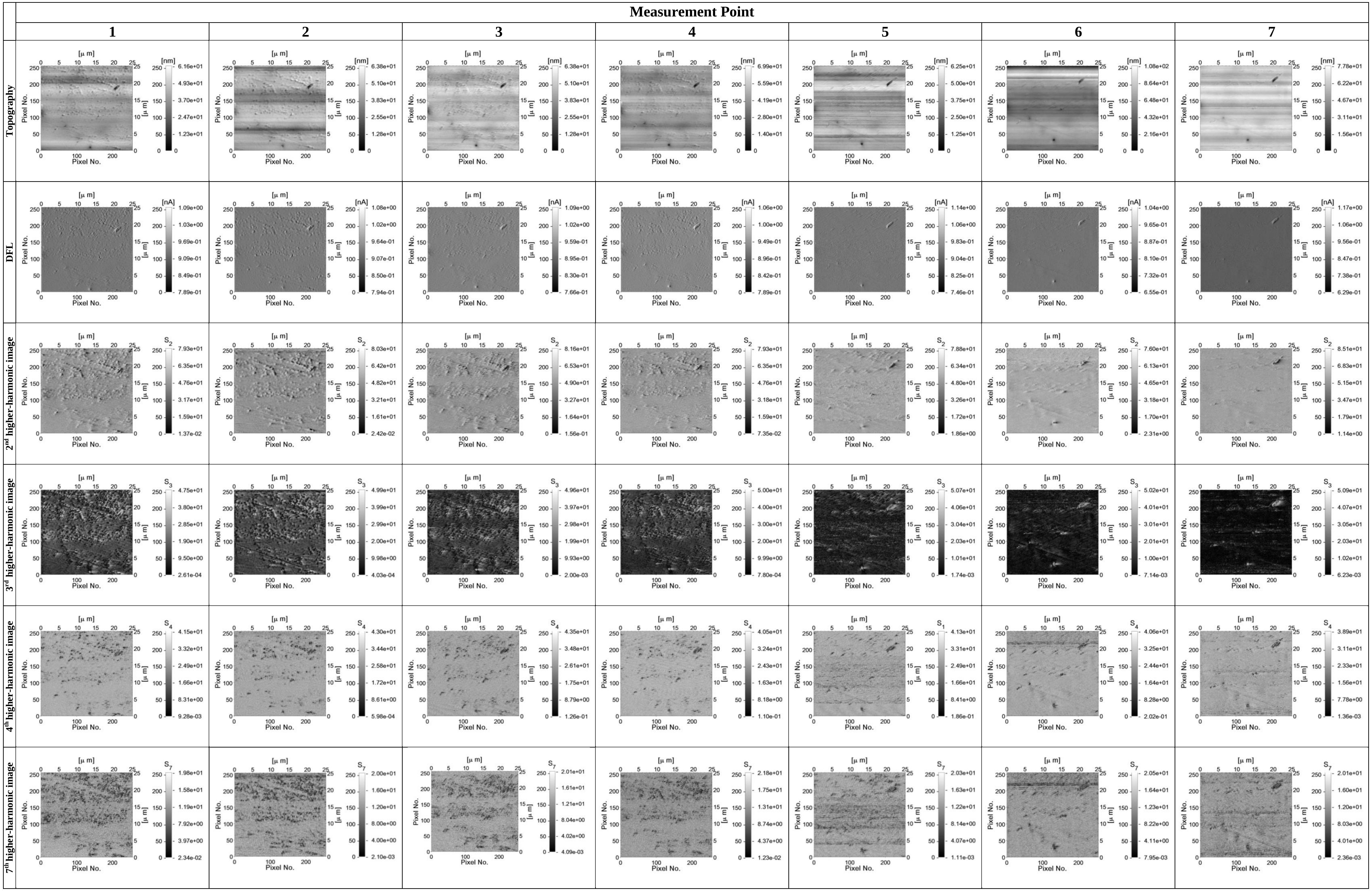

Fig. B.1 The measurement results of corrosion process monitoring

Appendix C. **Processing images using the Flatten Correction method**

An irregular background of an examined specimen influences intensity of the scattered light that enters the optical system during the exposure. Such an effect is caused by some unavoidable imperfections introduced by each optical element within a light path. To improve quality of the picture with non-uniform illumination, a necessary correction should be applied. The goal is to remove from the images artefacts caused by variations in the pixel-to-pixel sensitivity of the detector and/or by distortions in the optical path (Fig. C.1, Fig. C.2).

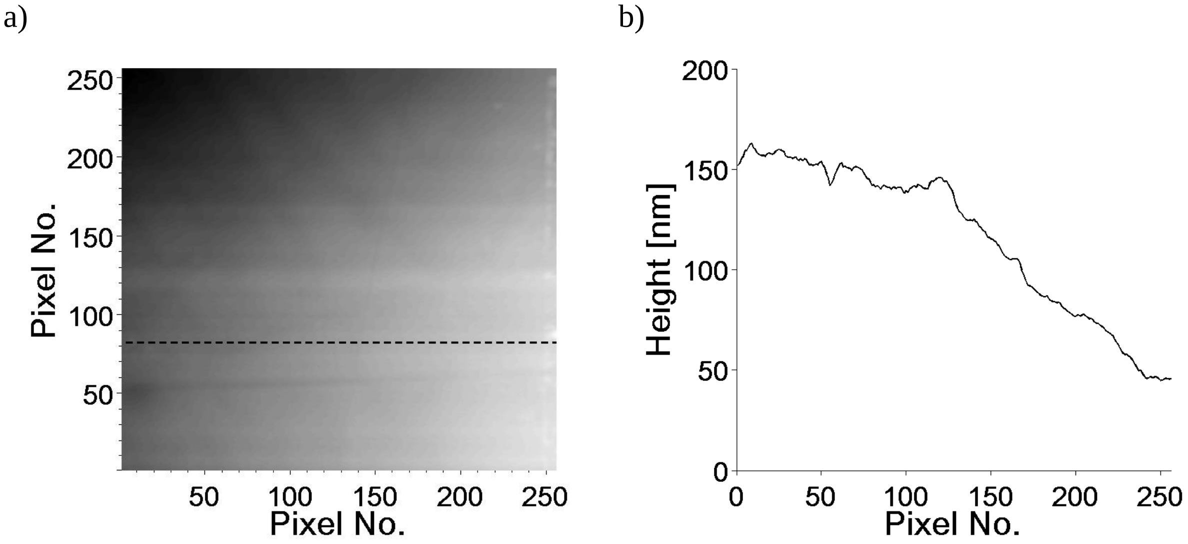

Fig. C.1 An exemplary image with irregular background of exemplary surface: a) an image with the marked 81st row (dashed line), b) a profile of the 81st row

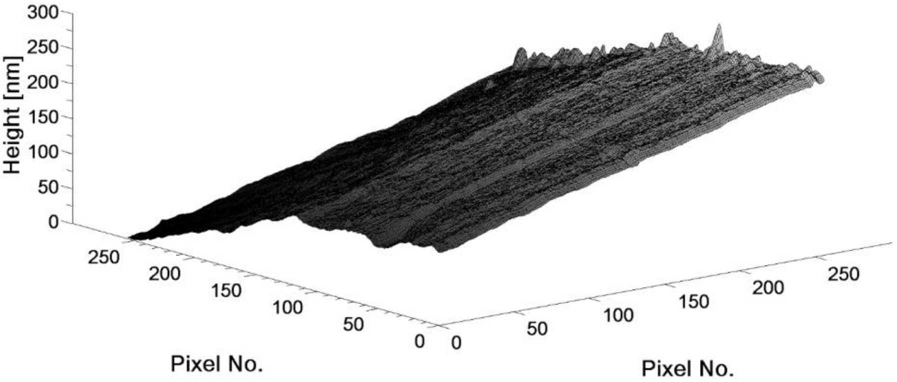

Fig. C.2 The three-dimension picture of the example surface presented in Fig. C.1

Slowly variating background level may by approximated by a polynomial and next subtracted from the original image. The 2nd or the 3rd order polynomials are commonly used for non-uniform illumination modelling. Polynomials of higher order could lead to some adverse effects and therefore they are not applied. The result of such approximation using the 2nd order polynomial and further its subtraction are presented in Fig. C.3. We observe much better quality and visualization of the surface details (Fig. C.3b, Fig. C.4). Such a correction may be performed by the AFM dedicated software NOVA automatically.

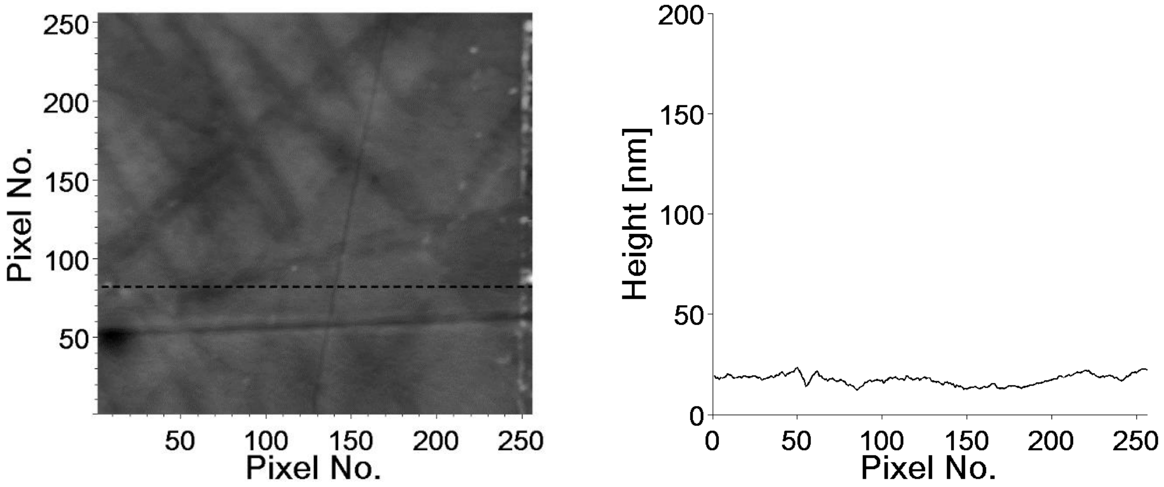
a) b)

Fig. C.3 The image with irregular background of an exemplary surface (Fig. C.1a) after the flatten correction: a) the image with the marked 81st row (dashed line), b) the modified profile of the 81st row

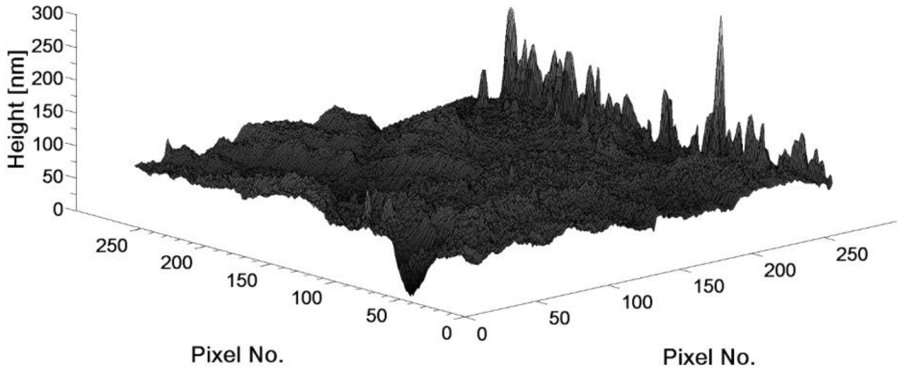

Fig. C.4 The three-dimension picture of an exemplary surface (Fig. C.1a) after the flatten correction

References

1. G. Binning and H. Rohrer, “Scanning tunneling microscopy”, Surface Science 126, 236-244 (1983).
2. G. Binnig, H. Rohrer, C. Gerber and E. Weibel, ‘‘Surface studies by scanning tunneling microscopy’’, Physical Review Letter 49, 57-61 (1982).
3. U. Dürig, J. K. Gimzewski and D. W. Pohl, “Experimental Observation of Forces Acting during Scanning Tunneling Microscopy”, Physical Review Letters 57 (19), 2403-2406 (1986).
4. G. Binnig and C. F. Quate, “Atomic Force Microscope”, Physical Review Letters 49 (1), 57-61 (1996).
5. G. Binning and H. Rohrer, “In touch with atoms”, Reviews of Modern Physics 71 (2), (1999).
6. Ch. R. Blanchard, “Atomic Force Microscopy”, Chemical Educator 1 (5), S324-S330 (1996).
7. S. Cuenot, Ch. Frétigny, S. Demoustier-Champagne and B. Nysten, “Surface tension effect on the mechanical properties of nanomaterials measured by atomic force microscopy”, Physical Review B 69, 165410 (2004).
8. R. Lüthi, E. Meyer, M. Bammerlin, A. Baratoff, T. Lehmann, L. Howald, C. Gerber and H.J. Güntherodt, “Atomic resolution in dynamic force microscopy across steps on Si(111)7×7”, Zeitschrift für Physik B 100, 165-167 (1996).
9. H. Ueyama, M. Ohta, Y. Sugawara and S. Morita, “Atomically Resolved InP(110) Surface Observed with Noncontact Ultrahigh Vacuum Atomic Force Microscope”, Japan Applied Physics 61, L1086-L1088 (1995).
10. F. J. Giessibl, “Atomic Resolution of the Silicon (111)-(7×7) Surface by Atomic Force Microscopy”, Science 67 (5194), 68-71 (1995).
11. Y. Sugimoto, P. Pou, M. Abe, P. Jelinek, R. Perez, S. Morita and O. Custance, “Chemical identification of individual surface atoms by atomic force microscopy”, Nature 446, 64-67 (2007).

12. R. W. Stark and W. M. Heckl, "Fourier transformed atomic force microscopy: tapping mode atomic force microscopy beyond the Hookian approximation", Surface Science 457 (1-2), 219-228 (2000).
13. R. W. Stark and M. Stark, "Higher Harmonics in Dynamic Atomic Force Microscopy", Applied Scanning Probe Methods II, NanoScience and Technology, 1-36 (2006).
14. L. Nony, R. Boisgard and J. P. Aime, "Nonlinear dynamical properties of an oscillating tip–cantilever system in the tapping mode", Journal of Chemical Physics 111 (4), 1615-1627 (1999).
15. M. Balantekin and A. Atalar, "Enhanced higher-harmonic imaging in tapping-mode atomic force microscopy", Applied Physics Letters 87 (24), 243513 (2005).
16. S. Akamine, R. C. Barrett and C. F. Quate, "Improved atomic force microscope images using microcantilevers with sharp tips", Applied Physics Letters 57 (3), 316-318 (1990).
17. G. Meyer and N. M. Amer, "Novel optical approach to atomic force microscopy", Applied Physics Letters 53, 1045-1047 (1988).
18. C. A. J. Putman, B.G. De Grooth, N. F. Van Hulst and J. Greve, "A detailed analysis of the optical beam deflection technique for use in atomic force microscopy", Journal of Applied Physics 72 (1), 6-12 (1992).
19. M. Enachescu, R. J. A. van den Oetelaar, R. W. Carpick, D. F. Ogletree, C. F. J. Flipse, and M. Salmeron, "Atomic Force Microscopy Study of an Ideally Hard Contact: The Diamond(111)/Tungsten Carbide Interface", Physical Review Letters 81 (9), 1877-1880 (1998).
20. P. Eaton and P. West, "Atomic Force Microscopy", Oxford University Press (2011).
21. B. Gotsmann, C. Seidel, B. Anczykowski and H. Fuchs, "Conservative and dissipative tip-sample interaction forces probed with dynamic AFM", Physical Review B 60 (15), 11051-11061 (1999).
22. D. Sarid, "Exploring Scanning Probe Microscopy with MATHEMATICA", (2007).
23. G. Schitter, P. Menold, H. F. Knapp, F. Allgöwer and A. Stemmer, "High performance feedback for fast scanning atomic force microscopes", Review of Scientific Instruments 72 (8), 3320-3327 (2001).
24. J. P. Hansen and L. Verlet, "Phase Transitions of the Lennard-Jones System", Physical Review 184 (1), 151-161 (1969).
25. H. Hölscher, U.D. Schwarz and R. Wiesendanger, "Calculation of the frequency shift in dynamic force microscopy", Applied Surface Science 140, 344-351 (1999).

26. **S. Babicz** and A. Zieliński, „Simulation and measurements for the substance identification by AFM”, Zeszyty Naukowe Wydziału Elektrotechniki i Automatyki Politechniki Gdańskiej 30, 17-20 (2011).
27. S. A. C. Gould, K. Burke and p. K. Hansma, “Simple theory for the atomic-force microscope with a comparison of theoretical and experimental images of graphite”, Physical Rewiev B 40 (8), 5363-5366 (1989).
28. F. J. Giessibl, “Advances in atomic force microscopy”, Reviews of modern Physics 75, 945-983 (2003).
29. A. Noy, Ch. H. Sanders, D. V. Vezenov, S. S. Wong and Ch. M. Lieber, “Chemically-Sensitive Imaging in Tapping Mode by Chemical Force Microscopy: Relationship between Phase Lag and Adhesion”, Langmuir 14, 1508-1511 (1998).
30. X. Chen, M. C. Davies,C.J. Roberts, S. J. B. Tendler, P.M. Williams, J. Davies, A. C. Dawkes and J.C. Edwards, “Interpretation of tapping mode atomic force microscopy data using amplitude-phase-distance measurements”, Ultramicroscopy 75, 171-181 (1998).
31. P. J. James, M. Antognozzi, J. Tamayo, T. J. McMaster, J. M. Newton and M. J. Miles, “Interpretation of Contrast in Tapping Mode AFM and Shear Force Microscopy. A Study of Nafion”, Langmuir 17, 349-360 (2001).
32. T. W. Kelley, E. L. Granstrom and C. Daniel Frisbie, “Conducting Probe Atomic Force Microscopy: A Characterization Tool for Molecular Electronics”, Advanced Materials 11 (3), 261-264 (1999).
33. E.J. Sullivan, D.B. Hunter and R.S. Bowman, “Topological and thermal properties of surfactant-modified clinoptilolite studied by tapping-mode atomic force microscopy and high-resolution thermogravimetric analysis”, Clays and Clay Minerals 45 (1), 42-53 (1997).
34. R. Garcia and R. Perez, “Dynamic atomic force microscopy methods”, Surface Science Reports 47, 197-301 (2002).
35. T. Gotszalk, P.B. Grabiec and I.W. Rangelow, “A novel piezoresistive microprobe for atomic and lateral force microscopy”, Sensors and Actuators A 123-124, 370-378 (2005).
36. R. Linnemann, T. Gotszalk, I. W. Rangelow, P. Dumania and E. Oesterschulze, “Atomic force microscopy and lateral force microscopy using piezoresistive cantilevers”, Journal of Vacuum Science & Technology B 14 (2), 856-860 (1996)

37. S. Morita, R. Wiesendanger and E. Meyer, "Noncontact Atomic Force Microscopy", Springer (2002).

38. R. Perez, Y. Stich, M. Payne and K. Terakura, "Surface-tip interactions in noncontact atomic-force microscopy on reactive surfaces: Si(111)", Physical Review B 58, 10835–10849 (1998).

39. N. Sasaki and M. Tsukada, "The relation between resonance curves and tip-surface interaction potential in noncontact atomic-force microscopy", Japan Journal of Applied Physics 37, L533-L535 (1998).

40. R. W. Stark and W. M. Heckl, "Higher harmonics imaging in tapping-mode atomic-force microscopy", Review of Scientific Instruments 74 (12), 5111-5114 (2003).

41. S. I. Lee, S. W. Howell, A. Raman and R Reifenberger, "Nonlinear dynamic perspectives on dynamic force microscopy", Ultramicroscopy 97 (1-4), 185–198 (2003).

42. S. I. Lee, S. W. Howell, A. Raman and R. Reifenberger, "Nonlinear dynamics of microcantilevers in tapping mode atomic force microscopy: A comparison between theory and experiment", Physical Review B 66 (11), 115409 (2002).

43. R. W. Stark, "Spectroscopy of higher harmonics in dynamic atomic force microscopy", Nanotechnology 15, 347-351 (2004).

44. J. E. Sader, "Frequency response of cantilever beams immersed in viscous fluids with applications to the atomic force microscope", Journal of Applied Physics 84, 64-76 (1998).

45. J. Tamayo and R. García, "Deformation, Contact Time, and Phase Contrast in Tapping Mode Scanning Force Microscopy", Langmuir 12 (18), 4430–4435 (1996).

46. R. Garcia and A. San Paulo, "Attractive and repulsive tip-sample interaction regimes in tapping-mode atomic force microscopy", Physical Review B 60 (7), 4961-4967 (1999).

47. O. Sahin and A. Atalar, "Simulation of higher harmonics generation in tapping-mode atomic force microscopy", Applied Physics Letters 79 (26), 4455-4457 (2001).

48. R. G. Winkler, J. P. Spatz, S. Sheiko, M. Möller, P. Reineker and O. Marti, "Imaging material properties by resonant tapping-force microscopy: A model investigation", Physical Review B 54 (12), 8908-8912 (1996).

49. B. Anczykowski, D. Krüger and H. Fuchs, "Cantilever dynamics in quasinoncontact force microscopy: Spectroscopic aspects", Physical Review B 53 (23), 15485 (1996).

50. B. Anczykowski, D. Krüger, K.L. Babcock and H. Fuchs, „Basic properties of dynamic force spectroscopy with the scanning force microscope in experiment and simulation", Ultramicroscopy 66 (3-4), 251-259 (1996).
51. J. R. Lozano and R. Garcia, "Theory of phase spectroscopy in bimodal atomic force microscopy", Physical Review B 79 (1), 014110 (2009).
52. J. Preiner, J. Tang, V. Pastushenko and P. Hinterdorfer, "Higher Harmonic Atomic Force Microscopy: Imaging of Biological Membranes in Liquid", Physical Review Letters 99, 046102 (2007).
53. B. Gotsmann and H. Fuchs, "Dynamic AFM using the FM technique with constant excitation amplitude", Applied Surface Science 188 (3-4), 355-362 (2002).
54. R. Garcia and A. San Paulo, "Dynamics of a vibrating tip near or in intermittent contact with a surface", Physical Review B 61 (20), 381-384 (2000).
55. A. F. Payam, D. Martin-Jimenez and R. Garcia, "Force reconstruction from tapping mode force microscopy experiments", Nanotechnology 26 (18), 1-12 (2015).
56. A. Sebastian, M. V. Salapaka, D. J. Chen and J. P. Cleveland, "Harmonic analysis based modeling of tapping-mode AFM", Proceedings of the American Control Conference San Diego, Califomia, 232-236 (1999).
57. F. J. Giessibl, "Forces and frequency shifts in atomic-resolution dynamic-force microscopy", Physical Review B 56 (24), 16010-16015 (1997).
58. J. B. Pethica and W. C. Oliver, "Tip Sample Interactions in STM and AFM", Physica Scripta T19, 61-66 (1987).
59. U. D. Schwarz, O. Zwörner, P. Köster and R. Wiesendanger, "Quantitative analysis of the frictional properties of solid materials at low loads. I. Carbon compounds", Physical Review B 56 (11), 6987-6996 (1997).
60. K. L. Johnson, "Contact mechanics", Cambridge University Press (1985).
61. B.V Derjaguin, V.M Muller and Yu.P Toporov, "Effect of contact deformations on the adhesion of particles", Journal of Colloid and Interface Science 53 (2), 314-326 (1975).
62. M. Kopycinska-Müller, R. H. Geiss and D. C. Hurley, "Contact mechanics and tip shape in AFM-based nanomechanical measurements", Ultramicroscopy 106, 466-474 (2006).
63. D. F. Ogletree, R. W. Carpick and M. Salmeron, "Calibration of frictional forces in atomic force microscopy", Review Scientific Instruments 67, 3298-3306 (1996).

64. O. Piétrement and M. Troyon, “General Equations Describing Elastic Indentation Depth and Normal Contact Stiffness versus Load”, Journal of Colloid and Interface Science 226 (1), 166-171 (2000).
65. S. C. Fain Jr., K. A. Barry, M. G. Bush, B. Pittenger and R. N. Louie, “Measuring average tip-sample forces in intermittent-contact (tapping) force microscopy in air”, Applied Physics Letters 76 (7), 930-932 (2000).
66. Ch. Lee and S. M. Salapka, “Model based control of dynamic atomic force microscope”, Review of Scientific Instruments 86 (4), 043703 (2015)
67. Sh. Hu and A. Raman, “Inverting amplitude and phase to reconstruct tip–sample interaction forces in tapping mode atomic force microscopy”, Nanotechnology 19 (37), 1-11 (2008).
68. R. Hillenbrand, M. Stark and R. Guckenberger, “Higher-harmonics generation in tapping-mode atomic-force microscopy: Insights into the tip-sample interaction”, Applied Physics Letters 76 (23), 3478-3480 (2000).
69. N. F. Martínez and R. García, “Measuring phase shifts and energy dissipation with amplitude modulation atomic force microscopy”, Nanotechnology 17 (7), S167–S172 (2006).
70. R. W. Stark, T. Drobek and W. M. Heckl, “Tapping-mode atomic force microscopy and phase-imaging in higher eigenmodes”, Applied Physics Letters 74 (22), 3296-3298 (1999).
71. T. Drobek, R. W. Stark, M. Gräber and W. M. Heckl, “Overtone atomic force microscopy studies of decagonal quasicrystal surfaces”, New Journal of Physics 1, 15.1-15.11 (1999).
72. R. Hillenbrand, M. Stark and R. Guckenberger, “Higher-harmonics generation in tapping-mode atomic-force microscopy: Insights into the tip-sample interaction”, Applied Physics Letters 76 (23), 3478-3480 (2000).
73. A. Kikukawa, S. Hosaka and R. Imura, “Vacuum compatible high-sensitive Kelvin probe force microscopy”, Review of Scientific Instruments 67 (4), 1463-1467 (1996).
74. Th. Glatzel, S. Sadewasser and M.Ch. Lux-Steiner, “Amplitude or frequency modulation-detection in Kelvin probe force microscopy”, Applied Surface Science 210 (1–2), 84-89 (2003).

75. N. F. Martinez, S. Patil, J. R. Lozano and R. Garcia, “Enhanced compositional sensitivity in atomic force microscopy by the excitation of the first two flexural modes”, Applied Physics Letters 89, 1531115 (2006).

76. T. R. Rodríguez and R. García, “Compositional mapping of surfaces in atomic force microscopy by excitation of the second normal mode of the microcantilever”, Applied Physics Letters 84 (3), 449-451 (2004).

77. J. R. Lozano and R. Garcia, “Theory of multifrequency atomc force microscopy”, Physical Review Letters 100 (7), 076102 (2008).

78. D. Platz, E. A. Tholen, C. Hutter, A. C. von Bieren and D. B. Haviland, “Phase imaging with intermodulation atomic force microscopy”, Ultramicroscopy 110, 573-577 (2010).

79. M. D. Aksoy and A. Atalar, “Force spectroscopy using bimodal frequency modulation atomic force microscopy”, Physical Review B 83 (7), 075416 (2011).

80. D. Martinez-Martin, E. T. Herruzo, C. Dietz, J. Gomez-Herrero and R. Garcia, “Noninvasive Protein Structural Flexibility Mapping by Bimodal Dynamic Force Microscopy”, Physical Review Letters 106 (19), 198101 (2011).

81. E. T. Herruzo and R. Garcia, “Theoretical study of the frequency shift in bimodal FM-AFM by fractional calculus”, Beilstein Journal of Nanotechnology 3, 198-206 (2012).

82. S. D. Solares and G. Chawla, “Triple-frequency intermittent contact atomic force microscopy characterization: Simultaneous topographical, phase, and frequency shift contrast in ambient air”, Journal of Applied Physics 108 (5), 054901 (2010).

83. R. Pedrak, Tzv. Ivanov, K. Ivanova, T. Gotszalk, N. Abedinov, I. W. Rangelow, K. Edinger, E. Tomerov, T. Schenkel, and P. Hudek, “Micromachined atomic force microscopy sensor with integrated piezoresistive sensor and thermal bimorph actuator for high-speed tapping-mode atomic force microscopy phase-imaging in higher eigenmodes”, Journal of Vacuum Science & Technology B 21, 3102-3107 (2003).

84. S. Jesse, S. V. Kalinin, R. Proksch, A. P. Baddorf and B. J. Rodriguez, “The band excitation method in scanning probe microscopy for rapid mapping of energy dissipation on the nanoscale”, Nanotechnology 8 (43), 1-8 (2007).

85. S. Jesse and S. V. Kalinin, “Band excitation in scanning probe microscopy: sines of change”, Journal of Physics D: Applied Physics 44 (46), 1-16 (2011).

86. J. Smulko, “Szumy czujników Metody pomiarów i analizy”, Wydawnictwo Politechniki Gdańskiej (2014).

87. R. W. Stark, , T. Drobek and W. M. Heckl, “Thermomechanical noise of a free v-shaped cantilever for atomic-force microscopy”, Ultramicroscopy 86 (1-2), 207–215 (2001).
88. H.–J. Butt and M. Jaschke, “Calculation of thermal noise in atomic force microscopy”, Nanotechnology 6 (1), 1-7 (1995).
89. **S. Babicz**, “Stochastic resonance in measurements”, 1st Students and PhD Students Conference and Electronics, Telecommunication, IT, automation and robotics ICT Young, May 28th -29th, Zeszyty Naukowe Wydziału Elektroniki, Telekomunikacji i Informatyki Politechniki Gdańskiej 9, 429-432 (2011).
90. A. Labuda, M. Lysy, W. Paul, Y. Miyahara, P. Grütter, R. Bennewitz and Mark Sutton, “Stochastic noise in atomic force microscopy”, Physical Review E 86 (3), 031104, (2012).
91. A. Raman , J. Melcher and R. Tung, “Cantilever dynamics in atomic force microscopy”, Nanotaday 3 (1-2), 20-27 (2008).
92. **S. Babicz**, A. Zieliński, J. Smulko and K. Darowicki, “Measurement system for nonlinear surface spectroscopy by atomic force microscopy for corrosion processes monitoring”, The 6th Congress of Metrology, Kielce-Sandomierz June 19th-22nd, 93-94 (2013),
93. **S. Babicz**, A. Zieliński and J. M. Smulko, “Enhancing capabilities of Atomic Force Microscopy by tip motion harmonics analysis”, Bulletin of the Polish Academy of Sciences Technical Sciences 61 (2), 535-539 (2013).
94. A. Sikora and Ł. Bednarz, “Direct measurement and control of peak tapping forces in atomic force microscopy for improved height measurements”, Measurement Science and Technology 22 (9), 094005 (2011).
95. A. Dulebo, J. Preiner, F. Kienberger, G, Kada, Ch. Rankl, L. Chtcheglova, C. Lamprecht, D. Kaftan, and Peter Hinterdorfer, “Second harmonic atomic force microscopy imaging of live and fixed mammalian cells”, Ultramicroscopy 109 (8), 1056-1060 (2009).
96. L. Yuan, Q. Jian-Qiang and L. Ying-Zi, “Theory of higher harmonics imaging in tapping-mode atomic force microscopy”, Chinese Physics B 19 (5), 050701 (2010).
97. A. Sikora and Ł. Bednarz, “Mapping of mechanical properties of the surface by utilization of torsional oscillation of the cantilever in atomic force microscopy”, Central European Journal of Physics 9 (2), 372-3-79 (2011).

98. A. Sikora and Ł. Bednarz, "The implementation and the performance analysis of the multi-channel software-based lock-in amplifier for the stiffness mapping with atomic force microscope (AFM)", Bulletin of the Polish Academy of Sciences: Technical Sciences 60 (1), 83-88 (2012).
99. M. L. Meade, "Lock-in amplifiers: Principles and application", IEE Electrical Measurement Series (1983).
100. M. Kotarski and J. Smulko, "Assessment of synchronic detection at low frequencies through DSP-based board and PC sound card", XIX IMEHO Word Congress Fundamental and Applied Metrology, 960-963 (2009).
101. J. H. Scofield, „Frequency-domain description of a lock-in amplifier", American Journal of Physics 66, 129-133 (1994).
102. **S. Babicz**, „Atomic Force Microscope data post-processing algorithm for higher harmonics imaging", Zeszyty Naukowe Wydziału Elektrotechniki i Automatyki Politechniki Gdańskiej 34, 9-12 (2013).
103. M. Kiwilszo, A. Zieliński, J. Smulko and K. Darowicki, Improving AFM Images with Harmonic Interference by Spectral Analysis, Microscopy and Microanalysis 18 (10), 186-195 (2012).
104. L. Z. Hasse, **S. Babicz**., L. Kaczmarek, J. M. Smulko and V. Sedlakova, "Quality assessment of ZnO-based varistors by 1/f noise", Microelectronics Reliability 54 (1), 192-199 (2014).
105. E. Olsson, G.L. Dunlop and R. Österlund, "Development of functional microstructure during sintering of Zn0 varistor materials", Journal of the American Ceramic Society 76 (1), 65-71 (1993).
106. E.S. Gadelmawla, M.M. Koura, T.M.A. Maksoud, , I.M. Elewa and H.H. Soliman, "Roughness parameters", Journal of Materials Processing Technology 123 (1), 133-145 (2002).
107. Ştefan Ţălu, "Nanoscale topography of 3-D engineering surfaces. Fractal and multifractal geometry in quantitative analysis at nanoscale". Habilitation Thesis, 2014.
108. L. Hasse and J. Smulko, "Quality assessment of high voltage varistors by third harmonic index", Metrology and Measurement Systems 15 (1), 23-31 (2008).
109. **S. Babicz**, "The study of harmonic imaging", Pomiary Automatyka Kontrola 57, 1508-1510 (2011).

110. J. Smulko, K. Darowicki, and A. Zieliński, „Evaluation of reinforcement corrosion rate in concrete structures by electrochemical noise measurements”, Russian Journal Electrochemistry 42 (5), 546-550 (2006).
111. J. Legleiter, M. Park, B. Cusick, B. and T. Kowalewski, „Scanning probe acceleration microscopy (SPAM) in fluids: Mapping mechanical properties of surfaces at the nanoscale”, Proceedings of the National Academy of Sciences of the United States of America 103 (13), 4813-4818 (2006).
112. G. H. Aydoğdu and M. K. Aydinol, „Determination of susceptibility to intergranular corrosion and electrochemical reactivation behaviour of AISI 316L type stainless steel”, Corrosion Science 48, 3565–3583 (2006).
113. H. Kokawa, M. Shimada, M. Michiuchi, Z. J. Wang, and Y. S. Sato, „Arrest of weld-decay in 304 austenitic stainless steel by twin-induced grain boundary engineering”, Acta Materialia 54 (16), 5401-5407 (2007).
114. M. A. Gaudett, and J. R. Scully, „Distributions of Cr Depletion Levels in Sensitized AISI 304 Stainless Steel and Its Implications Concerning Intergranular Corrosion Phenomena”, Journal of The Electrochemical Society 140 (12), 3425-3435 (1993).
115. W. K. Kelly, R. N. Iyer, and H. W. Pickering, „Another Grain Boundary Corrosion Process in Sensitized Stainless Steel”, Journal of The Electrochemical Society 140 (11), 3134-3140 (1993).
116. Ch.-M. Lai, „Reconstructing NMR images from projections under inhomogeneous magnetic field and non-linear field gradients”, Physics in Medicine and Biology 28 (8), 925-938 (1983).
117. H. Sahlaoui, K. Makhlouf, H. Sidhom and J. Philibert, „Effects of ageing conditions on the precipitates evolution, chromium depletion and intergranular corrosion susceptibility of AISI 316L: experimental and modeling results”, Materials Science and Engineering: A 372 (1-2), 98-108 (2004).
118. N. Lopez, M. Cid, and M. Puiggali, “Application of double loop electrochemical potentiodynamic reactivation test to austenitic and duplex stainless steels”, Materials Science and Engineering: A 229 (1-2), 123–128 (1997).
119. H. Kokawa, M. Shimada, and Y. Sato, “Grain-boundary structure and precipitation in sensitized austenitic stainless steel”, JOM 52 (7), 34–37 (2000).

120. A. Arutunow, K. Darowicki and M.T. Tobiszewski, “Electrical mapping of AISI 304 stainless steel subjected to intergranular corrosion performed by means of AFM–LIS in the contact mode”, Corrosion Science 71, 37-42 (2013).

121. J. Ryl, J. Wysocka, M. Jarzynka, A. Zielinski, J. Orlikowski and K. Darowicki, “Effect of native air-formed oxidation on the corrosion behavior of AA 7075 aluminum alloys”, Corrosion Science 87, 150-155 (2014).

122. **S. Babicz**, A. Zieliński and J. Smulko, “Problemy w obrazowaniu powierzchni za pomocą wyższych harmonicznych oscylacji igły mikroskopu AFM”, VII Seminar „Research conducted close interactions scanning microscopy methods - STM / AFM”, Zakopane November 28th –December 2nd, 8 (2012).

123. M. J. Weinberger, J. J. Rissanen and R. B. Arps, “Applications of universal context modeling to lossless compression of gray-scale images”, IEEE Transctions Image Process 5 (4), 575–586 (1996).

124. L. Seong-Lee, L. Dong-June and P. Hee-Seon, “A new methodology for gray-scale character segmentation and recognition”, IEEE Transctions Image Process 18 (10), 1045–1050 (1996).

125. C. Munteanu and A. Rosa, (2004). “Gray-scale image enhancement as an automatic process driven by evolution”, IEEE Transctions on Systems, man, and cybernetics – Part B 34 (2), 1292–1298 (2004).

126. M. R. Sabuncu, “Entropy-based image registration”, 2006.

127. Y. Wu, Y. Zhou, G. Saveriades, S. Agaian, J. P. Noonan and P. Natarajan, “Local Shannon entropy measure with statistical tests for image randomness”, Information Sciences 222, 323-342 (2013).

128. I. T. Young, J. J. Gerbrands and L. J. van Vliet, “Fundamentals of Image Processing”, Delft University of Technology (2007).

129. M. Wu, A. Vetro and Ch. W. Chen, “A Study of Encoding and Decoding Techniques for Syndrome-Based Video Coding”, Circuits and Systems, 2005. ISCAS 2005. IEEE International Symposium, 23 – 26 May 2005, Kobe, Japan, 4, 3527-3530.

List of figures

List of tables